Architecture of the neutrophil compartment in mice

Daniela Cerezo-Wallis[1,2]†, Andrea Rubio-Ponce[1,2]†, Mathis Richter[3], Emanuele Pitino[4], Immanuel Kwok[5], Juan Nieto[4], Giovanni Marteletto[1], Ana Cristina Guanolema-Coba[2], Ana Moraga[2,6], Natalia Borbaran Bravo[7], Samuel Dore[8], Sergio Callejas[2], David G. Aragonés[9], Daniel Jiménez-Carretero[2], Daniel Martin[2], Samuel Ovadia[1], Tommaso Vicanolo[2], Georgiana Crainiciuc[2], Jon Sicilia[2], Tong Deng[1], Anjelica Martin[1], Jing Zhang[10], Maria Isabel Cuartero[2,11], Diego Moncada Giraldo[12], Alicia Garcia-Culebras[2,6], Alejandra Aroca-Crevillen[2], Sandra Martín-Salamanca[2], Carlos Torroja[2], Sara Ruiz[4] , Melissa S. F. Ng[5], Ana Herruzo[13], David Chang van Oordt[14], Seokyoon Chang[14], Alexander E. Downie[14], Fei Chen[15], Andrea L. Graham[14], William C. Gause[15], Pierre-Olivier Fiset[16], Jonathan D. Spicer[17], Maria A. Zuriaga[2], Juan A Bernal[2], Irina Udalova[18], Maria A. Moro[2], Katrien de Bock[10], Ana Dopazo[2], Jose J. Fuster[2], Holger Heyn[4,19], Fátima Sánchez-Cabo[2], Gabriel F. Calvo[9], Julia Skokowa[7], Oliver Soehnlein[3], Daniela F. Quail[8], Logan A. Walsh[8], Lai Guan Ng[20], Andrés Hidalgo[1,2]¥ and Iván Ballesteros[2,21]¥

[1]Vascular Biology and Therapeutics Program and Department of Immunobiology, Yale University School of Medicine, New Haven, USA
[2]Centro Nacional de Investigaciones Cardiovasculares Carlos III, Madrid (Spain)
[3]Institute for Experimental Pathology (ExPat), Centre for Molecular Biology of Inflammation (ZMBE), University of Münster, Münster, Germany
[4] Centre Nacional d'Anàlisi Genòmica, Barcelona, Spain
[5] Singapore Immunology Network (SIgN), A*STAR (Agency for Science, Technology and Research); Singapore
[6] Departamento de Biología Celular e Histología, Facultad de Medicina, Universidad Complutense de Madrid (UCM), Spain
[7] University Hospital Tuebingen, Tuebingen, Germany
[8] Rosalind and Morris Goodman Cancer Institute, McGill University, Montreal, QC, Canada.
[9] Department of Mathematics & MOLAB-Mathematical Oncology Laboratory, Universidad de Castilla-La Mancha, Ciudad Real, Spain.
[10] Department of Health Sciences and Technology, Laboratory of Exercise and Health, ETH Zürich, Zurich, Switzerland
[11] Unidad de Investigación Neurovascular, Departamento de Farmacología y Toxicología, Facultad de Medicina, Universidad Complutense and Instituto de Investigación Hospital 12 de Octubre (i+12), Madrid, Spain
[12] Department of Pediatrics, Emory University School of Medicine, Atlanta, GA, USA
[13] Media and immersive experience center, The Design School, Arizona State University, Arizona State University, Temple, Arizona
[14] Ecology and Evolutionary Biology, Princeton University, Guyot Hall, Princeton, NJ 08544, USA.
[15] Department of Medicine, Center for Immunity and Inflammation, Rutgers, The State University of New Jersey, New Jersey Medical School, Newark, NJ 07101, USA.
[16] Department of Pathology, McGill University, Montreal, QC, Canada
[17] Department of Surgery, McGill University Health Center, Montreal, QC, Canada
[18] Kennedy Institute of Rheumatology, University of Oxford, Oxford, UK
[19] Universitat de Barcelona (UB), Barcelona, Spain
[20] Shanghai Immune Therapy Institute, Shanghai Jiao Tong University School of Medicine Affiliated Renji Hospital, Shanghai, China
[21]Department of Neuroscience and Biomedical Sciences, Universidad Carlos III de Madrid, Madrid, Spain

† These authors contributed equally as first authors
¥ These authors contributed equally as corresponding authors.

Abstract

Neutrophils exhibit remarkable phenotypic and functional diversity across tissues and diseases, yet the lack of understanding of how this immune compartment is globally organized creates confusion and challenges translation to the clinic. Here, we performed single-cell transcriptional profiling of neutrophils spanning 47 anatomical, physiological, and pathological scenarios to generate an integrated map of the global murine neutrophil compartment, which we refer to as *NeuMap*. The NeuMap integrates and expands existing models to generate fundamental new insights; it reveals that neutrophils organize in a finite number of functional hubs that distribute sequentially during maturation to then branch out into interferon-responsive, immunosuppressive and a functionally silent state that dominates the healthy circulation. Computational modeling and timestamp analyses identify prototypical trajectories connecting these hubs and evidence that the dynamics and preferred paths vary during health, inflammation, and cancer. We show that TGFβ, IFNβ, and GM-CSF push neutrophils along the different trajectories, and projection of chromatin accessibility sites onto the NeuMap reveals that the transcription factor JunB controls angiogenic and immunosuppressive states and promotes tissue revascularization. The architecture of the NeuMap appears to be conserved across sexes, environmental conditions and humans and, in the mouse, it allows inferring the pathophysiological state of the host by profiling blood neutrophils. Our study delineates the global architecture of the neutrophil compartment and establishes a framework for exploration and exploitation of neutrophil biology.

Introduction

The innate immune system is fundamental for anti-microbial defense and tissue homeostasis, and its dysfunction impacts virtually every pathology, from infection to cancer or ischemic disease. Among its cellular constituents, neutrophils stand out for their abundance, with billions produced every day in the human bone marrow (BM) through a well-defined series of differentiation steps before their release into the circulation as terminally differentiated, non-proliferative cells that eventually infiltrate most tissues (*1*, *2*). Work over the past decade has unveiled substantial heterogeneity of neutrophils and delineated a vast array of transcriptional and phenotypic states, of which only a few have been assigned functional roles (*3*). Paradoxically, the fundamental organization of the neutrophil compartment remains elusive, a limitation that creates confusion in their functional classification, physiological relevance, and clinical value.

Previous efforts to define the transcriptional organization of this compartment reported linear trajectories when profiling neutrophils from the BM, spleen, blood and inflamed tissues, and suggested active reprogramming of granulopoiesis by chronic diseases, such as cancer (*4*, *5*). It is unlikely, however, that these conditions encompass the full spectrum of transcriptional states of neutrophils given the vast variety of microenvironments, infectious agents, and malignant cells that inhabit or invade mammalian tissues, their transcriptional plasticity, and the wealth of functional states already identified across healthy and disease conditions (*3*). Hence, fundamental questions remain about 1) the actual number of possible transcriptional and functional states that neutrophils can acquire; 2) how these phenotypic states relate to each other; 3) the specific stage(s) that are reprogrammed by disease; and 4) the signaling and transcriptional programs that instruct the diversity of neutrophils in living tissues. We posited that understanding the global architecture of the neutrophil compartment might provide insights into these unknowns and facilitate the conversion of this phenomenal army of cells into therapeutic allies.

Here, we report the generation of a comprehensive transcriptional map of the neutrophil compartment in mice through single-cell profiling of neutrophils from multiple organs across multiple homeostatic and pathological conditions. The resulting NeuMap not only shapes the global structure of this compartment but, when combined with fate mapping, mouse genetics, *in vitro* treatment, disease models, and computational analyses, uncovers the dynamics of neutrophil maturation and peripheral reprogramming along predictable trajectories. Likewise, this comprehensive approach reveals cytokines and transcription factors that push neutrophils along these trajectories. We finally show that the high resolution of this map enables the generation of a diagnostic pipeline that infers the physiological status of the host.

Results

Transcriptional cartography of the neutrophil compartment

To generate a comprehensive transcriptional map of neutrophil diversity in C57BL/6J mice, we conducted single-cell RNA sequencing of Lineage^{NEG} (B220, CD3, CD19, NK1.1, Ter119) cells isolated from the BM, and CD11b^{+}Ly6G^{+} cells obtained from 13 tissues of C57BL/6J mice housed in specific pathogen free (SPF) conditions at different developmental stages, gender, age, and pathological perturbations ranging from sterile inflammation to infection and cancer models (Figure 1A, Extended Data Fig.1A and Table S1). For all our experiments, we used the BD Rhapsody platform (*6*) and included blood from healthy adult males as an internal reference to assess integration quality and control for batch effects across datasets. We performed two rounds of quality control to discard low-quality cells and used automated cell annotation (Immgen consortium) to ensure that only neutrophils were included in the map. To integrate all datasets from different experiments and laboratories, we employed the Seurat R package integration workflow, which captures common sources of variance across datasets and ensures clustering of biologically similar cells (see full details in Methods). We then applied dimensionality reduction techniques to visualize the transcriptional diversity of 129,829 neutrophils collected across 47 biological conditions (Figure 1A and Extended Data Fig.1B).

The resulting transcriptome embedding, which we refer to as NeuMap (Figure 1A-B), allowed visualization of the transcriptional space of the entire neutrophil compartment and revealed general properties by examining its topology. For example, an early granulopoietic program was easily identifiable as a linear structure originating in a region marked by genes associated with proliferation followed by genes involved in granule formation (Figure 1B and Extended Data Fig.1C-D). As expected, this granulopoietic structure was largely composed of neutrophils from the BM and spleen (Figure 1B and Extended Data Fig.1E) and featured maturation stages and synthesis of key granule components (Extended Data Fig.1B-C) (*7*, *8*). This differentiation program expanded and lost its linear topology as we incorporated neutrophils from healthy peripheral tissues (blood, lung, liver, and intestine) together with cells from a broad set of pathological conditions (different cancers, infections, and inflammation models; Extended Data Fig.1D). This resulted in expansion of the transcriptional space which ultimately converged into a defined end structure that featured programs associated with hypoxia and cancer (Figure 1C), without generating transcriptional areas separated from the main body of the map. The NeuMap also revealed a separate path connecting the initial and end states that was independent of the main granulopoietic path and was abundant in the lungs and inflamed tissues (Figure 1B). The integration of all neutrophils in a single, interconnected structure is consistent with the continued production and maturation of neutrophils (*9*) and suggested that most, if not all, transcriptional programs are accessible by neutrophils emanating from the granulopoietic program.

By observing the distribution of neutrophils from individual tissues of healthy, infected, inflamed or tumor-bearing mice, we found that the anatomical and physiological context dictated the distribution of the cells in different regions of the NeuMap (Figure 1B and Extended Data Fig.1E). Consequently, the global distribution of neutrophils in the NeuMap varied substantially depending on the pathophysiological status of the host, from healthy to acute or chronic inflammation, to cancer and to ischemic disease (Extended Data Fig.1F). In contrast, their distribution was similar (but not identical) when comparing healthy males, females and old individuals (Extended Data Fig.1G). These distributions were also consistent with those obtained by mapping neutrophils from existing datasets of healthy and tumor-bearing mice onto the NeuMap (Extended Data Fig.1H) (*7*, *10*, *11*). Interestingly, we found that healthy and pathological conditions shared the same granulopoietic pipeline and only diverged later, when neutrophils moved to extramedullary tissues (Figure 1D), suggesting that the transcriptional specialization of neutrophils mostly occurs after maturation in the BM. Finally, this “cartographic” inspection of the NeuMap revealed that neutrophils from healthy individuals are sufficiently diverse to build the general scaffold of the NeuMap, while those from inflammatory or tumoral conditions extend from these homeostatic states rather than creating entirely new programs (Extended Data Fig.1D).

We next searched for physiologically relevant regions within the NeuMap. We scored the NeuMap cells using a set of functional gene signatures and found that their expression patterns corresponded to distinct areas in the embedding (Figure 1C, Extended Data Fig.2A and Table S2). In addition to the proliferative and granule-synthesis regions described above, we found areas associated with metabolic state (OxPhos, hypoxia and glycolysis), chemotactic and antimicrobial functions, as well as antiviral responses, and signatures associated with cancer, which overlapped with areas of predicted immunosuppression and angiogenesis (Figure 1C and Extended Data Fig.2A).

To localize functional regions more precisely, we then combined unbiased clustering defined at different resolutions (Res 0.05-0.3; Extended Data Fig.2B-E) and performed optimal grouping of clusters and functional signatures. This allowed us to identify seven distinct transcriptional regions, or *hubs*, distributed within the NeuMap (Figure 1E and Extended Data Fig.2F), which we interpreted as predictive of the main functional states of neutrophils across most, if not all, physiological conditions of health, inflammation, infection, and cancer. These hubs included PreNeu-like neutrophils (*8*, *12*) defined by expression of *mKi67* and *Ltf*, that aligned with signatures of oxidative respiration, consistent with prior reports (*13*, *14*). A second hub (referred to here as the “Immature hub”) predicted active maturation and granule synthesis and was positive for *Mmp8* and *Cebpe*, a key regulator of granule protein synthesis (*8*, *15*). The third hub corresponded to *Cd52*+ neutrophils, which lacked a distinct transcriptional signature, had low mRNA content (Extended Data Fig.2A), and was typical of circulating neutrophils (“Immuno-silent” hub”). Neutrophils from a fourth hub displayed a conspicuous interferon response signature marked by expression of *Ifit1* and *Cd274* (which encodes for PDL1; “IFN-response hub”) and coincided with signatures of antiviral response (Figure 1C). This hub was similar to the G5b state reported in the blood and spleen of mice and humans during infection (*7*) (Extended Data Fig.1H). The next two hubs shared signatures associated with immunosuppression and angiogenesis, however, one featured expression of *Cd14* and *Ptgs2* and was typical of lung and liver neutrophils (*16*) (“Immunosuppression I hub”; IS-I), while the other expressed high levels of *Vegfa* and *Cd274* and was prominent in tumoral neutrophils (“Immunosuppression II hub”; IS-II). A final hub featured elevated expression of genes associated with MHCII (*H2* and *Cd74*). This hub, which is reminiscent of neutrophils reported to mediate antigen presentation (*17–19*), connected the PreNeu and IS-I hubs (Figure 1E), and was not further explored in this study. Neutrophils from different tissues or pathophysiological conditions had clear associations with the different functional hubs (Figure 1F). For example, while the PreNeu and immature hubs dominated in the BM, as expected, *Cd14*+ *Ptgs2*$^+$ IS-I neutrophils were abundant in the gut, liver, and lungs. In contrast, IFN-responsive neutrophils were abundant in infected, inflamed, and ischemic conditions irrespective of the tissue, and *Cd274*$^+$ and *Vegfa*$^+$ IS-II neutrophils were prominent in tumors, such as pancreatic adenocarcinoma (PDAC), and were largely absent from healthy tissues (Figure 1G and Extended Data Fig.2G-H). The transcriptional continuum between these hubs (gray in Figure 1E) includes neutrophils with intermediate or mixed profiles, distinct from the more defined states captured by the hubs.

We next examined whether the basic structure of the NeuMap in defined hubs was conserved across relevant biological variables including sex, housing conditions, mouse strains or in the presence of somatic mutations (Extended Data Fig.3A). We found remarkable conservation between males and females with only minor differences in hub distribution in the spleen and liver (Extended Data Fig.3B). Likewise, C57BL/6 mice maintained in germ-free or rewilded conditions showed only minor differences when compared with specific pathogen free (SPF)-housed mice, which mainly affected maturation in the bone marrow (Extended Data Fig.3C). Minor differences appeared also when mapping neutrophils from Balb/c mice across healthy tissues, or in conditions of infection and cancer (Extended Data

Fig.3D). Finally, we found that the structure of the map was not altered by a somatic mutation associated with clonal haematopoiesis (*Tet2*$^{-/-}$; (*20*)); Extended Data Fig.3E).

In summary, the NeuMap provides insights into the transcriptional structure of the neutrophil compartment across multiple tissues and physiological conditions at single-cell resolution, and allows the integration of profiles and signatures from existing datasets. Importantly, the integrated analysis reveals that neutrophils exist in a conserved finite number of transcriptional and functional states across anatomical sites, pathophysiological contexts, microbiome conditions, or genetic backgrounds.

Molecular, functional, and spatial profiling of the pulmonary compartment

We next explored the potential of this integrative map to uncover new biological properties of neutrophils. The NeuMap showed that the majority of neutrophils from the lungs, liver, and intestine at steady state localized within the *Cd14*+ *Ptgs2*+ IS-I hub and predicted immunosuppressive and angiogenic functions in these organs (Figure 1G, Extended Data Fig.1E and Figure 2A). To validate this prediction, we isolated neutrophils from the lung, as this organ hosts the largest pool of neutrophils among these organs (*2*), and compared their angiogenic and immunosuppressive properties with neutrophils from the blood, BM and spleen, to allow comparison with neutrophils localized in other transcriptional hubs (e.g., Immature, Immuno-silent and IFN-response hubs; Figure 1G).

Using an *in vivo* Matrigel plug model, we found that co-injection of lung neutrophils was substantially more potent at inducing neovascularization than neutrophils from the other tissues (Figure 2B). Likewise, co-incubation of lung neutrophils with activated CD8+ OT-I T cells had the most potent effect in suppressing their cytotoxic activity against OVA-expressing B16 melanoma target cells (Figure 2C), altogether confirming the predicted functional properties of neutrophils based on their distribution in the NeuMap.

To gain insights into possible transcriptional regulators of the IS-I hub, we performed single-cell assay for transposase-accessible chromatin (ATAC)-seq combined with RNA-sequencing (Dogma-seq; (*21*)) of neutrophils from the same four tissues at steady-state or during conditions of inflammation and cancer. A genome-wide search for transcription factor binding sites revealed that cells that mapped onto the IS-I hub were enriched for motifs bound by the AP-1 complex, SMAD and NFκB isoforms (Figure 2D and Extended Data Fig.4B), pointing to these transcription factors as potential regulators of their angiogenic and immunosuppressive properties of lung neutrophils. In contrast, neutrophils in the Immature and Immuno-silent hubs were enriched in motifs for members of the CEBP and KLF families, consistent with their known roles in neutrophil maturation (*12*, *22*). IRF- and STAT-related binding sites were largely restricted to the IFN-response hub, AP-1 and Bhlhe sites dominated in IS-II neutrophils, and the Antigen-presenting hub presented moderate enrichment for SMAD and AP-1 binding motifs. Finally, CEBP, NF-KB and SMAD binding sites were accessible in most hubs of the NeuMap (Extended Data Fig.4A-B), suggesting broad control of neutrophil transcription by these factors.

To begin validating these findings and explore the predicted role of AP-1 in regulating the properties of neutrophils in the IS-I hub, we generated mice with neutrophil-specific deletion of *Junb* (MRP8^{CRE}; JunB$^{fl/fl}$, referred to as JunBΔN mice), a core component of the AP-1 complex that was broadly expressed in mature neutrophils (Extended Data Fig.4C). Consistent with the predictions of the ATAC analyses, bulk transcriptome analysis of lung neutrophils from control versus JunBΔN mice revealed enrichment in genes associated with immunosuppression, angiogenesis and cancer, and this signature projected over the IS-I and IS-II hubs of the NeuMap (Extended Data Fig.4C). Further, scRNA-seq of neutrophils from JunB$^{\Delta N}$ mice revealed altered distribution of lung and liver neutrophils onto the NeuMap, but it did not affect neutrophils from the BM, blood, or spleen (Figure 2E and Extended Data Fig.4D). These alterations of lung neutrophils, however, were partial, suggesting that other transcriptional regulators contribute to shape the transcriptome of the IS-I hub. We confirmed that the alterations seen in these mice were cell intrinsic because transfer of BM neutrophils to the lungs of wild-type mice induced expression of genes involved in immunosuppression and angiogenesis only in control, but not JunB-deficient neutrophils (Extended Data Fig.4E). Importantly, although JunB$^{\Delta N}$ mice exhibited normal immature and mature neutrophil numbers in the BM (Extended Data Fig.4F), their capacity to suppress T cell activity *in vitro* and to promote Matrigel vascularization *in vivo* was lost (Extended Data Fig.4G-H). Consistent with these findings, lungs from JunB$^{\Delta N}$ mice showed reduced endothelial cell proliferation and numbers (Extended Data Fig.4I-J) in conditions previously shown to be controlled by neutrophils (young age and after irradiation (*16*)). To substantiate the pathological relevance of these observations in the context of cancer, we implanted subcutaneous LLC tumors in control and JunbΔN mice. Despite normal migration to the tumor site, we found reduced expression of typical cancer-associated markers in intratumoral neutrophils, including CD14, Sca1, and PDL1 (Extended Data Fig.4K-L). These phenotypic anomalies correlated with blunted endothelial cell proliferation and increased T cell infiltration in the tumors, and a strong reduction in tumor growth in these mice (Extended Data Fig.4M-O), indicating that neutrophils require active Junb signaling *in vivo* to acquire a pro-tumoral state (IS-II hub).

To assess whether JunB controlled the functional state of neutrophils irrespective of their anatomical localization in the lungs, we used a model of hind limb ischemia to examine neutrophil reprogramming during neovascularization. scRNA-seq of neutrophils extracted from ischemic limbs and mapped onto the NeuMap revealed that these cells distributed between the IS-I and IS-II hubs (Figure 2F), suggesting that they share the same transcriptional regulation and function as lung neutrophils. In line with this prediction, Doppler monitoring of restoration of blood flow in the ischemic limb revealed that reperfusion was significantly impaired in JunBΔN mice compared with littermate controls (Figure 2F), altogether demonstrating that AP-1 is a relevant regulator of neutrophil transcription and regenerative function across tissues. Thus, the NeuMap uncovers patterns of gene expression and enables the identification of transcriptional regulators of functional states (hubs), across anatomical locations and physiological contexts.

To further explore the notion that the NeuMap classifies neutrophils by functional state, rather than only by anatomical location, we profiled neutrophils from the same tissue subjected to different pathophysiological conditions. We again focused on the lungs and examined the profile of pulmonary neutrophils under conditions of health, flu infection (PR8 virus), and cancer (LLC adenocarcinoma). Whereas neutrophils from the naïve lungs localized mainly in the IS-I hub, as expected, those from infected lungs shifted toward the IFN-response and Ag presentation hubs, and those exposed to tumors moved towards the IS-II hub (Extended Data Fig.5A), indicating that both tissue and physiological context shape the phenotype and function of neutrophils.

To understand how the different transcriptional hubs relate to the microanatomical space of a tissue, we conducted spatial transcriptomics on lung sections from naive, flu-infected, and tumor-bearing mice. We first annotated the different anatomical domains based on histological appearance and cell lineage signatures for each spot (Extended Data Fig.5B-D) and confirmed that the overall tissue acquired a marked interferogenic signature in infected lungs, immunosuppressive and angiogenic in peritumoral areas, and proliferative inside the tumors (Extended Data Fig.5B).

We identified the spots that contained neutrophils in these tissues and assigned them a similarity score for the IFN-response and IS-I hubs (Figure 2G-H). We found that the Immunosuppression signature was particularly high in border tumor areas when compared with neutrophils from the tumor core, adjacent tissue, or naïve lungs (Figure 2G and Extended Data Fig.5C). In contrast, the IFN-response score was high in neutrophils around infected bronchioles but was almost undetectable in naïve lungs (Figure 2H and Extended Data Fig.5C). Conversely, when we projected the signature of the spatially-identified neutrophils onto the NeuMap, we found that the signature of neutrophils from tumors showed a broad distribution that included the IS-I and IS-II hubs (Figure 2G), whereas the signature of neutrophils from the flu-infected lungs overlapped with the IFN-response hub (Figure 2H). The association between the IS-II hub and neutrophils in border areas of tumors may explain the aggressive nature of the invasive tumor front (*23*), and we confirmed these spatial associations in a PDAC spatial dataset (from (*4*); Extended Data Fig.5E). Interestingly, IFN-response, IS-I, and IS-II neutrophil signatures could also be detected in the border zone of infarcted areas of the myocardium (dataset from (*24*); Extended Data Fig.5E), suggesting that different stresses can elicit similar responses in neutrophils. Our analyses further revealed that neutrophils from different hubs have distinct spatial associations with various types of T cells, macrophages, and fibroblasts (Extended Data Fig. 5F), providing insights into where these neutrophils are educated in the tissue and their potential impact on other immune and non-immune cells. Thus, despite the inherent limitations of spatial sequencing, our data suggest that the distribution of neutrophils in the NeuMap reflects microanatomical location and physiological states.

Finally, we examined the association of the different hubs in the NeuMap with protein expression and spatial distribution of neutrophils in the lungs subjected to the same perturbations of infection and cancer. We employed cyclic labelling tools to stain lung sections with a panel of 8 antibodies predicted to identify neutrophils from the different hubs present in the lungs (Extended Data Fig.5G-H) and performed unbiased clustering and UMAP embedding to identify eight patterns of neutrophils by protein content (clusters 1-8 in Figure 2I-M). We found that each phenotypic cluster identified neutrophils associated with different perturbations and regions of the tissue (Figure 2M and Extended Data Fig.5H-I). For example, cluster 1 lacked specific markers and was typical of naïve lungs and non-affected tissue adjacent to tumors (Figure 2J-K), whereas expression of MHCII and CD14 and elevated expression of CD11b (cluster 5) was characteristic of intratumoral neutrophils (Figure 2K and Extended Data Fig.5I), and PDL1+ and IFIT1+ neutrophils (clusters 6 and 7) were abundant in flu-infected sites (Figure 2L and Extended Data Fig.5I). Although markers of immature states (*Ly6g*, *Cxcr2*, *Ly6c1* and *Cd11b*) typically showed poor correlation with their position in the NeuMap, the good match with genes expressed extramedullary in the other hubs (*Cd274*, *Cd14*, *Ifit1* and *H2* genes; Extended Data Fig.5G-H) supported the notion that specialized neutrophils localize in specific anatomical environments *in vivo*. This partial mismatch between transcript and protein expression affecting maturation and granule-associated genes has been reported for neutrophils (*25*), and restricts the transcript-protein associations from our study mainly to extramedullary tissues.

Overall, these findings highlight the potential of NeuMap to integrate transcriptional, phenotypic, anatomical, and functional profiles of neutrophils across tissue microenvironments and physiological states.

Transcriptional trajectories within the NeuMap

Our initial analyses suggested that neutrophils transit through a series of transcriptional states and paths defined in the NeuMap that are specific of each tissue and physiological state of the host (Extended Data Fig.1F). To explore the dynamics of these transits in detail, we examined the distribution of neutrophils from several tissues (BM, blood, lung, spleen, and liver, plus the tumoral mass in tumor-bearing mice) across the different transcriptional hubs in conditions of health, cancer (PDAC), and acute inflammation induced by lipopolysaccharide (LPS) injection (Figure 3A-C). We found that the distribution of the neutrophils in the NeuMap varied for each treatment: neutrophils from healthy mice distributed through the Immature, Immuno-silent and IS-I hubs and had a detectable number of IFN-responsive neutrophils despite the absence of infection (Figure 3A). Tumor-bearing mice, in contrast, had very few neutrophils in the Immuno-silent and Interferon hubs, and instead shifted towards the IS-I and IS-II hubs (Figure 3B). Finally, most neutrophils from LPS-treated mice localized in the IFN-response hub and almost completely disappeared from the Immuno-silent and IS-I hubs (Figure 3C). Interestingly, the distribution of neutrophils in the NeuMap remained relatively constant for each tissue across all conditions (Extended Data Fig.6A), supporting the notion that both the tissue and the physiological state of the host influence the transcriptional dynamics of neutrophils.

We employed RNA Velocity analysis (26) to infer the transcriptional trajectories of neutrophils in the NeuMap, focusing on conditions (health, cancer, and inflammation) that could be individually validated using in vivo fate-mapping analyses (see below). The velocity analyses showed that, while the transition vectors from the PreNeu to the Immature hub were present in all groups, the downstream trajectories varied across the different conditions. Healthy mice favored the transition from the Immature to the Immuno-silent hub, tumor-bearing mice transitioned towards the IS-I hub, and inflamed mice manifested a shift to the IFN-response hub that was already noticeable at the immature state (Figure 3A-C). Interestingly, only tumor-bearing mice showed transcriptional transitions in the IS-II hub (Figure 3A-C), suggesting activation of this transcriptional area during cancer.

To experimentally determine the trajectories of neutrophils in the NeuMap, we performed genetic-tracing experiments using the recently reported iLy6G^{tdTomato} mice (*16*) in the same conditions of health, cancer, and inflammation. We isolated Tomato-labelled neutrophils from the BM 24h after tamoxifen treatment, and from the blood, spleen, and lung 36 and 72h following tamoxifen injection (Figure 3D). This experimental design allowed initial labelling of mature neutrophils in the marrow to assess potential alterations in granulopoiesis at early times and to capture their fate at later times in tissues where neutrophils are more abundant (blood, lung, and spleen; Extended Data Fig.6B; (*16*)). Mapping the single-cell transcriptomes of the Tomato+ cells in the NeuMap revealed that although neutrophils from the three conditions followed similar maturation paths in the BM, they followed separate trajectories in the other tissues (Figure 3D and Extended Data Fig.6D). Unexpectedly, we found that neutrophils from LPS-treated mice activated an additional route of maturation directed towards the IFN-driven hub (Maturation path II in Figure 3E and Extended Data Fig.6C). This trajectory was similar to the canonical maturation path I (shown in Figure 3E) but lacked activation of genes typically associated with homeostatic maturation, including *Cd101*, *Cxcr4*, *Sell* or *Csf3r*, while inflammatory genes such as *Icam1* or *Pdl1* were elevated (Extended Data Fig.6C), suggesting that this path reflects an accelerated and activated type of granulopoiesis. Consistent with this hypothesis, flow cytometric analyses revealed reduced frequency and intensity of CD101 expression and increased presence of PDL1+ ICAM1+ in bone marrow neutrophils after LPS treatment *in vitro* (Extended Data Fig.6E). Likewise, BrdU pulse-chase experiments confirmed accelerated transit of neutrophils across tissues, with LPS treatment resulting in faster transition of neutrophils from the BM to the bloodstream, and from the bloodstream to the spleen (Extended Data Fig.6F). This associated with the appearance of a small fraction of mature neutrophils only in the BM of LPS-treated mice that localized in the Immuno-silent and IFN-driven hubs (Figure 3D). Thus, the NeuMap facilitates visualization of maturation paths, including alternative routes of emergency granulopoiesis.

We then compared the trajectories of the Tomato+ neutrophils in peripheral tissues (blood, spleen, and lungs) of healthy, inflamed and tumor-bearing mice. We noticed that neutrophils from all conditions transited between the different transcriptional hubs defined in the NeuMap (Figure 1F) and began branching out into two separate trajectories by 36h (Figure 3D). However, the preferred pathways (seen as denser clouds in Figure 3D) differed between conditions; neutrophils in healthy and tumor-bearing mice favored the IFN-response hub at late time points (72h). Inflammation, in contrast, favored the accumulation of neutrophils at the Immune-silent hub by 72h. We confirmed this pattern in a model of zymosan-induced peritonitis (Extended Data Fig.6G), in which peritoneal neutrophils initially localized in the immature to Interferon-response hubs (24h) but transitioned to the Immuno-silent hub by 72h, suggesting that this trajectory is specifically favored during inflammation. We also noticed that only neutrophils from tumor-bearing mice transited from the IS-I hub to the IS-II hub (Figure 3D and Extended Data Fig.6D), a finding that aligned with the presence of neutrophils from various cancer models in this transcriptional state (Extended Data Fig.1F and Extended Data Fig.2A). Finally, we noticed that the Immunosuppression hub typical of lung neutrophils appeared rapidly (at 36h) but was largely gone by 72h, suggesting fast and distinct kinetics for this transcriptional program in the lungs.

By combining all the trajectories from the three conditions, we were able to model a network of transcriptional transitions and hubs in the NeuMap, and used pseudotime analysis to identify genes that were specifically activated in those transitions (Figure 3E and Extended Data Fig.6H). We found, for example, that the canonical maturation program (path I) involved the simultaneous activation of inflammatory, anti-inflammatory, and interferon-regulated genes (e.g., *Dusp1*, *Nlrp3*, *Ifitm1*; Figure 3E). This profile that was consistent with this path splitting into at least two trajectories, one leading to the Immune-stasis and the other to the IFN-response hub, suggesting that at this early stage neutrophils activate broad genetic programs without committing to only one. We also found that two independent trajectories led to the IFN-response hub, the first originated from a mature intermediary state (IFN-response path) and the second from the immature hub (Maturation path II) and that both induced many IFN-regulated genes (*Ifit1*, *Oasl1*, *Isg15*) including *Ly6e*, which encodes for a recently reported marker of anti-tumoral neutrophils (*26*). A different trajectory connected the IFN-response and IS-I hubs and involved well-known immunoregulatory genes (*Trem1*, *Ptgs2*, *Cd14*) and transcription factors (*Nr4a1* and *Fosb*). Finally, a path connecting the IS-I and IS-II hubs, showed activation of genes involved in angiogenesis, inflammation, and immunoregulation (*Vegfa*, *Icam1*, *Cd274*). Representation of the preferred trajectories of neutrophils in healthy, tumor-bearing and inflamed mice onto the NeuMap suggested that, although the global structure of this network of trajectories is conserved, each condition has preferred transcriptional paths that are followed by neutrophils (Figure 3F).

Thus, the mapping of temporal series onto the NeuMap infers transcriptional dynamics of neutrophils as they mature in the BM and transition into peripheral tissues to acquire new properties. We speculate that the selective activation of different paths to connect the various transcriptional hubs confers the neutrophil compartment an additional layer of plasticity.

Deterministic signaling drives the different maturation and functional profiles

The transcriptional directionality seen in the NeuMap suggested that active signaling propelled neutrophils from their immature forms into the different specialized hubs. Therefore, we sought to identify cues that controlled the transition of immature neutrophils to the main hubs. We initially took advantage of a recently reported dataset containing the single-cell transcriptomes of lymph node leukocytes from mice treated with 86 different cytokines and growth factors (*27*) and performed an *in silico* screening by mapping the neutrophils from this dataset onto our NeuMap (Figure 4A). This approach provided several insights; first, many cytokines impacted the distribution of neutrophils within the NeuMap, but most induced profiles were associated with a single hub (Figure 4A). For example, interferons (IFN α, β, and γ) and IL36 directed neutrophils to the IFN-response hub, GM-CSF and APRIL to the IS-II hub, and IL1β, IL1α, and TNFα positioned neutrophils in a region between the IS-I and IS-II hubs (Figure 4A-B).

To validate these observations, we established a simple *in vitro* system in which BM neutrophils were exposed to a collection of 8 different cytokines or conditioned media from two cancer cell lines (LLC and FC1242 cell lines) for 24 and 48h. We used these short culture times to ensure high viability and minimum aging of immature BM-neutrophils and profiled the cells using a custom panel of 21 antibodies directed to markers encoded by genes expressed in different areas of the NeuMap and known to associate with defined functions (Figure 4C). This allowed us to categorize neutrophils into 5 possible profiles of maturation (Ly6G, CD101), inflammation/infection (PDL1, CD150, TLR4, and CX3CR1), immunosuppression (PDL1, CD14, CD11b) and cancer (PDL1, CD14, ICAM1, MHCII and dcTRAIL-R1) (Figure 4C and Extended Data Fig.76A-B). We found that the 8 cytokines and conditioned media yielded three prototypic profiles, which were typically stronger at 48h (Extended Data Fig.7C). The first phenotypic profile was induced by TGFβ treatment, which favoured neutrophil maturation (increased expression of CD101 and Ly6G); the second was exclusive of IFNβ and induced an inflammatory-like phenotype (PDL1^{HI}, CD14^{LO}, CX3CR1^{HI}); finally, the third profile was represented by GM-CSF, and resembled cancer-associated neutrophils (CD101^{LO}, PDL1^{HI}, CD14^{HI}, dcTRAIL-R1^{HI} and MHC-II^{+}) (Fig. 4C-E and Extended Data Fig.7A-C) as seen in lung tumors (Fig. 2K). Interestingly, tumor-conditioned media (LLC adenocarcinoma and KP pancreatic cancer) induced phenotypes that resembled GM-CSF treatment but were milder and more biased to the immunosuppressive phenotype (Fig. 4C-E and Extended Data Fig.7A-C). Of note, while most treatments did not affect or improved viability (G-CSF and PDAC-conditioned media), TNFα induced massive cell death (Extended Data Fig.7D), as expected from the known pro-apoptotic activity of this cytokine (*28*, *29*).

To assess whether these prototypical phenotypes mirrored transcriptional states present in the NeuMap, we generated single-cell transcriptomes of BM neutrophils cultured with TGFβ, IFNβ and GM-

CSF for 24h-48h, and projected them onto the NeuMap (Figure 4F). We found that TGFβ favored a transcriptional state along the main maturation pathway typical of the BM and blood (Figure 4F), IFNβ generated neutrophils that localized in the IFN-response hub, and exposure to GM-CSF positioned neutrophils in the *Cd274+Vegfa+* IS-II Hub (Figure 4F), altogether supporting our phenotypic analyses and strongly suggesting that these cytokines drive different transcriptional trajectories along the NeuMap (shown in Figure 3E). To test this possibility, we generated mice with neutrophil-specific deficiency in receptors for TGFβ (MRP8^{CRE}; *Tgfbr2*$^{fl/fl}$ or TgfbrΔN mice), type I-IFN (IfnarΔN mice) and GM-CSF (Csf2rΔN mice). Treatment of BM neutrophils from these mutant mice with TGFβ, IFNβ or GM-CSF prevented the phenotypic changes elicited by their respective cytokines (Figure 4G and Extended Data Fig.7E), resulting in reduced maturation-, inflammation- and cancer-associated phenotypes, respectively (Figure 4G and Extended Data Fig.7E). To confirm the requirement for these signaling pathways *in vivo*, we then performed scRNA-seq of neutrophils from the relevant tissues of TgfbrΔN (BM), IfnarΔN (blood) and Csfr2ΔN (LLC tumor) mice and their respective controls and mapped their distribution in the NeuMap. BM neutrophils from TgfbrΔN mice showed a delay in maturation, whereas the blood of IfnarΔN mice showed loss of the IFN-response hub, and neutrophils from tumors of Csf2rΔN mice shifted away from the IS-II hub (Figure 4H and Extended Data Fig.7F). These data confirmed that these cytokines reprogram neutrophils to specific transcriptional states defined in the NeuMap.

We took advantage of this defined regulation of neutrophil phenotypes to investigate the contribution of the different transcription factors identified in the chromatin accessibility assay (scATAC-seq). We used the HoxB8 system with CRISPR-mediated deletion of various transcription factors (*22*) to assess the extent to which each factor contributed to phenotypic transitions induced by the cytokines by multiparametric flow cytometry (Extended Data Fig.7G-H). Deletion of *Cebpb*, *Rfx2*, and *Runx1* impaired neutrophil maturation and subsequent cytokine-driven polarization. In contrast, *Irf5* was required for the Infection/inflammation profile, and *Relb* for the acquisition of the cancer/immunosuppressive phenotype in response to GM-CSF or PDAC-conditioned media. Finally, *Junb* deletion had broad effects on differentiation, including the IS-I/IS-II phenotype (Extended Data Fig.7G-H) and, importantly, this could be reinforced or partially rescued by ectopic expression of *Junb* in wild-type and *Junb*$^{-/-}$ HoxB cells, respectively (Extended Data Fig.7I-K). Together, these findings support the contention that the transcriptional states of the NeuMap are driven by defined cytokines, signaling pathways, and transcription factors. It also reveals redundancies and potential compensatory mechanisms that shape the response of neutrophils to stimulation.

In addition to identifying key signalling pathways, our *in vitro* strategy allowed us to isolate and functionally characterize neutrophils that fell in the various transcriptional states defined in the NeuMap. Hence, we treated BM neutrophils with vehicle, TGFβ, IFNβ or GM-CSF using the same conditions as above and assessed how these treatments affected core functions of neutrophils, including chemotaxis, phagocytosis, NET formation, as well as bactericidal, immunosuppressive or angiogenic activities (Figure 4I and Extended Data Fig.8). We found that TGFβ induced moderate migratory and immunosuppressive activities but none of the other properties, consistent with the patrolling and non-inflammatory properties of neutrophils in the healthy circulation. IFNβ, in contrast, impaired migration but activated phagocytosis and NET formation, suggesting activation of an antimicrobial program. Interestingly, although IFNβ induced only mild bactericidal activity (*S. aureus*), co-stimulation with TGFβ elicited a more potent response, suggesting that combinatorial or synergistic signaling may be needed for maturation and activation (Extended Data Fig.8B). Finally, GM-CSF also impaired migration and enhanced phagocytosis, and additionally activated immunosuppressive and angiogenic properties (Figure 4I and Extended Data Fig.8E-F), consistent with scenarios of tissue repair and cancer (*16*, *30*, *31*). Altogether, these assays validate the activity of the predicted functional hubs defined in the NeuMap and assigns a specific driver (cytokine) to each of these hubs.

In sum, we have identified a collection of cytokines involved in the maturation and specialization of neutrophils *in vitro* and *in vivo*. Our data suggest that the transcriptional transitions and acquisition of functional states (hubs) defined in the NeuMap are elicited by signals delivered by one or more cytokines through activation of defined downstream pathways, as illustrated here for TGFβ, IFNβ, GM-CSF, and Junb.

Predictive properties of the NeuMap

Given the rich transcriptional resolution of the NeuMap and the remarkable plasticity of the neutrophil compartment, we speculated that the map could be harnessed to visualize neutrophil states across species, pathophysiological conditions and response to therapies of the host.

We first examined signatures associated with favorable response to immunotherapy after anti-CD40 treatment in a mouse model of lung cancer (*31*). Visualization of these signatures onto the NeuMap revealed that lung neutrophils shifted from the Immuno-silent and IS-II hubs (typical of active cancer; Extended Data Fig.1F) towards the IFN-response hub in the responding group (Figure 5A). Interestingly, the distribution of these signatures also suggested that this shift might originate from an early change in the maturation paths of immature neutrophils (red arrows in Figure 5A), with activation of the alternative path seen in the context of acute inflammation (shown in Figure 3F).

We then explored whether the transcriptional hubs defined in the NeuMap persisted across species and associated with pathological states. To this end, we examined a collection of published human datasets of infection, autoimmunity, and cancer (Figure 5B and Extended Data Fig.9A) (*11*, *32*–*34*). By extracting the neutrophil signatures associated with disease outcome and visualizing them onto the NeuMap, we found that severe COVID-19 associated with neutrophils positioned in the PreNeu hub (Figure 5B). In contrast, neutrophils from the blood of individuals with active influenza infection or systemic lupus localized in the IFN-response hub (Figure 5B), and neutrophils from lung tumors (NSCLC) localized in the IS-II hub. Additional signatures or clusters identified in other cancer types (PDAC, hepatic cancer and glioblastoma) were predominant in areas of the NeuMap that suggested the presence of neutrophils associated with inflammatory, angiogenic, immunosuppressive or antigen-presenting activities (Extended Data Fig.9A), evidencing the heterogeneity of tumor-infiltrating neutrophils in human cancers. Of note, circulating neutrophils from healthy individuals showed a broad projection on the NeuMap that was not restricted to the Immuno-silent hub, likely reflecting the lack of a defined signature of blood neutrophils and highlighting potential limitations of the inter-species comparison. We then performed a reverse in silico experiment by selecting the gene signature from 6 transcriptional hubs of the NeuMap (the immune-silent hub was excluded because it lacks an associated specific signature) and examined the degree to which they predicted disease outcome in patients with two representative human cancers enriched in neutrophils, namely lung squamous carcinoma (LUSC) and pancreatic adenocarcinoma (PAAD), using the TCGA database (Extended Data Fig.9B). The associations varied depending on tumor type, with the IS-II signature consistently associating with poor outcome across cancers whereas the IFN-response signature only showed reduced patient survival in PAAD (Extended Data Fig.9B), likely reflecting the aggressive response of PDAC subtypes to interferon signalling (*34*). We confirmed this diversity of transcriptional responses depending on tumor type by examining the distribution of neutrophils extracted from mice with lung, pancreatic and breast cancer in the NeuMap (Extended Data Fig.9C). While these analyses only provided correlations with human disease, the similarity of the signatures defined in the NeuMap suggested that the response of neutrophils to infection, inflammation and cancer is largely conserved across disease types and species.

To examine this in more detail, we exposed human neutrophils differentiated from CD34+ progenitors to cytokines that induce the acquisition of hub-associated profiles in mouse neutrophils (Figure 4). Human neutrophils treated *in vitro* with IFNβ and GM-CSF acquired transcriptional states similar to those seen in mice, while the response to TGFβ only partially mirrored the maturation observed in mice

(Extended Data Fig. 9D). We complemented these *in vitro* assays with examination of the transcriptional profile of human neutrophils *in situ*, by performing high-resolution spatial transcriptomic analysis of 12 human lung specimens from healthy or tumor-bearing (lung adenocarcinoma) regions (Figure 5C). Clustering of the annotated neutrophils from this dataset identified five transcriptomic profiles (Clusters 1-5) that we could associate with different hubs from the NeuMap. This revealed, for example, that healthy lung tissue areas were enriched in neutrophils from Clusters 1 and 2, which associated with IS-I and Ag-presenting hubs (Figure 5C-D), respectively, in line with our analyses of the healthy murine lung tissue (Figure 1F). In contrast, tumoral regions were enriched in clusters 4 and 5, which shared features with the IS-II and Ag-presenting hubs, and areas adjacent to the tumors were enriched in cluster 3 neutrophils, which had features of the PreNeu / Immature hubs (Figure 5C-D). Neighbourhood analyses revealed a differential association of neutrophils from each cluster with other cell lineages *in vivo* (Extended Data Fig.9E). For example, cluster 3/immature neutrophils grouped with other neutrophils, cluster 1/IS-I neutrophils associated with AT2 alveolar cells, cluster 4/IS-II neutrophils with tumor-associated macrophages, and cluster 2 and 5 / Ag-presenting neutrophils were proximal to fibroblasts (Figure 5E). Combined, these analyses suggest phenotypic and functional conservation of murine and human neutrophils, and distinct *in vivo* spatial distributions of neutrophils from each hub.

Finally, we examined whether the distribution of blood neutrophils in the NeuMap could help predict the pathophysiological state of the host. To this end, we performed scRNA-seq of neutrophils from the blood of mice exposed to 18 different conditions, including various stages of cancer (LLC 1, 2 or 3 weeks after implantation, and PDAC at humane end-point), microbial infections (viral and bacterial), sterile inflammation (hepatic injury, colitis, and hypercholesterolemia), or physiological states (pregnancy, old age, and embryonic life) (Figure 5F). We then visualized the distribution of the sequenced cells in two ways: in a UMAP embedding built only using the blood cells, or by mapping them onto the full NeuMap space (Fig 5G and Extended Data Fig.10A). We inferred the transcriptional hubs associated with each sample and found that all hubs (Figure 1F) were represented in at least one of the blood samples (Extended Data Fig.10B). We found that the projection onto the NeuMap dramatically reduced the overlap of the cells and their respective hubs when compared with the blood-only map, as quantified using the Bhattacharyya index (Figure 5G). This reduced overlap allowed better discrimination between the 18 physiological conditions and suggested that the NeuMap could be used as a scaffold to obtain unique distributions of blood neutrophils and to infer the patho-physiological state of the host. To examine this possibility, we generated 10 “diagnostic regions” in the NeuMap. These regions do not contain biological information but improved the spatial resolution and separability of the samples when compared with the 7 transcriptional hubs, which contain biological information but perform poorly for spatial discrimination (Extended Data Fig.10C). We used the overlapping distribution of blood neutrophils from each condition over these 10 regions (illustrated in Extended Data Fig.10D) and employed the Bhattacharyya index to generate distribution “barcodes” that were unique for each sample (Figure 5H). For example, the barcodes could discriminate healthy males from older (80-week-old) males, pregnant females, athero-prone *Apoe*$^{-/-}$ mice or from early onset cancer (one-week post-tumor implantation). Likewise, we could distinguish mice bearing different types of tumors (pancreatic vs. lung), or mice infected with viral (influenza) versus bacterial (*S. aureus*) or fungal (*C.albicans*) pathogens, as well as mice with active liver cholestasis versus those in remission. The differential profiles seen in blood across these conditions or across tissues (Figure 1F) highlight the adaptability of neutrophils to local and systemic cues. Collectively, these analyses demonstrate that the NeuMap captures the transcriptional diversity of neutrophils with enough resolution to allow inferring host physiology by simply assessing the distribution of blood neutrophils. This property may hold significant diagnostic potential and benefit from examination of many other physiological scenarios.

Discussion

Here, we have used single-cell transcriptomics to build a transcriptional map of the mouse neutrophil compartment across organs, developmental stages, and pathological and physiological conditions (the

NeuMap). This allowed us to gain new insights into its molecular and functional architecture and to demonstrate that, despite the wealth of transcriptional clusters reported in the literature (*3*, *6*, *7*, *16*, *18*, *35*, *36*), the neutrophil compartment is organized as a finite collection of transcriptional states that can be associated with recognizable biological properties (referred to here as transcriptional hubs). By visualizing the distribution of neutrophils across the NeuMap and combining this information with timestamp techniques *in vivo*, we identify prototypical trajectories connecting the hubs that are differentially transited during health, cancer, and inflammation. We report a collection of cues and transcriptional regulators that push neutrophils along these prototypical trajectories and instruct distinct functional properties. These trajectories and hubs are associated with distinct physiological states and appear to be conserved between mice and humans, supporting the use of the NeuMap as a powerful discovery tool and a potential platform for diagnosis (Extended Data Fig. 11).

The exploration and expansion of the NeuMap are still ongoing, and we expect it to be a long-term effort in the field. For example, we foresee extension of this mapping during organismal development and aging, pathological states associated with inflammation, and to other species. Further exploration and validation of the NeuMap will also benefit from *in vitro* and synthetic systems, such as the HoxB8 or iPSC models. Here, we limit our discussion to three salient features that we believe shed fundamental new insights into the biology of neutrophils. First, the transcriptome of the neutrophil compartment is organized as a single structure without obvious branching or separated clusters. Although this might appear to conflict with the various trajectories seen inside the NeuMap (Figure 3), we propose that this structure does not imply a single path of maturation. Instead, we propose that it reflects the neutrophils' unique life cycle. Indeed, the short lifespan of neutrophils (0.5 to ~5 days, depending on tissue and context (*4*, *16*)) demands active granulopoiesis and continuous replenishment of the entire compartment, implying that immature, intermediate, and final transcriptional states can be captured at any given time, including in pathological conditions of cancer and inflammation in which their production is accelerated (*37*). Because these intermediate states "occupy" the space between the transcriptional hubs, they prevent visualization of the final maturation states as separate clusters. Contrasting with neutrophils, we predict that similar mapping of longer-lived lineages, such as macrophages, would reveal clear branching points and separated clusters corresponding to extreme, long-lived differentiation states reported in tissues, which in turn are the consequence of tissue seeding by macrophage precursors during embryonic life and, in adult life, are independent of marrow-derived myelopoiesis (*38*, *39*).

Second, the NeuMap reveals several functional hubs, mirroring the heterogeneity of neutrophil states reported in multiple studies (*4*, *6*, *7*, *16*, *18*, *35*, *40*). The relatively low number of hubs, however, contrasts with the remarkable diversity of infectious, inflammatory, tumoral and homeostatic scenarios in which neutrophils play significant roles. When combined with their high transcriptional plasticity (*3*), one could have expected a much larger number of transcriptional hubs. The integration of many conditions into a single dataset, however, narrowed down this diversity to a few biological states and illuminated common physiological responses that are independent of specific perturbations. For example, we find that many of the "clusters" and cell populations reported in different studies share similar gene signatures associated with tissue repair and cancer that have received different names, including angiogenic neutrophils, myeloid-derived suppressor cells, activated tumor-associated neutrophils or T3 cells (*4*, *11*, *16*, *30*, *41*, *42*). These populations show similar, if not identical, distribution in the NeuMap, suggesting that they may represent the same biological state. In this line of thought, we show that neutrophils that share similar transcriptional profiles (marked by expression of *Cd14* and *Ptgs2*) exist in several tissues, including lung, gut, liver, and placenta, suggesting convergent instructing microenvironments and signals in those organs. Hence, we propose that the NeuMap could be used as a reference platform to uncover core properties of neutrophils.

Third, we emphasize the transcriptional dynamism of the NeuMap. Rather than defining static transcriptional profiles using traditional clustering algorithms, we harnessed computational prediction tools and timestamp analyses to illuminate trajectories connecting the different transcriptional hubs. We propose that the structure of our transcriptional map should be interpreted in terms of dynamic biological programs. A practical implication of this model is that it focuses on identifying the source state for each trajectory, including those that give rise to pathogenic states. This approach highlights the notion that interfering with the source of the different trajectories may be more effective than targeting terminally differentiated neutrophils, a strategy that still dominates neutrophil-based therapies (*1*). Illustrating this concept, we show that systemic inflammation generates neutrophils through a maturation path that diverges from normal granulopoiesis rather than by simply activating mature cells, whereas cancer appears to generate new trajectories stemming from already mature neutrophils. Finally, this dynamic interpretation provides a better grasp of how cytokines (and their receptors or signalling mediators) control maturation. For example, the finding that TGFβ, IFNβ and GM-CSF control different trajectories that are interconnected suggests that interfering with a particular trajectory may reroute maturation through an alternative path, in turn favoring the generation of neutrophils with new properties.

Despite the insights gained on the structure and dynamics of the neutrophil compartment, our study has several limitations. Foremost is that the NeuMap has been built using one strain of a single species (C57BL/6 mice) and, despite the evidence that key hub signatures are maintained in humans, it will be important to validate the extent to which the same architecture persists across other strains and species. Similarly, we have extracted neutrophils from a broad collection of tissues and from multiple pathological and physiological conditions that remain, however, incomplete. Perturbations and programs associated with allergy, autoimmunity, infiltration of mucosal surfaces, or diseases associated with old age (*43–47*), as well as neutrophils from many other tissues, remain uncharted in our NeuMap. Thus, we cannot exclude the presence of additional states, trajectories, and functional properties that will be important to incorporate as we continue to expand this map and understand the intricacies of the neutrophil compartment. We have also focused here on a relatively small collection of cytokines and transcriptional regulators that control the distribution and dynamics of neutrophils in the NeuMap; it is likely, however, that additional cues (including cytokines, chemokines, signaling lipids, and metabolites), activating stimuli (e.g., those associated with adhesion, circadian rhythms, mechano-stimulation or inhibitory receptors (*48–51*), and transcriptional regulators contribute to the specification of neutrophils and this will need to be tested in future studies. Finally, the spatial and anatomical associations with neutrophil states shown here will benefit from higher resolution and diversity of anatomical and pathological scenarios to understand where and how neutrophils “read” their environment to acquire new properties, as proposed in the healthy lung and spleen, where vascular niches (*16*) and subcapsular regions (*7*) instruct immunosuppressive and IFN-response signatures, respectively.

In summary, the integrative nature of the NeuMap should offer a powerful tool to uncover new features of neutrophils, including the source and breadth of their diversity, dynamics, and diagnostic potential. Our study highlights the collective nature of this immune compartment and hints that the properties of the collective differ from the sum of its individual components, a notion that may have a major impact on understanding its evolutionary “logic” and in defining how neutrophils contribute to health and disease.

References

1. A. Aroca-crevillén, T. Vicanolo, S. Ovadia, A. Hidalgo, Neutrophils in Physiology and Pathology. *Annu. Rev. Pathol. Mech. Dis.* **19**, 227–259 (2024).
2. M. Casanova-Acebes, J. A. Nicolás-Ávila, J. L. Yao Li, S. García-Silva, A. Balachander, A. Rubio-Ponce, L. A. Weiss, J. M. Adrover, K. Burrows, N. A-González, I. Ballesteros, S. Devi, J. A. Quintana, G. Crainiciuc, M. Leiva, M. Gunzer, C. Weber, T. Nagasawa, O. Soehnlein, M. Merad, A. Mortha, L. G. Ng, H. Peinado, A. Hidalgo, Neutrophils instruct homeostatic and pathological states in naive tissues. *J. Exp. Med.* **215**, 2778–2795 (2018).
3. L. G. Ng, R. Ostuni, A. Hidalgo, Heterogeneity of neutrophils. *Nat. Rev. Immunol.* **19** (2019), pp. 255–265.
4. M. S. F. Ng, I. Kwok, L. Tan, C. Shi, D. Cerezo-Wallis, Y. Tan, K. Leong, G. F. Calvo, K. Yang, Y. Zhang, J. Jin, K. H. Liong, D. Wu, R. He, D. Liu, Y. C. Teh, C. Bleriot, N. Caronni, Z. Liu, K. Duan, V. Narang, I. Ballesteros, F. Moalli, M. Li, J. Chen, Y. Liu, L. Liu, J. Qi, Y. Liu, L. Jiang, B. Shen, H. Cheng, T. Cheng, V. Angeli, A. Sharma, Y.-H. Loh, H. L. Tey, S. Z. Chong, M. Iannacone, R. Ostuni, A. Hidalgo, F. Ginhoux, L. G. Ng, Deterministic reprogramming of neutrophils within tumors. *Science*. **383**, eadf6493 (2024).
5. D. F. Quail, B. Amulic, M. Aziz, B. J. Barnes, E. Eruslanov, Z. G. Fridlender, H. S. Goodridge, Z. Granot, A. Hidalgo, A. Huttenlocher, M. J. Kaplan, I. Malanchi, T. Merghoub, E. Meylan, V. Mittal, M. J. Pittet, A. Rubio-Ponce, I. A. Udalova, T. K. van den Berg, D. D. Wagner, P. Wang, A. Zychlinsky, K. E. de Visser, M. Egeblad, P. Kubes, Neutrophil phenotypes and functions in cancer: A consensus statement. *J. Exp. Med.* **219**, 1–23 (2022).
6. S. Salcher, G. Sturm, L. Horvath, G. Untergasser, C. Kuempers, G. Fotakis, E. Panizzolo, A. Martowicz, M. Trebo, G. Pall, G. Gamerith, M. Sykora, F. Augustin, K. Schmitz, F. Finotello, D. Rieder, S. Perner, S. Sopper, D. Wolf, A. Pircher, Z. Trajanoski, High-resolution single-cell atlas reveals diversity and plasticity of tissue-resident neutrophils in non-small cell lung cancer. *Cancer Cell*. **40**, 1503-1520.e8 (2022).
7. X. Xie, Q. Shi, P. Wu, X. Zhang, H. Kambara, J. Su, H. Yu, S. Y. Park, R. Guo, Q. Ren, S. Zhang, Y. Xu, L. E. Silberstein, T. Cheng, F. Ma, C. Li, H. R. Luo, Single-cell transcriptome profiling reveals neutrophil heterogeneity in homeostasis and infection. *Nat. Immunol.* **21** (2020), doi:10.1038/s41590-020-0736-z.
8. I. Kwok, E. Becht, Y. Xia, M. Ng, Y. C. Teh, L. Tan, M. Evrard, J. L. Y. Li, H. T. N. Tran, Y. Tan, D. Liu, A. Mishra, K. H. Liong, K. Leong, Y. Zhang, A. Olsson, C. K. Mantri, P. Shyamsunder, Z. Liu, C. Piot, C.-A. Dutertre, H. Cheng, S. Bari, N. Ang, S. K. Biswas, H. P. Koeffler, H. L. Tey, A. Larbi, I.-H. Su, B. Lee, A. St John, J. K. Y. Chan, W. Y. K. Hwang, J. Chen, N. Salomonis, S. Z. Chong, H. L. Grimes, B. Liu, A. Hidalgo, E. W. Newell, T. Cheng, F. Ginhoux, L. G. Ng, Combinatorial Single-Cell Analyses of Granulocyte-Monocyte Progenitor Heterogeneity Reveals an Early Uni-potent Neutrophil Progenitor. *Immunity*. **53**, 303-318.e5 (2020).
9. A. Hidalgo, E. R. Chilvers, C. Summers, L. Koenderman, The Neutrophil Life Cycle. *Trends Immunol.* **40** (2019), pp. 584–597.
10. R. Grieshaber-Bouyer, F. A. Radtke, P. Cunin, G. Stifano, A. Levescot, B. Vijaykumar, N. Nelson-Maney, R. B. Blaustein, P. A. Monach, P. A. Nigrovic, O. Aguilar, R. Allan, J. Astarita, K. F. Austen, N. Barrett, A. Baysoy, C. Benoist, B. D. Brown, M. Buechler, J. Buenrostro, M. A. Casanova, K. Chowdhary, M. Colonna, T. Crowl, T. Deng, F. Desland, M. Dhainaut, J. Ding, C. Dominguez, D. Dwyer, M. Frascoli, S. Gal-Oz, A. Goldrath, T. Johanson, S. Jordan, J. Kang, V. Kapoor, E. Kenigsberg, J. Kim, K. wook Kim, E. Kiner, M. Kronenberg, L. Lanier, C. Laplace, C. Lareau, A. Leader, J. Lee, A. Magen, B. Maier, A. Maslova, D. Mathis, A. McFarland, M. Merad, E. Meunier, P. A. Monach, S. Mostafavi, S. Muller, C. Muus, H. Ner-Gaon, Q. Nguyen, G. Novakovsky, S. Nutt, K. Omilusik, A. Ortiz-Lopez, M. Paynich, V. Peng, M. Potempa, R. Pradhan, S. Quon, R. Ramirez, D. Ramanan, G. Randolph, A. Regev, S. A. Rose, K. Seddu, T. Shay, A. Shemesh, J. Shyer, C. Smilie, N. Spidale, A. Subramanian, K. Sylvia, J. Tellier, S. Turley, B. Vijaykumar, A. Wagers, C. Wang, P. L. Wang, A. Wroblewska, L. Yang, A. Yim, H. Yoshida, I. Consortium, The neutrotime transcriptional signature defines a single continuum of neutrophils across biological compartments. *Nat. Commun.* **12**, 2856 (2021).
11. R. Zilionis, C. Engblom, C. Pfirschke, V. Savova, D. Zemmour, H. D. Saatcioglu, I. Krishnan, G. Maroni, C. V. Meyerovitz, C. M. Kerwin, S. Choi, W. G. Richards, A. De Rienzo, D. G. Tenen, R. Bueno, E. Levantini, M. J. Pittet, A. M. Klein, Single-Cell Transcriptomics of Human and Mouse Lung Cancers Reveals Conserved Myeloid Populations across Individuals and Species. *Immunity*. **50**, 1317-1334.e10

(2019).

12. M. Evrard, I. W. H. Kwok, S. Z. Chong, K. W. W. Teng, E. Becht, J. Chen, J. L. Sieow, H. L. Penny, G. C. Ching, S. Devi, J. M. Adrover, J. L. Y. Li, K. H. Liong, L. Tan, Z. Poon, S. Foo, J. W. Chua, I.-H. Su, K. Balabanian, F. Bachelerie, S. K. Biswas, A. Larbi, W. Y. K. Hwang, V. Madan, H. P. Koeffler, S. C. Wong, E. W. Newell, A. Hidalgo, F. Ginhoux, L. G. Ng, Developmental Analysis of Bone Marrow Neutrophils Reveals Populations Specialized in Expansion, Trafficking, and Effector Functions. *Immunity*. **48**, 364-379.e8 (2018).

13. L. Grassi, F. Pourfarzad, S. Ullrich, A. Merkel, F. Were, E. Carrillo-de-Santa-Pau, G. Yi, I. H. Hiemstra, A. T. J. Tool, E. Mul, J. Perner, E. Janssen-Megens, K. Berentsen, H. Kerstens, E. Habibi, M. Gut, M. L. Yaspo, M. Linser, E. Lowy, A. Datta, L. Clarke, P. Flicek, M. Vingron, D. Roos, T. K. van den Berg, S. Heath, D. Rico, M. Frontini, M. Kostadima, I. Gut, A. Valencia, W. H. Ouwehand, H. G. Stunnenberg, J. H. A. Martens, T. W. Kuijpers, Dynamics of Transcription Regulation in Human Bone Marrow Myeloid Differentiation to Mature Blood Neutrophils. *Cell Rep.* **24**, 2784–2794 (2018).

14. T. Morrison, E. R. Watts, P. Sadiku, S. R. Walmsley, The emerging role for metabolism in fueling neutrophilic inflammation. *Immunol. Rev.* **314** (2023), pp. 427–441.

15. R. Morosetti, D. J. Park, A. M. Chumakov, I. Grillier, M. Shiohara, A. F. Gombart, T. Nakamki, K. Weinberg, H. P. Koeffler, A novel, myeloid transcription factor, C/EBP epsilon, is upregulated during granulocytic, but not monocytic, differentiation. *Blood*. **90**, 2591–2600 (1997).

16. I. Ballesteros, A. Rubio-Ponce, M. Genua, E. Lusito, I. Kwok, G. Fernández-Calvo, T. E. Khoyratty, E. van Grinsven, S. González-Hernández, J. Á. Nicolás-Ávila, T. Vicanolo, A. Maccataio, A. Benguría, J. L. Li, J. M. Adrover, A. Aroca-Crevillen, J. A. Quintana, S. Martín-Salamanca, F. Mayo, S. Ascher, G. Barbiera, O. Soehnlein, M. Gunzer, F. Ginhoux, F. Sánchez-Cabo, E. Nistal-Villán, C. Schulz, A. Dopazo, C. Reinhardt, I. A. Udalova, L. G. Ng, R. Ostuni, A. Hidalgo, Co-option of Neutrophil Fates by Tissue Environments. *Cell*. **183** (2020), doi:10.1016/j.cell.2020.10.003.

17. M. Vono, A. Lin, A. Norrby-Teglund, R. A. Koup, F. Liang, K. Loré, Neutrophils acquire the capacity for antigen presentation to memory CD4+ T cells in vitro and ex vivo. *Blood*. **129**, 1991–2001 (2017).

18. Y. Wu, J. Ma, X. Yang, F. Nan, T. Zhang, S. Ji, D. Rao, H. Feng, K. Gao, X. Gu, S. Jiang, G. Song, J. Pan, M. Zhang, Y. Xu, S. Zhang, Y. Fan, X. Wang, J. Zhou, L. Yang, J. Fan, X. Zhang, Q. Gao, Neutrophil profiling illuminates anti-tumor antigen-presenting potency. *Cell*. **187**, 1422-1439.e24 (2024).

19. S. Singhal, P. S. Bhojnagarwala, S. O'Brien, E. K. Moon, A. L. Garfall, A. S. Rao, J. G. Quatromoni, T. L. Stephen, L. Litzky, C. Deshpande, M. D. Feldman, W. W. Hancock, J. R. Conejo-Garcia, S. M. Albelda, E. B. Eruslanov, Origin and Role of a Subset of Tumor-Associated Neutrophils with Antigen-Presenting Cell Features in Early-Stage Human Lung Cancer. *Cancer Cell*. **30**, 120–135 (2016).

20. J. J. Fuster, S. MacLauchlan, M. A. Zuriaga, M. N. Polackal, A. C. Ostriker, R. Chakraborty, C. L. Wu, S. Sano, S. Muralidharan, C. Rius, J. Vuong, S. Jacob, V. Muralidhar, A. A. B. Robertson, M. A. Cooper, V. Andrés, K. K. Hirschi, K. A. Martin, K. Walsh, Clonal hematopoiesis associated with TET2 deficiency accelerates atherosclerosis development in mice. *Science (80-.).* **355**, 842–847 (2017).

21. E. P. Mimitou, C. A. Lareau, K. Y. Chen, A. L. Zorzetto-Fernandes, Y. Hao, Y. Takeshima, W. Luo, T. S. Huang, B. Z. Yeung, E. Papalexi, P. I. Thakore, T. Kibayashi, J. B. Wing, M. Hata, R. Satija, K. L. Nazor, S. Sakaguchi, L. S. Ludwig, V. G. Sankaran, A. Regev, P. Smibert, *Scalable, multimodal profiling of chromatin accessibility, gene expression and protein levels in single cells* (Springer US, 2021; http://dx.doi.org/10.1038/s41587-021-00927-2), vol. 39.

22. T. E. Khoyratty, Z. Ai, I. Ballesteros, H. L. Eames, S. Mathie, S. Martín-Salamanca, L. Wang, A. Hemmings, N. Willemsen, V. von Werz, A. Zehrer, B. Walzog, E. van Grinsven, A. Hidalgo, I. A. Udalova, Distinct transcription factor networks control neutrophil-driven inflammation. *Nat. Immunol.* **22** (2021), doi:10.1038/s41590-021-00968-4.

23. N. Horrée, P. J. van Diest, D. M. D. S. Sie-Go, A. P. M. Heintz, The invasive front in endometrial carcinoma: higher proliferation and associated derailment of cell cycle regulators. *Hum. Pathol.* **38**, 1232–1238 (2007).

24. S. Yamada, T. Ko, S. Hatsuse, S. Nomura, B. Zhang, Z. Dai, S. Inoue, M. Kubota, K. Sawami, T. Yamada, T. Sassa, M. Katagiri, K. Fujita, M. Katoh, M. Ito, M. Harada, H. Toko, N. Takeda, H. Morita, H. Aburatani, I. Komuro, Spatiotemporal transcriptome analysis reveals critical roles for mechano-sensing genes at the border zone in remodeling after myocardial infarction. *Nat. Cardiovasc. Res.* **1**, 1072–1083 (2022).

25. A. J. Hoogendijk, F. Pourfarzad, C. E. M. Aarts, A. T. J. Tool, I. H. Hiemstra, L. Grassi, M. Frontini, A. B.

Meijer, M. van den Biggelaar, T. W. Kuijpers, Dynamic Transcriptome-Proteome Correlation Networks Reveal Human Myeloid Differentiation and Neutrophil-Specific Programming. *Cell Rep.* **29**, 2505-2519.e4 (2019).

26. M. Benguigui, T. J. Cooper, P. Kalkar, S. Schif-Zuck, R. Halaban, A. Bacchiocchi, I. Kamer, A. Deo, B. Manobla, R. Menachem, J. Haj-Shomaly, A. Vorontsova, Z. Raviv, C. Buxbaum, P. Christopoulos, J. Bar, M. Lotem, M. Sznol, A. Ariel, S. S. Shen-Orr, Y. Shaked, Interferon-stimulated neutrophils as a predictor of immunotherapy response. *Cancer Cell*, 1–13 (2023).

27. A. Cui, T. Huang, S. Li, A. Ma, J. L. Pérez, C. Sander, D. B. Keskin, C. J. Wu, E. Fraenkel, N. Hacohen, Dictionary of immune responses to cytokines at single-cell resolution. *Nature*. **625**, 377–384 (2024).

28. G. Salamone, M. Giordano, A. S. Trevani, R. Gamberale, M. Vermeulen, J. Schettinni, J. R. Geffner, Promotion of Neutrophil Apoptosis by TNF-α. *J. Immunol.* **166**, 3476–3483 (2001).

29. B. J. Van Raam, A. Drewniak, V. Groenewold, T. K. Van Den Berg, T. W. Kuijpers, Granulocyte colony-stimulating factor delays neutrophil apoptosis by inhibition of calpains upstream of caspase-3. *Blood*. **112**, 2046–2054 (2008).

30. F. Veglia, A. Hashimoto, H. Dweep, E. Sanseviero, A. de Leo, E. Tcyganov, A. Kossenkov, C. Mulligan, B. Nam, G. Masters, J. Patel, V. Bhargava, P. Wilkinson, D. Smirnov, M. A. Sepulveda, S. Singhal, E. B. Eruslanov, R. Cristescu, A. Loboda, Y. Nefedova, D. I. Gabrilovich, Analysis of classical neutrophils and polymorphonuclear myeloid-derived suppressor cells in cancer patients and tumor-bearing mice. *J. Exp. Med.* **218** (2021), doi:10.1084/JEM.20201803.

31. J. Gungabeesoon, N. A. Gort-Freitas, M. Kiss, E. Bolli, M. Messemaker, M. Siwicki, M. Hicham, R. Bill, P. Koch, C. Cianciaruso, F. Duval, C. Pfirschke, M. Mazzola, S. Peters, K. Homicsko, C. Garris, R. Weissleder, A. M. Klein, M. J. Pittet, A neutrophil response linked to tumor control in immunotherapy. *Cell*. **186**, 1448-1464.e20 (2023).

32. Y. Zhang, L. Zong, Y. Zheng, Y. Zhang, N. Li, Y. Li, Y. Jin, L. Chen, J. Ouyang, A. Bibi, Y. Huang, Y. Xu, A single-cell atlas of the peripheral immune response in patients with influenza A virus infection. *iScience*. **26**, 108507 (2023).

33. J. E. Wither, S. D. Prokopec, B. Noamani, N.-H. Chang, D. Bonilla, Z. Touma, C. Avila-Casado, H. N. Reich, J. Scholey, P. R. Fortin, P. C. Boutros, C. Landolt-Marticorena, Identification of a neutrophil-related gene expression signature that is enriched in adult systemic lupus erythematosus patients with active nephritis: Clinical/pathologic associations and etiologic mechanisms. *PLoS One*. **13**, e0196117 (2018).

34. E. Espinet, Z. Gu, C. D. Imbusch, N. A. Giese, M. Büscher, M. Safavi, S. Weisenburger, C. Klein, V. Vogel, M. Falcone, J. Insua-Rodríguez, M. Reitberger, V. Thiel, S. O. Kossi, A. Muckenhuber, K. Sarai, A. Y. L. Lee, E. Backx, S. Zarei, M. M. Gaida, M. Rodríguez-Paredes, E. Donato, H.-Y. Yen, R. Eils, M. Schlesner, N. Pfarr, T. Hackert, C. Plass, B. Brors, K. Steiger, D. Weichenhan, H. E. Arda, I. Rooman, J. L. Kopp, O. Strobel, W. Weichert, M. R. Sprick, A. Trumpp, Aggressive PDACs Show Hypomethylation of Repetitive Elements and the Execution of an Intrinsic IFN Program Linked to a Ductal Cell of Origin. *Cancer Discov.* **11**, 638–659 (2021).

35. R. Xue, Q. Zhang, Q. Cao, R. Kong, X. Xiang, H. Liu, M. Feng, F. Wang, J. Cheng, Z. Li, Q. Zhan, M. Deng, J. Zhu, Z. Zhang, N. Zhang, Liver tumour immune microenvironment subtypes and neutrophil heterogeneity. *Nature*. **612**, 141–147 (2022).

36. J. Schulte-Schrepping, N. Reusch, D. Paclik, K. Baßler, S. Schlickeiser, B. Zhang, B. Krämer, T. Krammer, S. Brumhard, L. Bonaguro, E. De Domenico, D. Wendisch, M. Grasshoff, T. S. Kapellos, M. Beckstette, T. Pecht, A. Saglam, O. Dietrich, H. E. Mei, A. R. Schulz, C. Conrad, D. Kunkel, E. Vafadarnejad, C. J. Xu, A. Horne, M. Herbert, A. Drews, C. Thibeault, M. Pfeiffer, S. Hippenstiel, A. Hocke, H. Müller-Redetzky, K. M. Heim, F. Machleidt, A. Uhrig, L. Bosquillon de Jarcy, L. Jürgens, M. Stegemann, C. R. Glösenkamp, H. D. Volk, C. Goffinet, M. Landthaler, E. Wyler, P. Georg, M. Schneider, C. Dang-Heine, N. Neuwinger, K. Kappert, R. Tauber, V. Corman, J. Raabe, K. M. Kaiser, M. T. Vinh, G. Rieke, C. Meisel, T. Ulas, M. Becker, R. Geffers, M. Witzenrath, C. Drosten, N. Suttorp, C. von Kalle, F. Kurth, K. Händler, J. L. Schultze, A. C. Aschenbrenner, Y. Li, J. Nattermann, B. Sawitzki, A. E. Saliba, L. E. Sander, A. Angelov, R. Bals, A. Bartholomäus, A. Becker, D. Bezdan, E. Bonifacio, P. Bork, T. Clavel, M. Colome-Tatche, A. Diefenbach, A. Dilthey, N. Fischer, K. Förstner, J. S. Frick, J. Gagneur, A. Goesmann, T. Hain, M. Hummel, S. Janssen, J. Kalinowski, R. Kallies, B. Kehr, A. Keller, S. Kim-Hellmuth, C. Klein, O. Kohlbacher, J. O. Korbel, I. Kurth, K. Ludwig, O. Makarewicz, M. Marz, A. McHardy, C. Mertes, M. Nöthen, P. Nürnberg, U. Ohler, S. Ossowski, J. Overmann, S. Peter, K. Pfeffer, A. R. Poetsch, A. Pühler, N. Rajewsky, M. Ralser, O. Rieß, S. Ripke, U. Nunes da Rocha, P. Rosenstiel, P. Schiffer, E. C. Schulte, A. Sczyrba, O. Stegle, J. Stoye, F. Theis, J.

Vehreschild, J. Vogel, M. von Kleist, A. Walker, J. Walter, D. Wieczorek, J. Ziebuhr, Severe COVID-19 Is Marked by a Dysregulated Myeloid Cell Compartment. *Cell*. **182** (2020), doi:10.1016/j.cell.2020.08.001.

37. M. G. Manz, S. Boettcher, Emergency granulopoiesis. *Nat. Rev. Immunol.* **14** (2014), pp. 302–314.

38. Y. Lavin, D. Winter, R. Blecher-Gonen, E. David, H. Keren-Shaul, M. Merad, S. Jung, I. Amit, Tissue-resident macrophage enhancer landscapes are shaped by the local microenvironment. *Cell*. **159**, 1312–1326 (2014).

39. Z. Liu, Y. Gu, S. Chakarov, C. Bleriot, I. Kwok, X. Chen, A. Shin, W. Huang, R. J. Dress, C. A. Dutertre, A. Schlitzer, J. Chen, L. G. Ng, H. Wang, Z. Liu, B. Su, F. Ginhoux, Fate Mapping via Ms4a3-Expression History Traces Monocyte-Derived Cells. *Cell*. **178**, 1509-1525.e19 (2019).

40. L. Wang, Y. Liu, Y. Dai, X. Tang, T. Yin, C. Wang, T. Wang, L. Dong, M. Shi, J. Qin, M. Xue, Y. Cao, J. Liu, P. Liu, J. Huang, C. Wen, J. Zhang, Z. Xu, F. Bai, X. Deng, C. Peng, H. Chen, L. Jiang, S. Chen, B. Shen, Single-cell RNA-seq analysis reveals BHLHE40-driven pro-tumour neutrophils with hyperactivated glycolysis in pancreatic tumour microenvironment. *Gut*, 1–14 (2022).

41. F. Veglia, V. A. Tyurin, M. Blasi, A. De Leo, A. V. Kossenkov, L. Donthireddy, T. K. J. To, Z. Schug, S. Basu, F. Wang, E. Ricciotti, C. DiRusso, M. E. Murphy, R. H. Vonderheide, P. M. Lieberman, C. Mulligan, B. Nam, N. Hockstein, G. Masters, M. Guarino, C. Lin, Y. Nefedova, P. Black, V. E. Kagan, D. I. Gabrilovich, Fatty acid transport protein 2 reprograms neutrophils in cancer. *Nature*. **569**, 73–78 (2019).

42. Z. G. Fridlender, J. Sun, S. Kim, V. Kapoor, G. Cheng, L. Ling, G. S. Worthen, S. M. Albelda, Polarization of Tumor-Associated Neutrophil Phenotype by TGF-β: “N1” versus “N2” TAN. *Cancer Cell*. **16**, 183–194 (2009).

43. K. Van Avondt, J. K. Strecker, C. Tulotta, J. Minnerup, C. Schulz, O. Soehnlein, Neutrophils in aging and aging-related pathologies. *Immunol. Rev.* **314**, 357–375 (2023).

44. S. Gupta, M. J. Kaplan, The role of neutrophils and NETosis in autoimmune and renal diseases. *Nat. Rev. Nephrol.* **12**, 402–413 (2016).

45. L. Bennett, A. K. Palucka, E. Arce, V. Cantrell, J. Borvak, J. Banchereau, V. Pascual, Interferon and granulopoiesis signatures in systemic lupus erythematosus blood. *J. Exp. Med.* **197**, 711–723 (2003).

46. J. Woytschak, N. Keller, C. Krieg, D. Impellizzieri, R. W. Thompson, T. A. Wynn, A. S. Zinkernagel, O. Boyman, Type 2 Interleukin-4 Receptor Signaling in Neutrophils Antagonizes Their Expansion and Migration during Infection and Inflammation. *Immunity*. **45**, 172–184 (2016).

47. A. Özcan, O. Boyman, Mechanisms regulating neutrophil responses in immunity, allergy, and autoimmunity. *Allergy Eur. J. Allergy Clin. Immunol.* **77**, 3567–3583 (2022).

48. B. Favier, Regulation of neutrophil functions through inhibitory receptors: an emerging paradigm in health and disease. *Immunol. Rev.* **273**, 140–155 (2016).

49. A. Mukhopadhyay, Y. Tsukasaki, W. C. Chan, J. P. Le, M. L. Kwok, J. Zhou, V. Natarajan, N. Mostafazadeh, M. Maienschein-Cline, I. Papautsky, C. Tiruppathi, Z. Peng, J. Rehman, B. Ganesh, Y. Komarova, A. B. Malik, trans-Endothelial neutrophil migration activates bactericidal function via Piezo1 mechanosensing. *Immunity*. **57**, 52-67.e10 (2024).

50. J. M. Adrover, C. del Fresno, G. Crainiciuc, M. I. Cuartero, M. Casanova-Acebes, L. A. Weiss, H. Huerga-Encabo, C. Silvestre-Roig, J. Rossaint, I. Cossío, A. V. Lechuga-Vieco, J. García-Prieto, M. Gómez-Parrizas, J. A. Quintana, I. Ballesteros, S. Martin-Salamanca, A. Aroca-Crevillen, S. Z. Chong, M. Evrard, K. Balabanian, J. López, K. Bidzhekov, F. Bachelerie, F. Abad-Santos, C. Muñoz-Calleja, A. Zarbock, O. Soehnlein, C. Weber, L. G. Ng, C. Lopez-Rodriguez, D. Sancho, M. A. Moro, B. Ibáñez, A. Hidalgo, A Neutrophil Timer Coordinates Immune Defense and Vascular Protection. *Immunity*. **50** (2019), doi:10.1016/j.immuni.2019.01.002.

51. A. Zarbock, K. Ley, Neutrophil adhesion and activation under flow. *Microcirculation*. **16** (2009), pp. 31–42.

52. P. Levéen, J. Larsson, M. Ehinger, C. M. Cilio, M. Sundler, L. J. Sjöstrand, R. Holmdahl, S. Karlsson, Induced disruption of the transforming growth factor beta type II receptor gene in mice causes a lethal inflammatory disorder that is transplantable. *Blood*. **100**, 560–568 (2002).

53. L. Kenner, A. Hoebertz, F. T. Beil, N. Keon, F. Karreth, R. Eferl, H. Scheuch, A. Szremska, M. Amling, M. Schorpp-Kistner, P. Angel, E. F. Wagner, Mice lacking JunB are osteopenic due to cell-autonomous osteoblast and osteoclast defects. *J. Cell Biol.* **164**, 613–623 (2004).

54. A. L. Croxford, M. Lanzinger, F. J. Hartmann, B. Schreiner, F. Mair, P. Pelczar, B. E. Clausen, S. Jung, M. Greter, B. Becher, The Cytokine GM-CSF Drives the Inflammatory Signature of CCR2+ Monocytes and Licenses Autoimmunity. *Immunity*. **43**, 502–514 (2015).

55. J. R. Prigge, T. R. Hoyt, E. Dobrinen, M. R. Capecchi, E. E. Schmidt, N. Meissner, Type I IFNs Act upon Hematopoietic Progenitors To Protect and Maintain Hematopoiesis during *Pneumocystis* Lung Infection in Mice. *J. Immunol.* **195**, 5347–5357 (2015).

56. J. M. Leung, S. A. Budischak, H. Chung The, C. Hansen, R. Bowcutt, R. Neill, M. Shellman, P. Loke, A. L. Graham, Rapid environmental effects on gut nematode susceptibility in rewilded mice. *PLoS Biol.* **16**, 1–28 (2018).

57. S. Ariño, B. Aguilar-Bravo, M. Coll, W. Y. Lee, M. Peiseler, P. Cantallops-Vilà, L. Sererols-Viñas, R. A. Martínez-García de la Torre, C. Martínez-Sánchez, J. Pedragosa, L. Zanatto, J. Gratacós-Ginès, E. Pose, D. Blaya, X. Almodóvar, M. Fernández-Fernández, P. Ruiz-Blázquez, J. J. Lozano, S. Affo, A. M. Planas, P. Ginès, A. Moles, P. Kubes, P. Sancho-Bru, Ductular reaction-associated neutrophils promote biliary epithelium proliferation in chronic liver disease. *J. Hepatol.* **79**, 1025–1036 (2023).

58. F. Ruscitti, F. Ravanetti, J. Essers, Y. Ridwan, S. Belenkov, W. Vos, F. Ferreira, A. KleinJan, P. van Heijningen, C. Van Holsbeke, A. Cacchioli, G. Villetti, F. F. Stellari, Longitudinal assessment of bleomycin-induced lung fibrosis by Micro-CT correlates with histological evaluation in mice. *Multidiscip. Respir. Med.* **12**, 8 (2017).

59. B. Chassaing, J. D. Aitken, M. Malleshappa, M. Vijay-Kumar, Dextran Sulfate Sodium (DSS)-Induced Colitis in Mice. *Curr. Protoc. Immunol.* **104** (2014), doi:10.1002/0471142735.im1525s104.

60. J. Zhang, J. Muri, G. Fitzgerald, T. Gorski, R. Gianni-Barrera, E. Masschelein, G. D'Hulst, P. Gilardoni, G. Turiel, Z. Fan, T. Wang, M. Planque, P. Carmeliet, L. Pellerin, C. Wolfrum, S.-M. Fendt, A. Banfi, C. Stockmann, I. Soro-Arnáiz, M. Kopf, K. De Bock, Endothelial Lactate Controls Muscle Regeneration from Ischemia by Inducing M2-like Macrophage Polarization. *Cell Metab.* **31**, 1136-1153.e7 (2020).

61. J. J. Fuster, M. A. Zuriaga, V. Zorita, S. MacLauchlan, M. N. Polackal, V. Viana-Huete, A. Ferrer-Pérez, N. Matesanz, A. Herrero-Cervera, S. Sano, M. A. Cooper, H. González-Navarro, K. Walsh, TET2-Loss-of-Function-Driven Clonal Hematopoiesis Exacerbates Experimental Insulin Resistance in Aging and Obesity. *Cell Rep.* **33** (2020), doi:10.1016/j.celrep.2020.108326.

62. M. M. Bjørklund, A. K. Hollensen, M. K. Hagensen, F. Dagnæs-Hansen, C. Christoffersen, J. G. Mikkelsen, J. F. Bentzon, Induction of atherosclerosis in mice and hamsters without germline genetic engineering. *Circ. Res.* **114**, 1684–1689 (2014).

63. L. McInnes, J. Healy, J. Melville, UMAP: Uniform Manifold Approximation and Projection for Dimension Reduction (2018) (available at http://arxiv.org/abs/1802.03426).

64. S. Van Gassen, B. Callebaut, M. J. Van Helden, B. N. Lambrecht, P. Demeester, T. Dhaene, Y. Saeys, FlowSOM: Using self-organizing maps for visualization and interpretation of cytometry data. *Cytom. Part A*. **87**, 636–645 (2015).

65. M. Martin, Cutadapt removes adapter sequences from high-throughput sequencing reads. *EMBnet.journal*. **17**, 10 (2011).

66. B. Li, C. N. Dewey, RSEM: accurate transcript quantification from RNA-Seq data with or without a reference genome. *BMC Bioinformatics*. **12**, 323 (2011).

67. M. E. Ritchie, B. Phipson, D. Wu, Y. Hu, C. W. Law, W. Shi, G. K. Smyth, limma powers differential expression analyses for RNA-sequencing and microarray studies. *Nucleic Acids Res.* **43**, e47–e47 (2015).

68. M. D. Robinson, D. J. McCarthy, G. K. Smyth, <tt>edgeR</tt> : a Bioconductor package for differential expression analysis of digital gene expression data. *Bioinformatics*. **26**, 139–140 (2010).

69. M. I. Love, W. Huber, S. Anders, Moderated estimation of fold change and dispersion for RNA-seq data with DESeq2. *Genome Biol.* **15**, 550 (2014).

70. A. Dobin, C. A. Davis, F. Schlesinger, J. Drenkow, C. Zaleski, S. Jha, P. Batut, M. Chaisson, T. R. Gingeras, STAR: ultrafast universal RNA-seq aligner. *Bioinformatics*. **29**, 15–21 (2013).

71. Y. Hao, S. Hao, E. Andersen-Nissen, W. M. Mauck, S. Zheng, A. Butler, M. J. Lee, A. J. Wilk, C. Darby, M. Zager, P. Hoffman, M. Stoeckius, E. Papalexi, E. P. Mimitou, J. Jain, A. Srivastava, T. Stuart, L. M. Fleming, B. Yeung, A. J. Rogers, J. M. McElrath, C. A. Blish, R. Gottardo, P. Smibert, R. Satija, Integrated analysis of multimodal single-cell data. *Cell*. **184**, 3573-3587.e29 (2021).

72. M. Guo, M. P. Morley, C. Jiang, Y. Wu, G. Li, Y. Du, S. Zhao, A. Wagner, A. C. Cakar, M. Kouril, K. Jin, N. Gaddis, J. A. Kitzmiller, K. Stewart, M. C. Basil, S. M. Lin, Y. Ying, A. Babu, K. A. Wikenheiser-Brokamp, K. S. Mun, A. P. Naren, G. Clair, J. N. Adkins, G. S. Pryhuber, R. S. Misra, B. J. Aronow, T. L. Tickle, N. Salomonis, X. Sun, E. E. Morrisey, J. A. Whitsett, S. Lin, Y. Xu, Guided construction of single cell reference for human and mouse lung. *Nat. Commun.* **14**, 4566 (2023).

73. L. Waltman, N. J. van Eck, A smart local moving algorithm for large-scale modularity-based community detection. *Eur. Phys. J. B.* **86**, 471 (2013).

74. G. La Manno, R. Soldatov, A. Zeisel, E. Braun, H. Hochgerner, V. Petukhov, K. Lidschreiber, M. E. Kastriti, P. Lönnerberg, A. Furlan, J. Fan, L. E. Borm, Z. Liu, D. van Bruggen, J. Guo, X. He, R. Barker, E. Sundström, G. Castelo-Branco, P. Cramer, I. Adameyko, S. Linnarsson, P. V. Kharchenko, RNA velocity of single cells. *Nature*. **560**, 494–498 (2018).

75. P. Danecek, J. K. Bonfield, J. Liddle, J. Marshall, V. Ohan, M. O. Pollard, A. Whitwham, T. Keane, S. A. McCarthy, R. M. Davies, H. Li, Twelve years of SAMtools and BCFtools. *Gigascience*. **10** (2021), doi:10.1093/gigascience/giab008.

76. M. Köhler, A. Schindler, S. Sperlich, A Review and Comparison of Bandwidth Selection Methods for Kernel Regression. *Int. Stat. Rev.* **82**, 243–274 (2014).

77. T. Stuart, A. Srivastava, S. Madad, C. A. Lareau, R. Satija, Single-cell chromatin state analysis with Signac. *Nat. Methods*. **18**, 1333–1341 (2021).

78. D. Aran, A. P. Looney, L. Liu, E. Wu, V. Fong, A. Hsu, S. Chak, R. P. Naikawadi, P. J. Wolters, A. R. Abate, A. J. Butte, M. Bhattacharya, Reference-based analysis of lung single-cell sequencing reveals a transitional profibrotic macrophage. *Nat. Immunol.* **20**, 163–172 (2019).

79. T. S. P. Heng, M. W. Painter, K. Elpek, V. Lukacs-Kornek, N. Mauermann, S. J. Turley, D. Koller, F. S. Kim, A. J. Wagers, N. Asinovski, S. Davis, M. Fassett, M. Feuerer, D. H. D. Gray, S. Haxhinasto, J. A. Hill, G. Hyatt, C. Laplace, K. Leatherbee, D. Mathis, C. Benoist, R. Jianu, D. H. Laidlaw, J. A. Best, J. Knell, A. W. Goldrath, J. Jarjoura, J. C. Sun, Y. Zhu, L. L. Lanier, A. Ergun, Z. Li, J. J. Collins, S. A. Shinton, R. R. Hardy, R. Friedline, K. Sylvia, J. Kang, The Immunological Genome Project: networks of gene expression in immune cells. *Nat. Immunol.* **9**, 1091–1094 (2008).

80. M. Lawrence, W. Huber, H. Pagès, P. Aboyoun, M. Carlson, R. Gentleman, M. T. Morgan, V. J. Carey, Software for Computing and Annotating Genomic Ranges. *PLoS Comput. Biol.* **9**, e1003118 (2013).

81. Y. Zhang, T. Liu, C. A. Meyer, J. Eeckhoute, D. S. Johnson, B. E. Bernstein, C. Nusbaum, R. M. Myers, M. Brown, W. Li, X. S. Liu, Model-based Analysis of ChIP-Seq (MACS). *Genome Biol.* **9**, R137 (2008).

82. A. N. Schep, B. Wu, J. D. Buenrostro, W. J. Greenleaf, chromVAR: inferring transcription-factor-associated accessibility from single-cell epigenomic data. *Nat. Methods*. **14**, 975–978 (2017).

83. V. A. Traag, L. Waltman, N. J. van Eck, From Louvain to Leiden: guaranteeing well-connected communities. *Sci. Rep.* **9**, 5233 (2019).

84. M. Elosua-Bayes, P. Nieto, E. Mereu, I. Gut, H. Heyn, SPOTlight: seeded NMF regression to deconvolute spatial transcriptomics spots with single-cell transcriptomes. *Nucleic Acids Res.* **49**, e50–e50 (2021).

85. P. Badia-i-Mompel, J. Vélez Santiago, J. Braunger, C. Geiss, D. Dimitrov, S. Müller-Dott, P. Taus, A. Dugourd, C. H. Holland, R. O. Ramirez Flores, J. Saez-Rodriguez, decoupleR: ensemble of computational methods to infer biological activities from omics data. *Bioinforma. Adv.* **2** (2022), doi:10.1093/bioadv/vbac016.

86. C. Hafemeister, R. Satija, Normalization and variance stabilization of single-cell RNA-seq data using regularized negative binomial regression. *Genome Biol.* **20**, 1–15 (2019).

87. Y. Schlesinger, O. Yosefov-Levi, D. Kolodkin-Gal, R. Z. Granit, L. Peters, R. Kalifa, L. Xia, A. Nasereddin, I. Shiff, O. Amran, Y. Nevo, S. Elgavish, K. Atlan, G. Zamir, O. Parnas, Single-cell transcriptomes of pancreatic preinvasive lesions and cancer reveal acinar metaplastic cells' heterogeneity. *Nat. Commun.* **11** (2020), doi:10.1038/s41467-020-18207-z.

88. N. Caronni, F. La Terza, F. M. Vittoria, G. Barbiera, L. Mezzanzanica, V. Cuzzola, S. Barresi, M. Pellegatta, P. Canevazzi, G. Dunsmore, C. Leonardi, E. Montaldo, E. Lusito, E. Dugnani, A. Citro, M. S. F. Ng, M. Schiavo Lena, D. Drago, A. Andolfo, S. Brugiapaglia, A. Scagliotti, A. Mortellaro, V. Corbo, Z. Liu, A. Mondino, P. Dellabona, L. Piemonti, C. Taveggia, C. Doglioni, P. Cappello, F. Novelli, M. Iannacone, L. G. Ng, F. Ginhoux, S. Crippa, M. Falconi, C. Bonini, L. Naldini, M. Genua, R. Ostuni, IL-1β+ macrophages fuel pathogenic inflammation in pancreatic cancer. *Nature*. **623**, 415–422 (2023).

89. Y. Chu, E. Dai, Y. Li, G. Han, G. Pei, D. R. Ingram, K. Thakkar, J. J. Qin, M. Dang, X. Le, C. Hu, Q. Deng, A. Sinjab, P. Gupta, R. Wang, D. Hao, F. Peng, X. Yan, Y. Liu, S. Song, S. Zhang, J. V. Heymach, A. Reuben, Y. Y. Elamin, M. P. Pizzi, Y. Lu, R. Lazcano, J. Hu, M. Li, M. Curran, A. Futreal, A. Maitra, A. A. Jazaeri, J. A. Ajani, C. Swanton, X. D. Cheng, H. A. Abbas, M. Gillison, K. Bhat, A. J. Lazar, M. Green, K. Litchfield, H. Kadara, C. Yee, L. Wang, Pan-cancer T cell atlas links a cellular stress response state to immunotherapy resistance. *Nat. Med.* **29**, 1550–1562 (2023).

90. J. M. Amrute, X. Luo, V. Penna, S. Yang, T. Yamawaki, S. Hayat, A. Bredemeyer, I.-H. Jung, F. F. Kadyrov, G. S. Heo, R. Venkatesan, S. Y. Shi, A. Parvathaneni, A. L. Koenig, C. Kuppe, C. Baker, H. Luehmann, C. Jones, B. Kopecky, X. Zeng, T. Bleckwehl, P. Ma, P. Lee, Y. Terada, A. Fu, M. Furtado, D. Kreisel, A. Kovacs, N. O. Stitziel, S. Jackson, C.-M. Li, Y. Liu, N. A. Rosenthal, R. Kramann, B. Ason, K. J. Lavine, Targeting immune-fibroblast cell communication in heart failure. *Nature* (2024), doi:10.1038/s41586-024-08008-5.

91. K. Polański, R. Bartolomé-Casado, I. Sarropoulos, C. Xu, N. England, F. L. Jahnsen, S. A. Teichmann, N. Yayon, Bin2cell reconstructs cells from high resolution visium HD data. *Bioinformatics* (2024), doi:10.1093/bioinformatics/btae546.

92. R. A. Amezquita, A. T. L. Lun, E. Becht, V. J. Carey, L. N. Carpp, L. Geistlinger, F. Marini, K. Rue-Albrecht, D. Risso, C. Soneson, L. Waldron, H. Pagès, M. L. Smith, W. Huber, M. Morgan, R. Gottardo, S. C. Hicks, Orchestrating single-cell analysis with Bioconductor. *Nat. Methods*. **17**, 137–145 (2020).

93. D. J. McCarthy, K. R. Campbell, A. T. L. Lun, Q. F. Wills, Scater: Pre-processing, quality control, normalization and visualization of single-cell RNA-seq data in R. *Bioinformatics*. **33**, 1179–1186 (2017).

94. K. J. Travaglini, A. N. Nabhan, L. Penland, R. Sinha, A. Gillich, R. V. Sit, S. Chang, S. D. Conley, Y. Mori, J. Seita, G. J. Berry, J. B. Shrager, R. J. Metzger, C. S. Kuo, N. Neff, I. L. Weissman, S. R. Quake, M. A. Krasnow, A molecular cell atlas of the human lung from single-cell RNA sequencing. *Nature*. **587**, 619–625 (2020).

95. R. R. Wilcox, *Introduction to Robust Estimation and Hypothesis* (Academic Press, 5th edn., 2022).

96. W. L. Dunn, J. K. Shultis, *Exploring Monte Carlo methods* (Elsevier, Amsterdam, Second., 2022; 978-0-12-819739-4).

Acknowledgements

We thank all members of our laboratories for insightful feedback. E. Menet, Z. Zhao, E. Prieto, N.A Muñoz, R. Nieto and M. Vitón for help with sorting and cytometric analyses; L. Cabezuela and E. Santos for animal husbandry; V. Labrador, E. Arza, and the Microscopy Unit of the CNIC for help with microscopy; Laura Carramolino and Jacob Bentzon for providing plasmids encoding PCSK9; Jiaqui Li ad Henry Beach from Arizona State University for help with data visualization. Noah Palm for generous gift of mice. The Thoracic Oncology Clinical Database and Biobank (TOCDB) at the McGill University Health Centre for access to tissue and clinical data.

Funding

D.C-W. was supported by the Cancer Research Institute/Irvington Postdoctoral Fellowship (CRI CRI3511) and A.G.C by a predoctoral grant from MCIN (PREP2022-000391). I.B. was supported by grants from MICIN (RYC2020-029563-I and PID2022-140534NB-I00) and the BBVA Foundation (Leonardo fellowship; LEO22-2-2596). A.H. was supported by the Worldwide Cancer Research foundation (Grant 23-0115) and 1RO1AI165661 from NIH. D.G.A. is supported by contract 2023-CDT-11616 from a project with grant number TED2021-132296B-C55 funded by the Spanish MCIN/AEI/10.13039/501100011033. G.F.C. is supported by grants PID2022-142341OB-I00 funded by the Spanish MCIN/AEI/10.13039/501100011033 and European Union “NextGenerationEU/PRTR”, and SBPLY/23/180225/000041 funded by Junta de Comunidades de Castilla-La Mancha, Spain, and European Regional Development Fund. L.G.N is supported by National Natural Science Fund of China 32270956, 92374205. O.S. receives support from the Deutsche Forschungsgemeinschaft (CRC TRR332 A2 & Z1, CRC1009 A13, CRC1123 A6, 502158695), the Leducq Foundation, and IZKF and the IMF of the Medical Faculty Münster. L.A.W acknowledges funding from the Bachynski Family Foundation and D.F.Q. receives support from Canada Foundation for Innovation (CFI#42884). The CNIC is supported by the MCIN, the Instituto de Salud Carlos III, and the Pro-CNIC Foundation and is a Severo Ochoa Center of Excellence (grant number CEX2020-001041-S funded by MCIN/AEI/10.13039/501100011033).

Author contributions:

Conceptualization: I.B., A.H.
Data Curation: DC-W, AR-P, MR, EP, IK, GM, DGA, DJ-C, CT, DMG, IB
Formal analysis: DC-W, AR-P, MR, EP, IK, DGA, DJ-C, DMG, GF-C, IB
Funding acquisition: AM, MAM, KDB, AD, HH, GFC, FS-C, OS, DFQ, LAW, LGN, AH, IB
Investigation: DC-W, AR-P, MR, IK, ACG-B, NBB, SD, SC, AA-C, MZ, DM, SM-S, ACG-C, TD, AM, JZ, MIC, AG-C, PB, SR, MSFN, DCvO, SC, AED, FC, IB
Methodology: DC-W, EP, GM, GFC, AH, IB
Project administration and supervision: A.H.
Resources: AM, MAM, KDB, ALG, WCG, JDS, HH, GFC, FSC, JS, IU, JJF, JB, OS, DFQ, LAW, LNG, AH, IB
Software: AR-P, EP, GM, DGA, DJ-C
Validation: DC-W, AR-P, ACG-C, P-OF, IB
Visualization: DC-W, AR-P, AH, AH, IB
Writing: AH, IB

Competing interest:

Juan C. Nieto is scientific advisor of Omniscope

The authors declare no other conflicts of interest.

Data and materials availability: All the transcriptomics data are available in Gene Expression Omnibus (GEO) as a Super-series GSE266680. The individual GEO accession numbers are as follows Bulk (GSE266678), dogma-sequencing (GSE266930), single-cell (GSE266680), spatial transcriptomics (GSE266518). Visualization and analysis of the NeuMAP is available at the single-cell Data Analysis and VISualization scDAVIS (scDAVIS) web-based tool: https://bioinfo.cnic.es/scdavisr/ (Credentials for reviewers: user: neumap; pass: 0gl4d1h).

Supplementary Materials

Materials and Methods

Extended data Figures 1 to 11

References 52 to 96

Data S1 to S6

Figures and Figure Legends

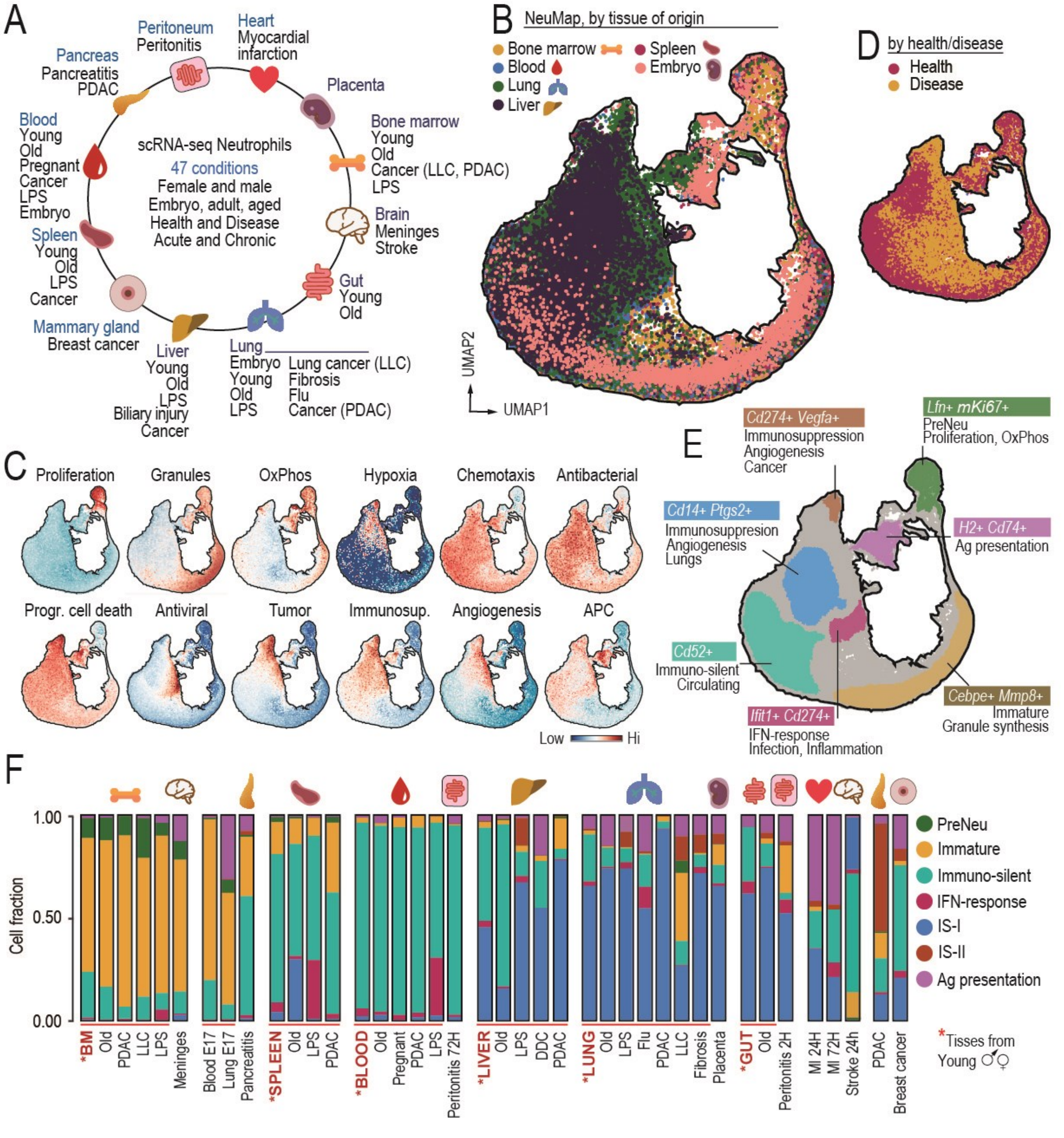

Figure 1. NeuMap, an integrative map of the neutrophil transcriptome. (A) Scheme of the tissues and biological conditions used to generate the NeuMap by scRNA-sequencing. See Table S1. **(B)** UMAP visualization by tissue of origin. **(C)** Score value of gene sets for specific biological processes. See Table S2 for the complete gene lists. **(D)** UMAP visualization of neutrophils extracted from health or diseased conditions. (**E**) Scheme of the functional compartmentalization of NeuMap. Each hub is defined by areas containing the top 85% K-mass score. **(F)** Stacked bars showing the proportion of cells form different organs and conditions in each functional hub.

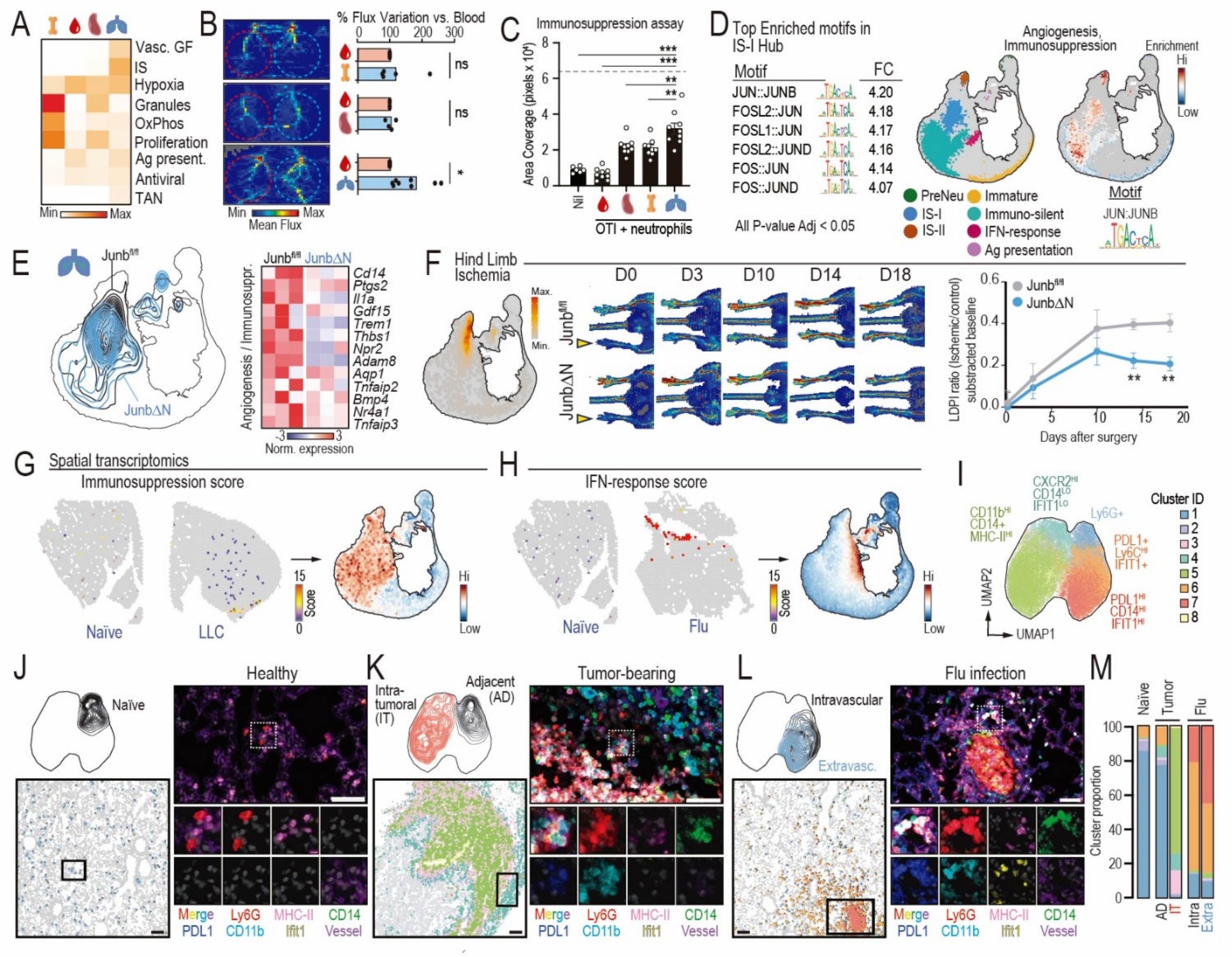

Figure 2. The NeuMap illuminates molecular and functional properties of lung neutrophils. (A) Heatmap of the proportion of cells in BM, spleen, blood, and lung neutrophils that contribute to the top 5% expressing cells for each indicated functional gene signature. VascGF., vascular growth factors; IS, Immunosuppression; OxPhos, oxidative phosphorylation; Ag. Pres., Antigen presentation; TAN, Tumor-associated neutrophils. The number of cells per tissue was downsampled to 1000 prior to the calculation of the contribution proportion. **(B)** *In vivo* matrigel plugs assay to assess the angiogenesis potential of neutrophils from the indicated tissues. Left, representative Doppler imaging of reference blood neutrophils control (red), and the respective tissue neutrophils (blue), which are quantified in the bar graph (right). Data from 4-8 mice per group. *, p<0.05 determined by two-tailed t test. **(C)** Quantification of OT-I T cell killing of B16OVA target cells in the presence of neutrophils from the indicated tissues. Data shows area coverage of live cells after culture of OT-I cells with neutrophils from the different tissues. No OT-I cell control is shown with a dashed line, and Nil shows untreated OT-I. Data from 6-9 independent experiments. **, p < 0.01; ***, p<0.001 determined by one-way ANOVA. **(D)** Dogma-seq analyses of neutrophils from the indicated tissues, mapped onto the NeuMap. Left, top TF motifs enriched in the IS-I hub. Right, mapping of the enrichment score for JunB binding sites. See Table S4 for motif enrichment analysis **(E)** Left, contour plot of lung neutrophils from control Junb$^{fl/fl}$ and JunbΔN mice mapped onto the NeuMAP. Right, heatmap showing relevant differentially expressed genes (DEG) of lung neutrophils obtained from bulk-sequencing analysis. See Table S5 for a list of the DEGs (**F**) K-Mass projection of neutrophils from ischemic hind limbs, and kinetics of revascularization of the ischemic limbs in control and JunbΔN mice, as assessed by Doppler analysis and quantified in the plots at right. Data is from 7-9 mice per group. *, p<0.05 determined by two-way ANOVA. **(G)** Spatial scRNA-sequencing. Mapping of the Immunosuppression signature score for neutrophils detected in the spatial map, in lungs from naïve and tumor-bearing (LLC) mice. Right, NeuMap showing the mapped enrichment score of the annotated neutrophils identified in the tumoral area. **(H)** Visualization of the IFN-response signature score for neutrophils detected in the spatial map of lungs from naïve and flu-infected mice. Right, NeuMap showing the enrichment score of the annotated neutrophils identified in flu-infected lungs. **(I)** Multiparametric tissue immunostaining. UMAP representation and unbiased clustering of the neutrophils from the lungs of tumor-bearing, flu-infected, and healthy mice. Key protein markers identifying each cluster are highlighted. **(J-L)** UMAP

of the annotated Ly6G+ neutrophils, showing cluster distribution and representative image of the stained tissue showing relevant markers defining the clusters in **(I)**, from lungs of naïve **(J),** tumor-bearing **(**LLC; **K),** and flu-infected mice **(L). (M)** Distribution of neutrophils per cluster in the different experimental conditions.

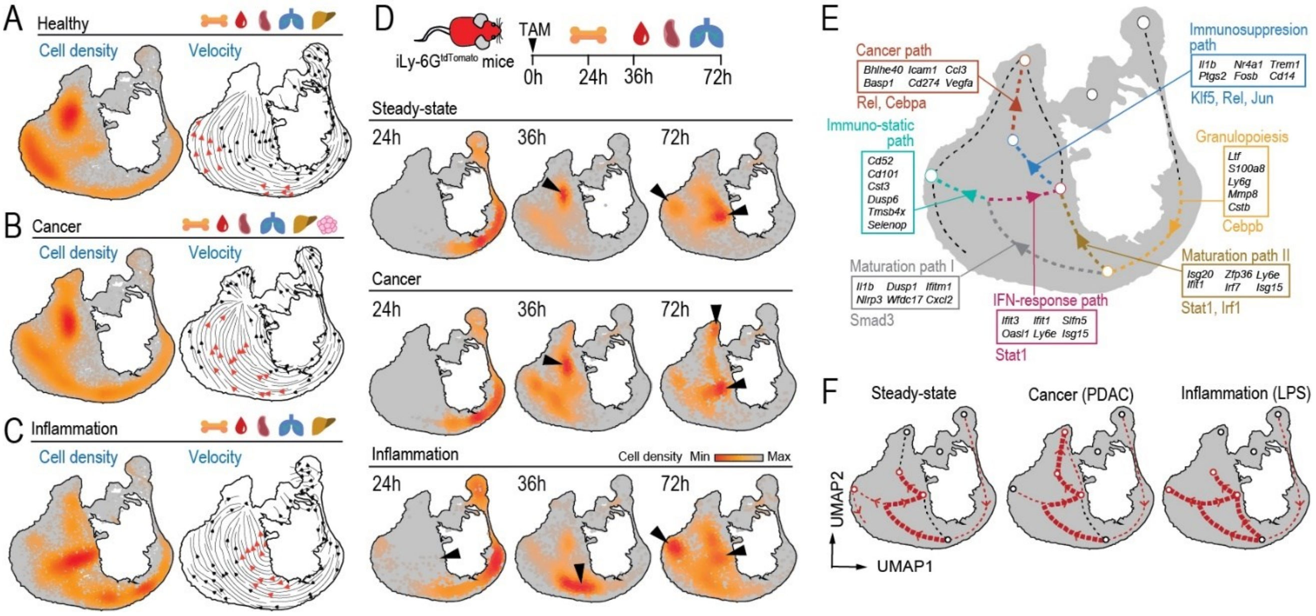

Figure 3. Transcriptional trajectories within the NeuMap. **(A-C)** K-mass score (representing cell density) of neutrophils from the BM, blood, spleen, lungs, and livers of naïve **(A)**, tumor-bearing (PDAC tumors) **(B)**, and LPS **(C)** treated mice projected on the NeuMap**.** RNA velocity analyses were performed for each of the conditions and the main developmental trajectories are highlighted in red arrows. **(D)** K-mass score of the mapped time-stamped neutrophils from steady-state, inflammation (LPS), and tumor-bearing mice (LLC) onto the NeuMAP. Neutrophils were tracked at 24h (BM, black dots), 36h and 72h (blood, spleen, and lung, orange-red scale) after tamoxifen-induced labelling of Ly6G-tdTomato cells. **(E)** Network model highlighting the trajectories identified in **(A-D)**, showing genes and transcription factors enriched for each trajectory. Transcription factors were selected when identified by both EnrichR and chromatin accessibility analyses. Note that we did not find any transcription factor enriched in the Immuno-static path. For a complete list see Table S6. **(F)** Inference of preferred trajectories for neutrophils from healthy, tumor-bearing, and inflamed mice from the data in **(A-D)**.

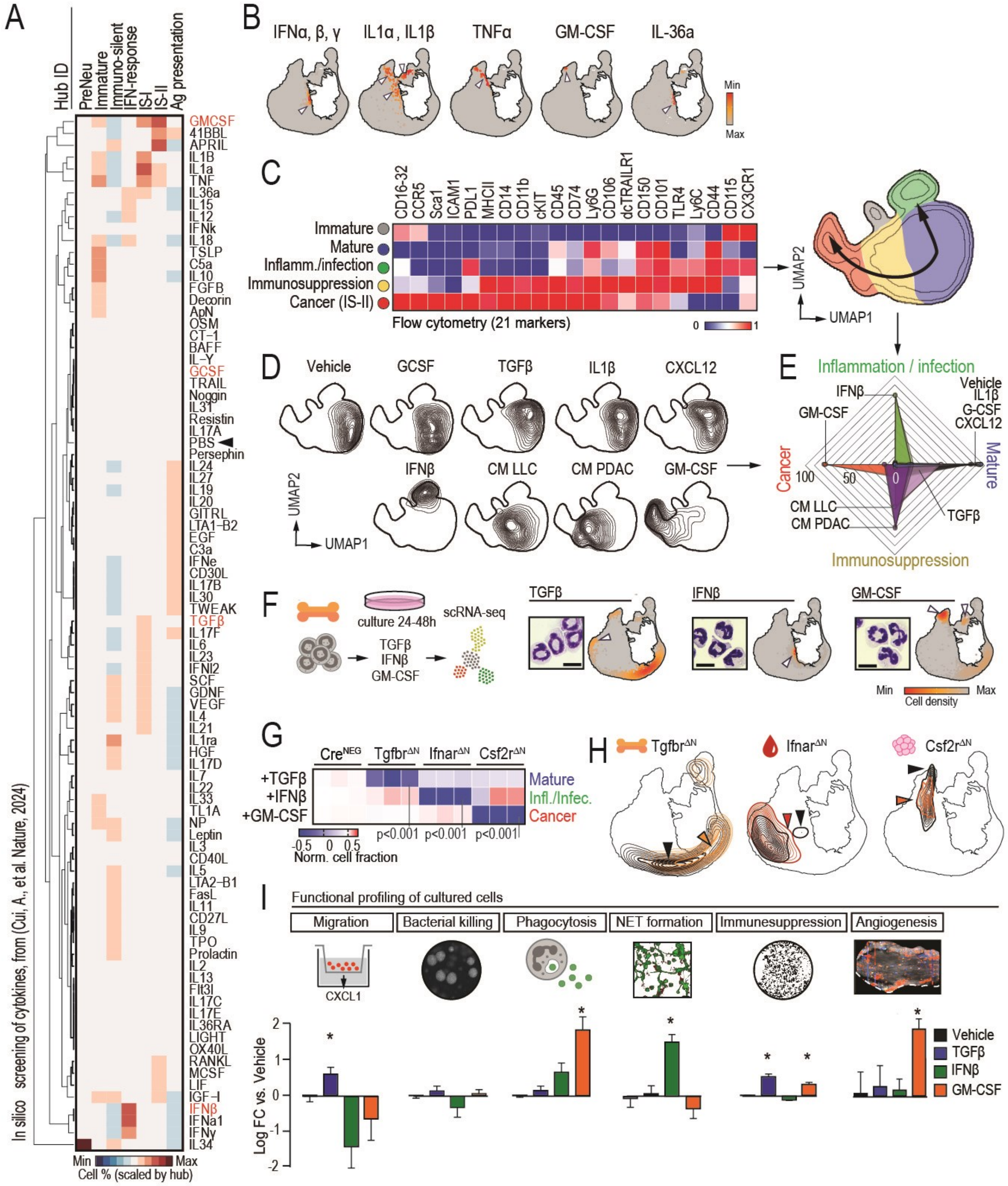

Figure 4. Signals that drive neutrophil maturation along the different paths. (**A**) *In silico* screening of cytokines that induce specific transcriptional profiles. The heatmap shows data from lymph node-derived neutrophils upon *in vivo* treatment with the indicated cytokines and PBS (arrowhead) as treatment control (*27*). Cells from this dataset were classified into the functional hubs of the NeuMap using the LabelTransfer function on the Seurat R package. The proportion of cells from each treatment classified into each functional hub is color-coded with values scaled by column (hubs) (**B**) Distribution of neutrophil transcriptomes from mice treated with the indicated cytokines onto the NeuMAP. (**C**) Heatmap showing the expression of the indicated 21 markers in BM-derived neutrophils (left), and UMAP projection (right) showing the profile of 5 functional states (immature, mature, inflammation/infection, immunosuppression (IS)-I, and IS-II). Data is from 4 independent experiments. (**D**) Contour plot showing the phenotypic distribution of neutrophils in the UMAP from (C) after treatment with the indicated cytokines and conditioned media for 24h. CM LLC, conditioned medium of LLC cells, CM PDAC,

conditioned medium of FC1242 cells. (**E**) Radar chart summarizing the data from (D), showing the distribution of neutrophils in phenotypic clusters in response to the indicated treatments. (**F**) Experimental scheme, hematoxylin/eosin staining, and the associated UMAP plots with K-mass projections on the NeuMAP of single-cell transcriptomes of BM neutrophils cultured with TGFβ, IFNβ, or GM-CSF. The micrographs show the distinct nuclear morphologies of the treated neutrophils, ranging from more immature (ringed) in the TGFβ group to more differentiated (multilobulated) in the other groups. (**G**) Heatmap visualization of the proportion of BM neutrophils from TgfbrΔN, IfnarΔN and Csf2rΔN mutants and Cre^{NEG} controls in the "Mature", "Inflammation/infection" and "Cancer" phenotypic clusters, after treatment with the indicated cytokines for 24h, determined by flow cytometry as in (C). Shown are Log2 fold values normalized to control vehicle, for three replicates per group. Statistical comparison by One-way ANOVA. (**H**) Contour plot showing the distribution in the NeuMAP of single cell transcriptomes of neutrophils from TgfbrΔN, IfnarΔN and Csf2rΔN mutants and Cre^{NEG} control mice from the indicated tissues, which shifts highlighted by arrowheads. These changes in distribution are quantified in Extended Data Fig.7F. (**I**) Analysis of the core functional properties of neutrophils treated with vehicle or the indicated cytokines. Data is from 3-7 independent experiments. *, $p<0.05$ as determined by One Way ANOVA.

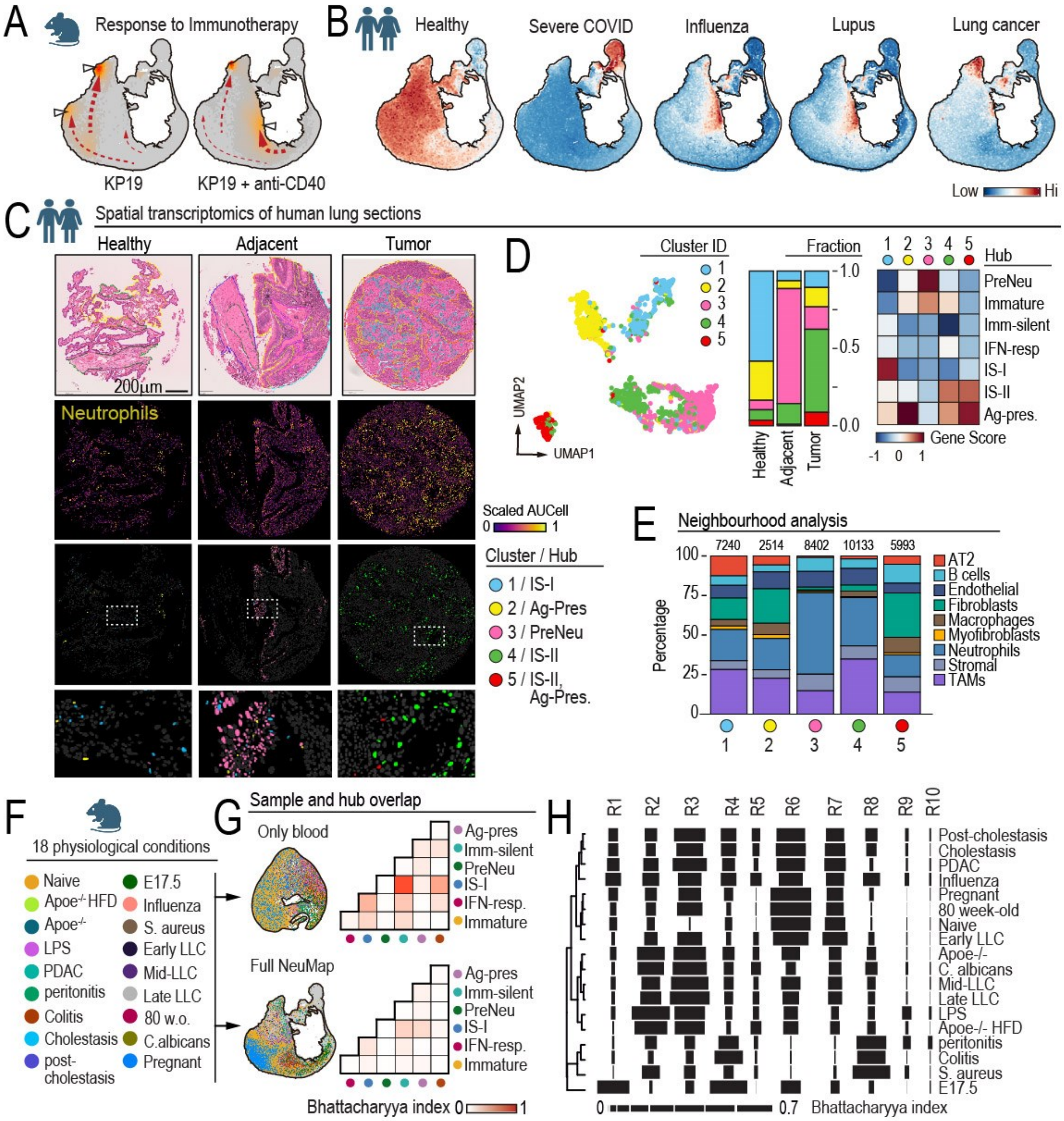

Figure 5. Predictive potential of the NeuMAP. (**A**) K-mass score of neutrophils from murine lung cancer, treated or not with anti-CD40 immunotherapy, from (*31*), and mapped onto the NeuMAP. **(B)** Signature scores from human neutrophils extracted from the blood of healthy individuals, with severe COVID-19 (*36*), influenza A (*32*), systemic lupus (*33*), or from lungs of cancer patients (*11*). **(C)** Representative images from spatial transcriptomics of lung sections from patients with lung adenocarcinoma, showing healthy tissue, adjacent tissue, and tumor lesion from the same individual. Top, H&E-stained sections; middle, spatial distribution of neutrophil gene signature scores; bottom, enlarged images of the selected regions showing the spatial distribution of neutrophils from the different clusters/hubs. **(D)** UMAP embedding of neutrophil transcriptomes from the spatial-seq dataset across all regions, identifying the transcriptional clusters shown in (**C**). The bar plot shows the relative abundance of each neutrophil state in healthy, adjacent, and tumor areas. Right: Heatmap showing the mean score per hub for each human cluster gene set. Scaled by signature (column). P<0.001 for all hubs, Kruskal-Wallis analysis. (**E**) Percent of closest neighbouring cells to neutrophils from the different clusters/hubs. Numbers indicate the number of cells scored for each group. TAM, tumor-associated macrophage. (**F**) Overview of the 18 physiological and pathological conditions from which single-cell blood neutrophil transcriptomes were obtained. (**G**) Top, UMAP of blood neutrophils from (F) coloured by sample origin. We used the Bhattacharyya index to measure the overlap

of the different blood samples, and the neutrophil hubs defined in Figure 1. Bottom, the same blood neutrophil transcriptomes were projected onto the reference NeuMAP embedding, and their overlap with transcriptional hubs is quantified in the correlation matrix as above. (**H**) Bhattacharyya indexes showing the overlap of each sample with the different NeuMap regions shown in Extended Data Fig.10C. The data are represented as a barcode for each condition in a hierarchical tree.

Supplementary Materials for

Architecture of the neutrophil compartment in mice

Cerezo-Wallis, Rubio-Ponce et al.

Corresponding authors: ivballes@salud.uc3m.es, andres.hidalgo@yale.edu

The PDF file includes:

Materials and Methods

Extended data Figures 1 to 10

References 54-93

Other Supplementary Materials for this manuscript include the following:

Table S1 to S6

Materials and Methods

Mice

All experiments were performed on 6–24-week-old C57BL/6 male and female mice. Young mice were defined as 8–12 weeks old, and old mice were defined as 22–24 months old at the time of analysis. Chow and water were available ad libitum. Mice with neutrophil-specific deficiency in *Tgfbr2* (TGFbRΔN) were generated by crossing MRP8^{CRE} mice with Tgfbr2$^{fl/fl}$ mice (*52*). Similarly, we generated neutrophil-specific mutants by crossing *Junb*-floxed (*53*), *Csf2r*-floxed (*54*) and *Ifnar1*-floxed mice (*55*) with the MRP8^{CRE} driver. *Apoe*$^{-/-}$ mice (B6.129P2-Apoetm1Unc; Taconic M&B). Ly6G^{CREERT2}Ly6G^{CREERT2} mice were crossed with Rosa26^{Tdtomato} Rosa26^{Tdtomato} mice as in (*16*), resulting in the iLy6G^{tdTom}iLy6G^{tdTom} mice used in our fate mapping experiments. Gavage administration of tamoxifen (2mg/ per mouse) was performed to induce CRE recombinase activity in 6-12 week-old male iLy6G^{tdTom}iLy6G^{tdTom} mice. JAXBoy (Ptprc^{K302E}) from Jackson laboratories and *Tet2*$^{-/-}$ mice (*20*) were used for adoptive bone marrow cell transfer. 8-week-old male Germ-free mice (C57Bl/6) were kindly provided by Noah Palm's Lab (Yale University). In brief, Germ-free C57BL/6 mice were bred and maintained under sterile conditions in flexible film isolators (Class Biologically Clean) in the Palm laboratory Gnotobiotic Facility at Yale School of Medicine. Mice were housed in a temperature- and humidity-controlled room under a dark–light cycle of 12 h–12 h. All animal protocols were approved by the Yale University Institutional Animal Care and Use Committee (protocol #11513).

For the rewilding experiments, littermate of mice were generated from multiple breeding pairs and randomly assigned to either remain in the institutional vivarium (laboratory mice) or released into the outdoor enclosures (rewilded mice) to control for the microbiota at the onset of the experiment. Outdoor enclosures were previously described (*56*) and the protocols for releasing the laboratory mice into the outdoor enclosure facility were approved by Rutgers University (protocol # PROTO999900794). All protocols were approved by the corresponding local authorities of Madrid, Singapore, Rutgers and Yale University.

Mouse models of disease

Stroke: Thrombotic occlusion of the middle cerebral artery (MCA) was induced by the ferric chloride (FeCl3) stroke model. Briefly, mice were anesthetized and maintained at 2% sevoflurane in a mixture of 0.2/0.8 L/min O2/air and temperature was kept at 36.5–37°C using a heating blanket. The scalp was opened, and the MCA was visualized with a stereomicroscope (PZMIV, World Precision Instruments, USA). A piece of Whatman filter paper strip soaked in freshly prepared FeCl3 (20%) was placed over the intact duramater on the artery for 10 minutes and then removed to allow the formation of a thrombus. Following surgery, individual animals were returned to their cages with free access to water and food. Brains were collected 24h after surgery to perform transcriptomics analysis.

Liver Cholestasis (biliary injury model). Mice were fed a 0.1% of 3,5-diethoxycarbonyl-1,4-dihydrocollidine (DDC)-supplemented diet for 3 weeks before sample collection, housed with a 12-hour light/dark cycle, and permitted ad libitum consumption of water as described (*57*). An additional group of animals was fed a 0.1% DDC-supplemented diet for 3 weeks and afterward allowed to recover for 3 days under standard mouse diet to study the reversibility of the cholestatic phenotype.

Influenza A infection**.** A stock of the virus strain A/PR8/34 (H1N1) was diluted, and 100 PFU were administered intra-nasally to isoflurane-anesthetized 8–12-week-old male mice in 50 µl of PBS. Mouse weight was monitored daily after infection and mice that presented weight loss < 20% of their initial body weight were sacrificed and considered deceased. For transcriptomic studies, blood and lungs were collected on day 4 after infection.

Pancreatitis. Acute pancreatitis was induced by intraperitoneal injections of 50 µg/kg of cerulein (Sigma-Aldrich), every hour, for a total of 7 administrations. Mice were sacrificed 24 hours after the first injection.

Orthotopic pancreatic tumor model. Mice were anesthetized with ketamine/xylazine, and had their abdomen shaved and swabbed with antiseptic. A 5mm vertical incision was made in the skin and abdominal layer at a point 1cm down from the xiphoid process of the sternum, and 1cm to the right of the midline. The pancreas was exposed, 10^5 FC1242 cells were resuspended in phosphate-buffered saline (PBS) and mixed with Matrigel (BD) in a 1:1 ratio and were injected as a volume of 50 µL into the body of the pancreas to form a visible bolus using a 30–gauge insulin needle. The pancreas was then returned to the abdominal cavity. The abdominal layer was closed with absorbable 5/0 sutures, while the skin was closed with non-absorbable 5/0 sutures. Superglue was applied over the sutures to ensure that they did not come undone after surgery. Mice were resuscitated with saline and were subcutaneously administered Buprenorphine (10mg/kg) and Enrofloxacin (Baytril, 1.5mg/kg) for the 2 days following surgery. Mice were euthanized at week 5 following surgery and tissues were collected for transcriptomic analysis.

Orthotopic breast tumor model. Mice were implanted orthotopically with $5x10^5$ E0771 breast cancer cells in 50 µl of matrigel into the thoracic mammary gland of C57BL6/J mice. Additionally, the same procedure was followed using the BALB/c derived 4 T1 breast tumor cell cancer in BALB/c mice. Mice were euthanized at week 4 after implantation and tumors were collected for transcriptomic analysis.

Orthotopic lung cancer model. $2x10^5$ Lewis Lung Carcinoma (LLC) cells in 100 µL PBS were administered intravenously into the lateral tail vein of 8-week-old C57BL6/J mice. Mice were euthanized at week 1,2 or 3 after the implantation and bloods and lungs were used for transcriptomics analysis.

Subcutaneous lung cancer model. Mouse LLC1 implants were generated in 8-week-old C57BL/6 mice by subcutaneous implantation of 0.5×10^6 cells (one injection site per mouse). Tumor growth was followed every 2 d by measuring the two orthogonal external diameters using a caliper. Tumor volume was calculated as $V = \pi/6 \times L \times W \times H$, where L, W, and H represent length, width, and height, respectively. Tumors were excised and processed for flow cytometry analysis when they reached $0.5\,cm^3$.

Cecal Ligation and Puncture (CLP)-Induced Sepsis. CLP was performed as previously described (*50*). Briefly, the peritoneal cavity of ketamine/xylazine-anesthetised mice was exposed with a small incision and the cecum was exteriorized. 80% of the cecum distal to the ileo-cecal valve was ligated using non-absorbable 7-0 suture. A 23-gauge needle was then used to puncture both walls of the distal end of the cecum, and a small drop of feces was extruded through the perforation. The ligated and punctured cecum was relocated inside the peritoneal cavity and both peritoneum and skin were closed. Blood was extracted 3 days after the puncture.

Peritonitis. Male 8- to 12-week-old mice were injected intraperitoneally with zymosan (1mg, intraperitoneal injection, Sigma). After 2 h and 72h we performed a peritoneal lavage for transcriptomic studies.

Myocardial Infarction. Male 8- to 12-week-old mice were intubated, and temperature controlled throughout the experiment at 36.5C to prevent hypothermic cardioprotection. Thoracotomy was then performed, and the LAD was ligated with a nylon 8/0 monofilament suture for 45 min. At the end of the ischemia, the chest was closed, and animals were kept with 100% O_2 and given analgesia with buprenorphine (subcutaneous injection, 0.1 mg/kg) as described previously (*50*). Mice were sacrificed 24h or 72h hours after surgery and the heart was isolated for transcriptomics studies.

Bleomycin-induced fibrosis. We administered 1 mg/Kg of bleomycin sulfate to 8- to 12-week-old mice as previously described (*58*). Briefly, bleomycin was dissolved in saline and was instilled into the tracheal lumen through a cannula under isoflurane (2.5% in oxygen) anesthesia. Bleomycin was injected at day 0 and at day 4. Mice were sacrificed three weeks after bleomycin injection and lungs were collected for transcriptomics analysis.

S. Aureus Infection. Mice were intravenously infected with 2.5×10^7 CFU of Staphylococcus aureus (RNU4220 strain) and monitored for weight loss. For single cell transcriptomic studies, blood was collected 5 days after infection.

Candida Infection. Mice were intravenously infected with 1.5×10^5 *C. albicans* conidia (SC5314 strain), blood for single cell transcriptomic studies was extracted at day 6 post-infection (*50*).

LPS-induced inflammation. for transcriptomic studies, 400ng of LPS (Sigma) were injected intravenously. Blood and tissues were collected 24h after injection. An intraperitoneal lethal dose of LPS (40mg/kg) was used as a model of endotoxic shock. Mice were monitored daily for weight loss. A weight loss of more than 20% of initial body weight was considered a lethal event and mice were sacrificed at human endpoints.

High Fat diet. *Apoe*$^{-/-}$ mice were fed for 6 weeks with a control or high-fat diet (HFD, 10.7% total fat, 0.75% cholesterol; Sniff, Soest, Germany) before blood extraction**.**

DSS Colitis. To induce colitis, mice received for 9 days water with 1.5% Dextran Sulphate Sodium (DSS) salt, (MP Biomedicals) as previously described (*59*). Blood was collected on day 9 after DSS.

Hind Limb ischemia. Hind-limb ischemia experiments were performed as described (*60*). Briefly, mice were anesthetized with isoflurane, the hind limb was shaved, and, following a small incision in the skin, both the proximal end of the femoral artery and the distal portion of the saphenous artery were ligated. The artery and all side-branches were dissected free; after this, the femoral artery and attached side-branches were excised. Immediately after surgery, perfusion was measured by Laser Doppler Imaging of plantar regions of interest (Moor Instruments Ltd, Axminster, Devon, England) and calculated as ratio of left (ligated) versus right (unligated) values. Ischemic muscle samples for transcriptomics analysis were collected 1 day after surgery.

Model of Clonal Hematopoiesis and PCSK9-Induced Hypercholesterolemia. To model TET2 loss-of-function-driven clonal hematopoiesis, we performed an adoptive bone marrow transfer (ADT) without pre-conditioning. Ten-week-old unirradiated JAXBoy (Ptprc^{K302E}) recipient mice were intravenously injected with a total of 1.5×10^7 unfractionated CD45.2$^+$ *Tet2*$^{-/-}$ bone marrow (BM) cells, administered as three consecutive daily doses of 5×10^6 cells (*61*). Donor cells were harvested from age-matched littermate *Tet2*$^{-/-}$ mice (8–10 weeks old) by flushing femurs and tibias following euthanasia. To induce hypercholesterolemia, a recombinant AAV vector encoding a gain-of-function form of murine PCSK9 (pAAV/D377Y-mPCSK9) was delivered via a single tail vein injection (*62*). One week later, mice were placed on either a high-cholesterol Western diet (Envigo, TD.88137; 42% calories from fat, 0.2% cholesterol) or a matched control diet for 13 weeks. At endpoint, ADT mice were euthanized and Tet2$^{-/-}$ (CD45.2$^+$) or WT (CD45.1$^+$) neutrophils were isolated from peripheral blood and bone marrow by cell sorting. Cells were processed for single-cell RNA sequencing as described below.

Sample preparation and flow cytometry-assisted cell sorting

Mice were euthanized and Blood was taken through cardiac puncture with 1ml syringe attached to a 26 g needle filled with 50mL of 0.5M EDTA. After blood collection, animals were perfused via the right ventricle with 10 mL of PBS to remove circulating blood cells. Tissues including lung, tumors, muscle, heart, placenta and pancreas were harvested, cut into small pieces, and digested with Liberase TM (Sigma) and DNase I (Sigma) for 30 minutes at 37°C. Following digestion, tissues were passed through 70 µm nylon mesh sieves using syringe plungers to obtain single-cell suspensions.

Bone marrow cells were obtained by flushing femurs with PBS containing 2 mM EDTA and 2% fetal bovine serum (FBS) using a 23-gauge needle. Spleens were mechanically dissociated through 70 µm mesh filters. For colon isolation, intestines were cleaned, cut longitudinally, and washed in PBS. After a 30-minute incubation in 100 mM EDTA at 37°C with shaking to remove epithelial cells, colon tissue was cut and digested in Liberase TM and DNase I for 30 minutes at 37°C. Ear (skin) samples were processed by separating the dorsal and ventral sides, cutting them into small pieces, and digesting them in Liberase TM and DNase I for 90 minutes at 37°C. The resulting suspensions were filtered as above. Peritoneal lavage was performed by injecting 10 mL of cold PBS into the peritoneal cavity, followed by gentle massage of the abdomen and careful aspiration of the fluid using a syringe and needle. The collected fluid was centrifuged, and the pellet was resuspended in FACS buffer for staining.

For meninges isolation, mice were euthanized and decapitated. The skull was opened along the sagittal midline, and the brain was removed to expose the dura. The meninges were peeled off using fine forceps and placed directly into digestion solution on ice. For the brain, infarcted regions were dissected and digested for 30 minutes at 37°C in an enzyme cocktail containing: 50 U/mL collagenase; 8.5 U/mL dispase; 100 µg/mL Nα-tosyl-L-lysine chloromethyl ketone hydrochloride; 5 U/mL DNase I in 9.64 mL HBSS without calcium, magnesium, or phenol red (Fisher Scientific, 14175-095). After digestion, brains were ground using a 2 mL glass-glass grinder, filtered through a 70 µm filter, and centrifuged. Cell pellets were resuspended in 7 mL of 35% Percoll, overlaid with 5 mL HBSS to form a gradient, and centrifuged at 800 × g for 30 minutes at 4°C (no brake). The myelin layer and supernatant were discarded, and the final cell pellet was washed and resuspended in FACS buffer.

All single-cell suspensions were lysed in RBC lysis buffer (eBioscience) for 4min and stained with the following antibodies: CD11b-PE (Clone M1/70, BioLegend, 1:200); Ly6G-AF647 (Clone 1A8, eBioscience, 1:200); DAPI (1:10,000). Neutrophils were sorted as live (DAPI-negative), CD11b$^+$ Ly6G$^+$ cells using a FACS Aria sorter (BD Biosciences) at the CNIC Cytometry Unit. Bone marrow neutrophils were capture as Lineage negative (B220, CD18, NK.1.1, Ter119, CD3).

Cancer cell culture

The C57BL6/J syngeneic mouse Lewis Lung Carcinoma (LLC), E0771 breast luminal B and the BALB/c-derived 4T1 breast tumor cell cancer cell lines were from the American Type Culture Collection. The pancreatic adenocarcinoma FC1242 cell line (kind gift from Dr. Dannielle Engle, Tuveson lab, Cold Spring Harbour Laboratory) was derived from Pdx1Cre; KrasG12D/+; null/+ (KPC) mice. All cells were cultured in Dulbecco's modified Eagle's medium (DMEM; Thermofisher) supplemented with 10% fetal bovine serum (FBS; Thermofisher) and 100 µg ml−1 Penicillin/Streptomycin (Thomas Sci).

In vitro mouse neutrophil culture and analysis

Primary mouse neutrophils were obtained from the femurs and tibias of healthy C57BL/6J mice, or indicated mouse genetically modified mouse model, by centrifugation. Erythrocytes were lysed using Red Blood Cell Lysis Solution (Qiagen; 79217). Cell strainer-filtered single-cell solutions were sorted in BD Aria Cell Sorter as DAPI^{NEG} CD45+ CD11b+ Ly6G+ CD101+ mature, and DAPI^{NEG} CD45+ CD11b+ Ly6G+ CD101^{NEG} immature neutrophils. Cells were seeded in 96-well plates, 50,000 cells per well, and cultured with complemented DMEM media (vehicle), or with the indicated treatments. GCSF (574606, BioLegend), TGFβ (7666-MB-005/CF, R&D), IFNβ (581302, BioLegend), CXCL12 (578704, BioLegend), IL1B (401-ML, R&D Systems), and GM-CSF (315-03-20UG, Thermofisher) were used at a concentration of 10 ng/ml. Conditioned medium of LLC or KP-PDAC cells was obtained after 24h culture of 80% confluence cells. Neutrophils were collected after 24h or 48hr of treatment, and stained with the following antibody panel: Sca1 BUV395 (D7, BD), I-A/I-E BUV496 (M5/114.15.2, BD), CD106 BUV563 (429, BD), CCR5 BUV615-P (C34-3448, BD), CD74 BUV661 (In-1, BD), CD115 BUV737 (AFS98, BD), CD274 BV421 (10F-9G2, BioLegend), CD11b BV510 (M1/70, BioLegend), CD44 BV570 (IM7, BioLegend), cKit BV605 (ACK2, BioLegend), DC-trail-R1 biotinylated (Polyclonal, R&D Systems), Ly-6C BV711 (HK1.4, BioLegend), TLR4 BV786 (MTS510, BD), Cx3Cr1 FITC (SA011F11, BioLegend), CD16/32 PerCP-Cy5.5 (93, BioLegend), ICAM1 PE-Dazzle 594 (YN1/1.7.4, BioLegend), CD150 PE-CY5 (TC15-12F12.2, BioLegend), CD101 PE-Cy7 (MOUSHI 101, eBioscience), Ly6G PE(1A8, BioLegend), CD45 APC (30F11, BioLegend), and CD14 APC-CY7 (Sa14-2, BioLegend). Secondary staining was performed with Streptavidin BV650 (Biolegend). Cells were analysed in a SymphonyA4 Flow Cytometer. The data was analyzed using FlowJo software. FlowAI (DOI: 10.1093/bioinformatics/btw191) was used for QC of flow data, followed by dimensionality reduction using UMAP_R plugin (*63*). Initial Clusterization was performed with FlowSOM (*64*) and ClusterExplorerPlugin, and UMAP parameters were embedded in each sample for statistical analysis of neutrophils phenotypes.

RNA Isolation, Reverse Transcription, and RT-PCR

Total RNA was prepared with the RNA Extraction RNeasy Plus Mini-kit (QIAGEN) and RNA was reverse-transcribed with the High-Capacity cDNA Reverse Transcription kit (Applied Biosystems; Carlsbad, CA) according to the manufacturer's protocol. Real-time quantitative PCR (SYBR-green, Applied Biosystems) assays were performed with an Applied Biosystems 7900HT Fast Real-Time PCR System sequencer detector. Expression was normalized to the expression of the *36b4* housekeeping gene. Primer sequences are as follow:

36b4: F 5′-ACTGGTCTAGGACCCGAGAAG-, R 5′- TCCCACCTTGTCTCCAGTCT-;
Ptgs2: F 5′ -TGAGCAACTATTCCAAACCAGC-, R 5′- GCACGTAGTCTTCGATCACTATC-
Nr4a1: F 5′- TTGAGTTCGGCAAGCCTACC-, R 5′- GTGTACCCGTCCATGAAGGTG-
Il1b: F 5′-AGTGAGGAGAATGACCTGTTC-, R 5′-CGAGATGCTGCTGTGAGATT-
Tnfaip3: F 5′-GAACAGCGATCAGGCCAGG-, R 5′-GGACAGTTGGGTGTCTCACATT-
Cebpe: F 5 -'GCAGCCACTTGAGTTCT CAGG-, R 5′-GATGTAGGCGGAGAGGTCGAT-
Ltf: F 5′-TGAGGCCCTTGGACTCTGT-, R 5′-ACCCACTTTTCTCATCTCGTTC-

Functional assays

T cell cytotoxicity assay

B16F10–OVA-GFP (10^4 cells) were seeded in 96-well culture dishes for 24 h, in RMPI medium + glutamine (Thermofisher) containing 10% heat-inactivated FBS (Thermofisher), 100 µg ml−1 Penicillin/Streptomycin (Thomas Sci); 200 nM glutamine, 1% non-essential amino acids (MEM amino acids; Gibco), 1% sodium pyruvate (Gibco) and 0.01% β-mercaptoethanol (Gibco). Neutrophils from sorting or *in vitro* cultures were co-culture at a 2:1 ratio with SIINFEKL-activated OT-1 T effector cells for 3 hours. Neutrophil-OTI cells were then seeded on top of B16F10–OVAGFP target cells 1:2 ratio. After 24 hours, live cells were stained with 0.4g/L crystal violet (Sigma-Aldrich, HT90132). The area covered by target cells was quantified from micrographs of the plates using the ImageJ software.

In vivo Matrigel plug assay

50,000 neutrophils sorted from tissues of interest were resuspended in 500µL of growth-factor depleted Matrigel (Corning) and injected subcutaneously in the lower back of anesthetized mice to form plugs. At days 3 and 7 post-implantation, the same number of sorted neutrophils was resuspended in 50µL of PBS and injected directly into the plug respectively. On day 9 post-implantation, Doppler laser perfusion imaging was performed at the lower back region that contained the Matrigel plugs. One region of interest (ROI) was defined for each observable Matrigel plug, and the amount of flux variation in each ROI was quantified. Only ROIs that were not obscured by hair regrowth were used.

Chemotaxis assay

Chemotaxis assays were performed as described in (*50*). Briefly, BM neutrophils were plated in 6.5mm polycarbonate transwells with 5mm pores (Corning, Corning, USA) in RPMI medium 48h after cytokine treatment. 20ng/ml CXCL1 (R&D) was added to the bottom well. Transwells were incubated for 2h at 37C and transmigrated cells were harvested from the bottom well and stained for cytometric analysis. The number of transmigrated cells was assessed by the presence of a known number of Truecount beads (BD Biosciences)

3D doppler imaging of tumor vascularization

Subcutaneous LLC tumor vascularization was imaged using Vevo® Imaging Systems once they reached $500mm^3$. In brief, mice were anesthetized in an isoflurane-vaporizer chamber, and the backs were thoroughly shaved. The mice were placed in the imaging platform and images were captured using the Power color doppler-3D mode. A total of 100 images were captured to generate a 3D reconstruction of the vasculature. Vevo LAB software was used to calculate the Volume and percent vascularization (PV) of tumors. PV value is determined by calculating the percentage of pixels in the volume that have a Power Doppler signal associated with them, the presence of this signal indicates the presence of blood flow.

NET formation assay

48h after cytokine treatment, 5×10^4 BM neutrophils were plated with RPMI medium on poly-l-lysine-covered 8-well µ-Slides (Ibidi), and left 30min to adhere. Subsequently, cells were incubated for 2h with 100nM PMA or vehicle. Cells were then fixed using 4% PFA for 10min, permeabilized with PBS with 0.1% Triton X-100, 1% goat serum plus 5% BSA and stained with antibodies against cit-H3, DNA (Sytox-green, Molecular Probes) and MPO. Whole-slide Z stack tilescan images were acquired with a Leica SP5 confocal microscope, and analyzed using the Imaris software (*50*).

Bacterial killing assay

48h after cytokine treatment, BM neutrophils were resuspended in fresh media along with live *S. aureus* (ATCC) that were grown in tryptic soy broth. For the *in vitro* assays, neutrophils and bacteria (10^4 CFU in 200ul) were incubated at 37°C for 60 min. The cells are then plated onto tryptic soy plates in a serial dilution. Bacterial colonies on the plates were counted the following day.

Phagocytosis assay

48h after cytokine treatment, BM neutrophils were resuspended in fresh media along with fluorescent latex beads (SIGMA) followed by flow cytometric analyses.

Analysis of human neutrophils

Isolation and Expansion of Human Bone Marrow CD34$^+$ HSPCs

Bone marrow samples were obtained from healthy donors under informed consent approved by the ethics committee of the University Hospital Tübingen. CD34$^+$ HSPCs were isolated through Ficoll gradient centrifugation followed by magnetic bead-based separation using the EasySep™ Human CD34$^+$ Cell Selection Kit II (Stem Cell Technologies, #17856). CD34$^+$ cells (n=4; purity 95.4 ± 1.9%) were cultured at a density of 5 × 10^5 cells/ml in StemSpan™ SFEM II hematopoietic stem cell medium (Stem Cell Technologies, #09655), supplemented with 1% penicillin/streptomycin (P/S), 20 ng/ml IL-3, 20 ng/ml IL-6, 20 ng/ml TPO, 50 ng/ml SCF, and 50 ng/ml FLT-3L (all cytokines purchased from R&D Systems). Cells were cultured under standard conditions (37°C, 5% CO_2) and frozen for future use.

For granulocytic differentiation *in vitro*, cells were seeded at a density of 2 × 10^5 cells/ml. During the first 8 days of differentiation (days 0–7), cells were maintained in a myeloid cell expansion medium - RPMI 1640 supplemented with 10% FCS, 1% penicillin/streptomycin (P/S), 5 ng/ml SCF, 5 ng/ml IL-3, and 1 ng/ml G-CSF. The medium was changed every two days. On day 8 of culture, the medium was replaced with a granulocytic cell differentiation medium (RPMI 1640 supplemented with 10% FCS, 1% P/S, and 1 ng/ml G-CSF). The medium was changed every two days until day 14. On day 13 of differentiation, cells were collected and counted. 800,000 cells were lysed for RNA isolation, 50,000 cells for FACS, and 40,000 cells for cytospins. The remaining cells were resuspended in fresh granulocytic differentiation medium at a seed density of 2 × 10^5 cells/ml and divided into four groups. Group one was maintained in granulocytic differentiation medium, group two was treated with 10 ng/ml TGF-β, group three with 10 ng/ml IFNβ (refreshed after 24h), and group 4 with 10 ng/ml GM-CSF. RNA-seq analyses were performed 48 hours after stimulation.

HoxB8 Cell Cultures and Differentiation

HoxB8-immortalized myeloid progenitors were routinely tested for mycoplasma contamination and cultured in RPMI 1640 medium supplemented with 10% fetal calf serum (FCS), 30 µM β-mercaptoethanol (Thermo Fisher Scientific), 1% supernatant from SCF-producing CHO cells, and 1 µM β-estradiol (Sigma-Aldrich) to maintain the progenitor state. Neutrophil differentiation was initiated by β-estradiol withdrawal and continued culture in medium supplemented with 1% SCF-containing supernatant. Differentiation into neutrophils was achieved by culturing cells in RPMI 1640 medium containing 10% FCS, 30 µM β-mercaptoethanol, 4% SCF supernatant, and 20 ng ml^{-1} granulocyte colony-stimulating factor (G-CSF) under standard tissue culture conditions (37 °C, 5% CO_2).

CRISPR–Cas9-Mediated Knockout. To generate gene knockouts, HoxB8 progenitors were transduced with lentiCas9-v2 lentiviral vectors encoding guide RNAs (gRNAs) targeting the following genes and exons: *Cebpb* (exon 1; gRNA: AGGCTCACGTAACCGTAGT); *Klf6* (exon 1; gRNA: TCGCTGTCGGGAAAACAGGG); *Runx1* (exon 3; gRNA: TAGCGAGATTCAACGACCTC); *Rfx2* (exon 5; gRNA: CTGCTGGGGGCGTAAAGCTG); *Relb* (exon 4; gRNA: CTGCACGGACGGCGTCTGCA); *Irf5* (exon 2; gRNA: ACCCTGGCGCCATGCCACGAGG); *Junb* (exon 1; gRNA: GGAACCGCAGACCGTACCGG). Gene editing was performed as previously described (22).

JunB Overexpression. Lentiviral vectors for Junb overexpression were generated by transient transfection of HEK293T cells using the calcium phosphate precipitation method. Cells were co-transfected with (i) a transfer plasmid containing the Junb cDNA under the control of the human PGK promoter, (ii) packaging plasmid psPax2, and (iii) envelope plasmid pMD2.G encoding VSV-G. The media was replaced 24 h post-transfection. At 72 h, virus-containing supernatant was collected, clarified by centrifugation (2,000 rpm, 5 min, 4 °C), filtered (0.45 μm), and concentrated via ultracentrifugation (26,000 rpm, 2 h, 4 °C). Viral pellets were resuspended in cold PBS, aliquoted, and stored at −80 °C.

Lentiviral Transduction of HoxB8 Cells. HoxB8 progenitors were transduced by spinoculation. Briefly, 5×10^5 cells were plated per well in 6-well plates with 1 mL of medium. Lentiviral particles were added at a multiplicity of infection (MOI) of 11.24 for the vector pRRL-hPGK-JunB-IRES-eGFP and MOI = 1.8 for the pRRL-hPGKIRES-eGFP empty vector, and cells were centrifuged at 1,000 × g for 90 min at 30 °C. Following transduction, cells were harvested, washed, and resuspended in fresh differentiation medium at a final concentration of 5×10^4 cells per ml.

Plasmid Construction. To construct the Junb expression vector, the human PGK (hPGK) promoter was PCR-amplified with ClaI and XbaI restriction sites and cloned into the ClaI/XbaI sites of the pRRL-CMV-IRES-eGFP vector, replacing the CMV promoter. The Junb coding sequence was amplified from mouse cDNA using primers containing BglII and XhoI sites and inserted into the BamHI/XhoI sites of the modified vector. Cloning was performed using the following primers: hPGK Fw (ClaI): 5′-TTTTTTATCGATGGGTAGGGGAGGCGCTTT-3′; hPGK Rv (XbaI): 5′-TTTTTTTTAGACGAAAGGCCCGGAGATGA-3′; Junb Fw (BglII): 5′-TTTTTAGATCTGCCACCATGTGCACGAAAATGGAACA-3′; Junb Rv (XhoI): 5′-TTTTTTCTCGAGTCAGAAGGCGTGTCCCTT-3

Culture of HoxB8 cells. For the flow cytometry and bulk RNA sequencing experiments, HoxB8 progenitors at day 3.5 of differentiation were seeded in 96-well plates at a density of 50,000 cells per well. Cells were cultured in complete DMEM medium (vehicle) or treated with GM-CSF (10ng/ml) for 48h, following the same conditions described for primary bone marrow neutrophil cultures. Vehicle or GM-CSF treated cells were collected at 48h after treatment for the analysis.

Bulk RNA-sequencing of mice and human-derived neutrophils

RNA from isolated mouse neutrophils was extracted using RNAeasy micro kit (Quiagen ®). RNA quality was checked using capillary electrophoresis (Agilent). Samples were submitted for whole RNA next generation sequencing in the Genomics Unit of CNIC. 200 ng of total RNA was used to generate barcoded RNA sequencing libraries using the NEBNext Ultra RNA Library preparation kit (New England Biolabs). Libraries were sequenced with HiSeq2500 (Illumina) to generate 50-nucleotide single reads, with a minimum of eight million reads per sample. For RNA-seq of human-derived neutrophils, we isolated RNA from a total of the differentiated neutrophils collected on day 13 and 15. We used the NucleoSpin RNA Mini Kit (Macherey-Nagel, cat. no. 740955.50), following the manufacturer's instructions. RNA concentration was assessed with Qubit 2.0 (Thermo Fisher), and a total of 400 ng RNA was sequenced. RNA integrity was assessed using Agilent Bioanalyzer 2100, with RNA integrity numbers (RIN) between 9.8 and 10.0. RNA samples were processed by Novogene (Munich, Germany) for library preparation and sequencing, and all samples passed the quality control criteria. Strand-specific libraries were generated based on Novogene´s standard protocol. Samples were sequenced on an Illumina platform to produce 150 bp pairwise reads (PE150) per sample.

FastQ files for each sample were obtained using CASAVA v1.8 software (Illumina). Reads were further processed with RTA v1.18.66.3. FastQ files for each sample were obtained using bcl2fastq v2.20.0.422 software (Illumina). Sequencing reads were further processed as follows: Illumina adapters were trimmed and low-quality reads removed with Cutadapt v4.9 (*65*) (mismatch rate = 1 mismatch every 10bp, overlap = 5bp, minimum read length = 30bp). Quality control of the processed reads was done with fastQC v0.12.1. RSEM v1.3.1 was used to quantify expression levels against the mouse genome reference GRCm38 or the human genome reference GRCh38, depending on the analysis (*66*) (default options). The processing of the counts and differential expression analysis was performed using limma v3.32.2 (*67*) and EdgeR v3.20.1 (*68*), which were also used to perform pairwise differential expression analyses. To identify genes whose expression significantly varies across conditions, we applied a Likelihood Ratio Test (LRT) using DESeq2 v1.30.1 (*69*), allowing the detection of global effects of a factor without the need to specify individual contrasts. The resulting significant genes were then clustered using the k-means algorithm from the stats package v4.0.3.

Single cell Transcriptomics

Single cell RNA sequencing (scRNA-sequencing) of sorted tissue neutrophils

For single cell analysis all sample were collected between ZT1 and ZT5. Tissues were dissected and dissociated into a single-cell suspension by enzyme digestion. The resulting suspensions were filtered through cell strainers, and sorted in BD Aria Cell Sorter as DAPI-CD11b+Ly6G+ cells and loaded into a BD Rhapsody cartridge. For the generation of single-cell whole-transcriptomes we used a BD Rhapsody system according to the manufacturer instructions. Briefly, cell suspensions from each condition were incubated with Sample Tags (BD) for 20 minutes at RT. Cells were then washed three times and pooled in a single tube. Cell viability and concentration were assessed using a Countess III cell counter (Thermo Fisher). 60,000 cells were loaded into a Rhapsody Single Cell Analysis System cartridge. Cell capture and cDNA synthesis were performed according to manufacturer's instructions; cells were isolated into nanowells by gravity, then cells lysed and mRNAs together with sample tags oligos were released and captured by beads present in the nanowells. Each bead contained a unique oligo named "cell label" to identify each individual bead. All beads present in the cartridge were collected and cDNA synthesis took place in a single reaction. At this point each cDNA and Sample Tag oligo were attached to its corresponding "cell label" oligo. Two separated indexed libraries were prepared for whole transcriptome analysis and Sample Tag demultiplexing following manufacturer's instructions. The average size of the libraries was calculated using the 2100 Bioanalyzer (Agilent) and the concentration was determined using the Qubit fluorometer (Thermofisher). Finally, libraries were combined and sequenced together in a paired-end run (60x42) using a NextSeq 2000 system (Illumina) and a P2 flow cell. Output files were processed with NextSeq 1000/2000 Control Software Suite v1.4.1. FastQ files for each sample were obtained using BCL Convert v3.6.3 software (Illumina).

Construction of the NeuMap and projection of external data

Once sequenced, the samples were aligned to BD's mm10 reference (http://bd-rhapsody-public.s3-website-us-east-1.amazonaws.com/; Rhapsody-WTA/mm10 directory) using STAR (*70*). Later, the Rhapsody analysis pipeline v1.9.1 was run locally. This pipeline includes steps for quantification and filtering of low-quality cells and tagging of doublets, which were also filtered out of the downstream analyses (*71*). After BD Rhapsody's pipeline automatic quality filtering, a second round was performed manually, where cells with a mitochondrial content over 20% or with over 300 total gene counts were discarded. Cell Annotation was performed using R package SingleR and the Immgen database for each dataset individually. All subsequent downstream analyses were implemented using R v4.0.3 and the package Seurat v4.0.5 61. The Seurat suite was used to integrate the neutrophils from all datasets using Seurat's integration implementation. This method uses common sources of variation across the different datasets and aligns the cells so those in similar biological states cluster together. The integrated dataset was used to perform the unbiased cluster analysis and the construction of the

NeuMap. Additionally, we used the integrated NeuMap to generate a reference which we later used to analyse additional and external datasets by projecting cells onto our reference and annotate the new data using our custom labels using Seurat's MapQuery and TransferData. This method is technology agnostic, so we could reliably project cells from external datasets sequenced in different platforms onto the NeuMap (*72*, *73*).

Definition of Hubs

Functional hubs were selected by performing unbiased clustering at different resolutions using Seurat's function FindClusters(). Resolutions used ranged between 0.05 and 0.3. Clusters from different resolutions were selected because they best represented the expression of functional signatures projected onto the NeuMap. Areas shown in the figures correspond to the q15 quantile of the KMASS algorithm, which calculates the density of cells in specific areas. For clarity, hubs in figures are shown as the area with the accumulation of 85% of cells for each selected cluster/hub. Analyses were performed on the complete set of cells for each cluster/hub. The FindAllMarkers() function from Seurat was used to calculate differentially expressed genes across the hubs. Only genes detected in a minimum of 25% of the cells and with an average of at least 0.25-fold difference (log-scale) between the groups in either of the groups were tested.

Kernel Density Estimation (K-mass score):

The R package v7.3.61 was used for two-dimensional kernel density estimation, with n=100 grid points in each direction.

Signature Projection

The signatures used for illustration of functional states are contained in Table S2. All signatures were calculated by Seurat's AddModuleScore() function. We used two different sources for the functional signatures, one were previous publications, for which we provide the whole list of genes reported and used in Suppl. Table 2; and the second were public databases such as GO and GSEA. In those cases the whole gene list from the functional category was tested. For signatures from human data, human genes were mapped to their corresponding mouse homologue to calculate the enrichment score using the Mouse Genome Informatics (MGI) database. We used R package v5.2.1 AddModuleScore() function to calculate the scores. To generate visualization heatmaps across NeuMap hubs, we first calculated enrichment scores for each cell. Scores were then averaged by hub and scaled per signature for comparison. To assess whether gene signature scores significantly differed across NeuMap hubs, we applied the Kruskal–Wallis test to each signature, testing the null hypothesis that score distributions were identical across hubs. The resulting test statistics were compared to a chi-squared distribution, with degrees of freedom equal to the number of hubs minus one. To correct for multiple comparisons, we adjusted p-values using the Benjamini–Hochberg False Discovery Rate (FDR) method.

Patient Survival Analysis

The TCGA datasets were downloaded using the TCGAbiolinks R package suite. Only samples from patients with primary and solid tumors were used. An "overall survival" variable was created for the test, which is equal to "days to death" for dead patients, and to "days to last follow up" for patients who are still alive. Patients were divided into two groups using the .75 and .25 percentile of expression of the gene signatures in each hub. The signatures for each hub were created using the significant genes (adj.p.value < 0.05) with an average log2FC higher than 1. Mouse genes were translated into their human homologue genes using the Mouse Genome Informatics (MGI) database to perform the test. Survival curves were compared using the log-rank test.

Velocyto analysis

The analysis of expression dynamics in single-cell RNA sequencing data was performed using velocyto (*74*), a package that allows estimating RNA velocities distinguishing between spliced and unspliced mRNAs in standard single-cell RNA sequencing protocols. The command line tool in Python implementation was adapted to be able to work with BAM files generated by BD Rhapsody, using samtools (*75*) to format the files, mainly by removing all possible alignments with antibodies and renaming the UMI barcode tag to "UB" instead of "MA". Velocyto was then executed with default parameters and the GRCm38 reference genome with the gencodevM19-20181206 transcriptome annotation. After concatenation of the spliced and unspliced data from all experiments, the results were merged with the outputs from single cell analyses performed with Seurat in R, and scVelo (*76*) was used for further processing. Preprocessing included gene selection by detection (the minimum number of both unspliced and spliced counts was set to 30), and by variability (keep 2000 highly variable genes), normalization, and log1p transformation. First and second order moments were computed among 50 nearest neighbors in the PCA space using 30 components. Cell-based RNA velocities were estimated by modelling the transcriptional dynamics of splicing kinetics using the stochastic model available in scVelo. Finally, these velocities were projected onto the previously computed UMAP and visualized at the cellular level or as velocity vector fields through streamlines.

In some experiments we performed Pseudotime analysis. Samples were pre-processed using the standard Monocle3 pipeline. To address batch effects, samples were integrated using the Batchelor algorithm. Dimensionality reduction and clustering were performed within Monocle3, and pseudotime values were computed for the integrated dataset. To evaluate the significance of differences in pseudotime values between Cre^{NEG} control and TgfbRII mutant immature cells, we applied a non-parametric Wilcoxon rank-sum test with continuity correction (W = 373,675; p-value = 0.005548).

Comparison of cell distribution in the different hubs

To test differences in how neutrophils distributed in the different hubs, we classified cell hubs for both mutant and control samples based on the k-nearest neighbors (KNN) algorithm (k = 5) of the cells projected onto the Neumap. The observed hub proportions were calculated for each sample, and differences were determined by subtracting proportions in control from proportions in mutant cells. To assess the statistical significance of these differences, we used a bootstrap approach. For this, we generated a null distribution of hub proportion differences by merging each control-mutant pairs into a mixed population. From this combined dataset, 10,000 resampled pairs were drawn with replacement, matching the sample sizes of the original control and mutant datasets. The differences in hub proportions between the resampled mutant and control groups were then calculated. The null distributions for each hub were verified to have a mean of 0.0, as expected under the null hypothesis. Finally, p-values for the observed differences were computed by determining the fraction of resampled differences that were as extreme as or more extreme than the observed differences. To estimate 95% confidence intervals, the quantiles corresponding to the 0.025 and 0.975 percentiles of the null distributions were calculated.

Single cell multiome: DOGMA-seq technology

To simultaneously profile chromatin accessibility and gene expression at single-cell resolution, we used the Chromium Next GEM Single Cell Multiome ATAC + Gene Expression platform (10x Genomics). We harvested neutrophils from BM, spleen and lung (Dataset 1) and Lewis Lung Carcinoma (LLC) and Spleen with LPS (Dataset 2) from 8-12 weeks C57BL/6 mice Healthy blood was sequenced in both datasets as a quality control reference. Single-cell suspensions were prepared as described above. After staining, cells were washed, resuspended in sorting buffer, and incubated with DAPI (NBP2311561, Novus Biologicals) for 15 minutes prior to sorting.

Live CD11b$^+$Ly6G$^+$ neutrophils were sorted in equal proportions from each organ. Cells were then pooled and lysed in 100 µL of cold DIG lysis buffer (20 mM Tris-HCl, 150 mM NaCl, 3 mM $MgCl_2$, 0.005% Digitonin, 2 U/µL RNase inhibitor) for 5 minutes on ice. Lysis was quenched with 1 mL of cold DIG wash buffer, followed by centrifugation at 500 × g for 5 minutes. Nuclei were resuspended in 100 µL of 10x Genomics Nuclei Buffer supplemented with 1 mM DTT (Sigma) and 2 U/µL RNase inhibitor (Roche) to a final concentration of 3,400 nuclei/µL. After additional washes and centrifugation, samples were processed for library preparation at the Yale Center for Genome Analysis (YCGA).

Library construction was performed following the 10x Genomics protocol (Chromium Next GEM Multiome ATAC + GEX v1.1, CG000338 Rev E). Briefly, nuclei underwent transposition using the ATAC transposition mix and were loaded onto the Chromium Controller for GEM generation, barcoding, and reverse transcription. Separate libraries were constructed for ATAC and gene expression using standard amplification and indexing steps. Libraries were quantified using Bioanalyzer (Agilent) and Qubit (ThermoFisher), pooled, and sequenced on an Illumina NovaSeq 6000 platform (paired-end, 150 bp) with a target depth of 75 million reads per sample.

Data processing

Initial QC and cell filtering. DNA accessibility and gene expression from each cell were analyzed simultaneously using Seurat (*71*) and Signac (*77*) R packages. Per-cell quality control metrics were evaluated using the DNA accessibility and transcriptional data was performed. Cells that did not pass the following criteria were removed from downstream analysis: number of counts in the ATAC data (nCount_ATAC) < 100000 and > 100; number of counts in the gene expression data (nCount_RNA) < 5000 and > 100; number of genes in the gene expression data (nFeature_RNA) < 2500 and > 100; ratio of mono-nucleosomal to nucleosome-free fragments (nucleosome_signal) < 2; ratio of fragments centered at the transcription starting site (TSS) to fragments in TSS-flanking regions > 1; percentage of mitochondrial gene expression < 5.

ATAC data annotation. R packages Signac v1.14.0 and Seurat v5.1.0 were used to analyze single cell chromatin data and gene expression, respectively. Full genome sequences for Mus musculus (Mouse) were used as provided by UCSC (mm10, based on GRCm38.p6), and annotated using Ensembl Mus musculus annotations v.79

Cell type identification and neutrophil subset classification. We used R package SingleR v2.8.0 (*78*) to annotate cell types against the ImmGen database (*79*). Cells annotated as “neutrophils” were subset and re-analyzed by running a new round of FindVariableFeatures() in which outlier features were identified and ScaleData() to re-scale the expression of the neutrophil subset.

Mapping onto the NeuMap. We used Seurat v5.1. FindTransferAnchors() function to identify pairwise correspondences (anchors) between the reference and query datasets using the transcriptomics data. This function employs canonical correlation analysis (CCA) and mutual nearest neighbors (MNN) to identify cells with similar gene expression profiles across the two datasets. The top 2000 variable features shared between the reference and query datasets were used for anchor identification.

The query dataset was mapped onto the NeuMap reference using the MapQuery() function. This step projected the query cells from the DOGMA-seq into the NeuMap embedding space, allowing for direct comparison and visualization of the dogma cells relative to the NeuMap. Hub annotations from the NeuMap were transferred to the query dataset using the TransferData() function. This function predicts cell labels for each query cell based on the similarity scores computed from the anchors. The predicted labels were assigned to the query dataset, enabling downstream analysis of chromatin state in cells from each hub. Additionally, we assessed the confidence scores provided by TransferData() for each predicted label, retaining only high-confidence predictions (predicted.id.score>=0.7) for downstream analysis.

Merging of the datasets and Peak calling: We created a common peak set, and quantified this peak set in each experiment using Signac v1.14.0 and GenomicRanges v1.58.0 (*80*) prior to merging the objects. Once both datasets contained an assay with the same set of features, we used Seurat v5.2.1 R package to merge the datasets.

We used the Signac R package v1.14.0 to call peaks with the CallPeaks() function. The CallPeaks() function used MACS2 v2.2.9.1 (*81*) to run. Peaks were called for cells assigned to each hub separately. Only cells with a predicted.id.score>=0.7 were retained for peak calling. Peaks on nonstandard chromosomes and in genomic blacklist regions were removed. After QC and predicted score filtering 1962 for dataset 1 and 8155 neutrophils remained for dataset 2.

ATAC data processing. R package Signac v1.14.0 standard processing pipeline was applied to the combined data: Term Frequency-Inverse Document Frequency (TF-IDF) normalization was applied via

RunTFIDF(), top features were identified using FindTopFeatures() with a minimum cutoff of 5 and Singular Value Decomposition (SVD) was performed on the normalized data running RunSVD().

Differential Peak Analysis. Differential accessibility peaks were identified using FindAllMarkers(), considering only positive markers and a minimum percentage of cells expressing the feature (min.pct = 0.1). The closest genes to the differentially accessible peaks were annotated using the ClosestFeature(). The results were merged and filtered to retain significant peaks and marked for uniqueness.

Motif Enrichment Analysis. A position frequency matrix (PFM) set was retrieved from the JASPAR2020 database via the homonim R package v0.99.10, filtering for vertebrate transcription factors in the CORE collection. Motif information was added to the dataset with the BSgenome.Mmusculus.UCSC.mm10 genome as reference. Enriched motifs in the differentially accessible peaks per hub were then identified.

Transcription Factor Activity. Chromatin accessibility variability analysis was performed using R package chromVAR v1.28.0 (*82*), with the BSgenome.Mmusculus.UCSC.mm10 genome as the reference. This step computes motif activity scores for each cell, representing the inferred transcription factor activity based on chromatin accessibility.

Spatial Transcriptomics (Visium OCT)

Visualization of gene expression within the tissue was conducted using 10x Visium Spatial Gene Expression Kit (10x Genomics; PN1000184) as per the manufacturer's protocol. The OCT blocks were cut using a cryostat (Leica; PN-CM1520) and first cuts were used for RNA extraction (Qiagen; PN-74034), and RNA quality was assessed using the Agilent RNA 6000 Pico chips (Agilent; PN- 5067-1513), ensuring a minimum RIN number of 7. Secondly, 10µm sections were cut on the Visium Spatial Tissue Optimization Slide (PN-1000193) to assess optimal tissue permeabilization time. Lastly, one 10µm section was mounted on a Visium Spatial Gene Expression Slide and then stained for H&E and imaged using the NanoZoomer S210 (Hamamatsu; NP-C13239) to assess tissue morphology and quality. Following protocol instructions, the sections were then permeabilized for 18 min where tissue was lysed, and reverse transcription was performed followed by second strand synthesis and cDNA denaturation. Spatially barcoded, full-length cDNAs were amplified by PCR for 16 and 17 cycles, depending on the initial concentration previously determined by qPCR. Indexed sequencing libraries were generated via End Repair, A-tailing, adaptor ligation, and sample index PCR. Size distribution and concentration of full-length GEX libraries were verified on an Agilent Bioanalyzer High Sensitivity chip (Agilent). Finally, sequencing of GEX libraries was carried out on a NovaSeq 6000 sequencer (Illumina) aiming at approximately 40,000 pair-end reads per spot.

Data pre-processing

For the analysis of the spatial transcriptomics data, SpaceRanger software (10x Genomics, v1.3.0) was employed to map the sequenced reads, correct amplification bias and obtain the count matrix. The mouse genome (mm10) was used as the reference. The filtered feature expression matrices generated were then used as input for downstream analysis with Seurat[6868] (v4.4.0) in R (v.4.3.1).

Quality control and data normalization

To ensure quality of the data, spots not overlapping tissue were removed previously to the SpaceRanger mapping with the Loupe Browser software (10X Genomics). Quality metrics were calculated on a per-slide basis to preserve biological variability. Differences in total UMI across spots were adjusted by log-normalization using the NormalizeData() function from Seurat. This function divides the raw gene counts for each cell by the total counts of that cell and multiplies it by the scale factor (10,000), which is then log-normalized as log(1+x). Genes not expressed in any spot overlapping tissue were also removed.

Feature selection, dimensionality reduction

To annotate the distinct lung regions of each Visium slide, we used the FindVariableFeatures() function to extract the top 3,000 highly variable genes and capture major axes of biological variability. Data was then scaled with ScaleData() to Z-score. Principal component analysis was performed, and the top 50 principal components were retained for subsequent analysis steps.

Clustering and annotation

To perform clustering, FindNeighbors() function was applied together with the Leiden (*83*) community detection algorithm. Sample-specific resolutions were chosen, ranging from 0.2 to 0.6 in the function FindClusters(). Lastly, differentially expressed genes for each cluster were identified with FindAllMarkers() function and Wilcoxon Rank Sum test. When needed, clusters showing high heterogeneity were sub clustered and markers re-calculated. Each region of the lungs was then annotated considering the differentially expressed genes together with the hematoxylin/eosin staining.

Downstream analysis

To estimate cell type composition for each spot, we deconvoluted the spatial transcriptomic data using the single-cell reference of the mouse lung from the LungMap project (*72*). This was achieved using the seeded NMF regression approach in SPOTlight (*84*) (v1.0.3). Spots with a predicted composition of neutrophils of 10% or more were annotated accordingly. Signature scoring was performed using decoupleR (*85*) (v2.8.0), employing the univariate linear model.

Analyses of PDAC and myocardial infarction (MI) models

Spatial transcriptomics data were analyzed for the PDAC and MI mouse datasets (*4*, *24*) using the Seurat package (v5.1.0) in R. Raw count matrices were first filtered to remove unexpressed genes. Low-quality spots were excluded based on thresholds for the number of detected genes, total UMI counts, and mitochondrial gene content. Spots with abnormally low or high total counts, low gene detection, or mitochondrial percentages exceeding dataset-specific thresholds were considered low quality and discarded. We normalized using SCTransform (*86*, *87*). Highly variable features were identified using the FindVariableFeatures() function, selecting the top 10% of genes by variability within each dataset. Data were then scaled using ScaleData() to center gene expression values and apply Z-score transformation. Dimensionality reduction was performed using principal component analysis (PCA) via RunPCA() on the selected highly variable genes. Neighborhood graphs were constructed with FindNeighbors() based on the first 20 PCs, followed by clustering with the Leiden algorithm and a resolution parameter set to 0.5 using FindClusters(). Low-quality clusters lacking underlying tissue structure were identified and removed. UMAP embeddings were computed on the same 20 PCs using RunUMAP() for visualization.

For single-cell referencing, we used a publicly available dataset (GSE141017and GSE176092) (*24*, *87*). Quality control was applied by removing unexpressed genes and low-quality cells based on gene counts, UMI counts, and mitochondrial gene content. The dataset was normalized using SCTransform, followed by identification of highly variable genes (top 10%), scaling, and PCA using 30 (MI) to 40 (PDAC) components. Batch correction across samples was performed using FindIntegrationAnchors() and IntegrateData(). Clustering was performed with the Leiden algorithm (resolution = 0.5) after computing neighbors using the top 30-40 PCs. UMAP was used for visualization. We annotated cell type identities using SingleR (v2.6.0) with reference profiles from the MouseRNAseq ImmGen databases via the celldex package (v1.14.0) and curated marker genes from the dataset's own clustering results. Marker genes for each cell type were extracted using FindAllMarkers(). Cell-type-specific markers were used in subsequent annotation and deconvolution steps. Cell-type deconvolution of spatial transcriptomics data was conducted using the SPOTlight package (v1.0.3), employing a seeded non-negative matrix factorization (NMF) regression approach. Spots with neutrophil compositions of 10% or higher were labeled accordingly.

For neutrophil hub signature scoring and subtype analysis, we identified the top 15 marker genes for each hub, and module scores were calculated using AddModuleScore(). Seeded K-means clustering (K = 7) was performed on neutrophil-labeled spots using the hub marker signatures. Clusters were annotated based on the most specific and abundant signature. Clusters with no dominant signature were left unclassified. This procedure was repeated for macrophage and T-cell subtype signatures described in (*88*, *89*). For MI-associated fibroblasts (from (*90*)), a different strategy was employed by classifying the cell subtypes in the reference single-cell dataset and predicting their respective abundances directly via deconvolution. Spatial annotations were derived by integrating information from the Leiden clusters, cell type deconvolution, histological inspection, and expression of cancer-specific signatures. GSEA and over-representation analyses were used to characterize and differentiate distinct tumor cores. Finally, to investigate spatial relationships between spots, we constructed a graph using the igraph::graph() function based on a distance matrix computed from spot coordinates (stats::dist()). The graph was tuned to include only immediate neighbors based on the 2D spatial grid structure.

Spatial analysis of human lung specimens using Visium HD

The protocols for human sample biobanking were approved by the McGill University Health Centre Institutional Review Board (IRB # 2014-1119). From these samples, tissue microarrays (TMAs) were constructed by a pathologist based on intratumoural neutrophil abundance, using one-millimeter cores sampled from formalin-fixed paraffin-embedded (FFPE) pulmonary invasive adenocarcinomas with high-grade predominant solid architecture and adjacent non-tumorous lung tissue. Samples were derived from eight patients. Sections (5 µm) were mounted onto Visium CytAssist HD slides (10x Genomics) and processed following the manufacturer's protocol. In brief, FFPE tissue sections underwent deparaffinization, decrosslinking, probe hybridization, ligation, and extension, followed by spatial barcoding and sample indexing. Final library quality and fragment size were assessed using an Agilent Bioanalyzer High Sensitivity chip. Libraries were sequenced at the McGill University Genome Centre on an Illumina NovaSeq X Plus platform (1.5B reads, PE100 per lane). Spatial gene expression data were processed using Space Ranger (10x Genomics), and high-resolution spatial transcriptomic profiles were generated for downstream analysis.

FASTQ files from the Visium HD experiment were mapped to the GRCh38-2020-A reference genome using the Visium_Human_Transcriptome_Probe_Set_v2.0_GRCh38-2020-A probe set with Space Ranger (v3.1.1, 10x Genomics). Sample areas were manually selected using Loupe Browser, and the registration file H1-RTF6MBB-A1-fiducials-image-registration.json was provided to spaceranger count via the --loupe-alignment argument. High-resolution H&E and CytAssist images were passed with the --image and --cytaimage arguments, respectively.

Cell-level transcriptomic profiles were reconstructed using the Bin2cell package (*91*) (v0.3.2). First, an AnnData object was created with b2c.read_visium, then filtered to retain bins with at least one count and genes expressed in at least three spots (min_counts = 1, min_cells = 3). The H&E image was scaled using b2c.scaled_he_image with mpp = 0.38. Due to variability in bin sizing across the array, 2 µm bins exhibit slight differences in width/height, leading to a striped appearance. To correct this artifact, the b2c.destripe function was applied. Nuclei segmentation was then performed on the H&E using b2c.stardist with parameters: stardist_model = "2D_versatile_he", prob_thresh = 0.1, and nms_thresh = 0.1. Segmented nuclei were expanded using b2c.expand_labels with algorithm = "volume_ratio". To recover additional cells not segmented via H&E, the Stardist fluorescence model was applied to a σ-smoothed gene expression image generated using b2c.grid_image (mpp = 0.38, sigma = 5). b2c.stardist was re-run with stardist_model = "2D_versatile_fluo" and the same thresholds. Cells not segmented with the H&E-based model were assigned secondary labels from the fluorescence model. Finally, bins were grouped into cells with the b2c.bin_to_cell function. To reconstruct the Segmentation Polygon Mask we converted the .npz mask output from Bin2cell into a data frame using pd.DataFrame.from_dict (pandas v2.2.3). This file was then processed in R (v4.4.1) using the concaveman package (v1.1.0) to generate cell polygons for visualization.

SingleCellExperiment (*92*) objects were created in R by importing the Bin2cell .h5ad files with the h5ad2sce function from the schard package (v0.0.1). Low-quality cells were removed if they met any of the following criteria: fewer than 10 counts, fewer than 10 unique genes, area < 8 µm², or >15% mitochondrial reads. Additionally, cells labeled only through gene expression segmentation (secondary labels) were excluded upon manual inspection for falling outside tissue boundaries. In a second quality control step, the isOutlier function from the scuttle package (v1.16.0) was used to flag outliers in transcript count and transcript density (log2(counts / area)) using parameters nmads = 2.5, type =

"both", and log = FALSE. Identified outliers were excluded from downstream analysis. For pre-processing, quality-filtered SingleCellExperiment objects were normalized using logNormCounts from scuttle. Highly variable genes (HVGs) were identified with modelGeneVar (scran[6] v1.34.0), blocking by patient ID (block = sce$patient). HVGs were selected using getTopHVGs (fdr.threshold = 0.05). PCA was performed using runPCA (scater v1.34.0) (*93*) on the HVGs (subset_row = hvgs), and the first 15 principal components were retained based on elbow plot inspection. UMAP dimensionality reduction was computed using runUMAP (scater).

To cluster cells, we built a shared nearest-neighbor (SNN) graph using buildSNNGraph from scran with type = "jaccard" and use.dimred = "PCA". Louvain community detection was performed using cluster_louvain (igraph[7] v2.1.1) at multiple resolutions. Differentially expressed genes (DEGs) between clusters were identified using findMarkers (scran) with direction = "up". Top-ranked markers for each cluster were selected from the "Top" column of the results and inspected manually to guide spatial annotation. Hallmark gene sets (e.g., angiogenesis, hypoxia) were obtained from MSigDB using the msigdbr package (v7.5.1) with species = "Homo sapiens" and category = "H". Immune cell-type signatures (*94*) were retrieved using category = "C8" and filtered to retain adult lung signatures while excluding fetal profiles. Signature scoring was performed using AUCell (v1.28.0). Gene expression rankings per cell were computed with AUCell_buildRankings, followed by AUC calculation with AUCell_calcAUC. Neutrophil hub scores were computed analogously. For visualization, cluster-level mean AUC scores were obtained using aggregateAcrossCells (scuttle (*93*)) with statistics = "mean" and use.assay.type = "AUC". Signature scores were quantile-normalized to the 1st and 99th percentiles using quantile (probs = c(0.01, 0.99)) and capped at ±2.5 standard deviations for heatmap representation (pheatmap package, v.1.0.12) with arguments scale = "row", cluster_cols = TRUE, cluster_rows = FALSE.

Neighborhood analysis

Spatial transcriptomic data were analyzed using Seurat (v4.3) in R (v4.2). A spatial proximity graph was constructed by computing the k-nearest neighbors (k = 6) from each spot's x–y coordinates using the RANN package. Edges exceeding 250 units in Euclidean distance were excluded to account for realistic cell-cell interaction radii. An undirected graph was generated using the igraph package, with edge weights corresponding to physical distances. We implemented two complementary functions to quantify spatial cell type context: 1) Neighborhood Frequency Analysis. For a given set of target spots (e.g., neutrophils), their first-order neighbors were identified within the spatial graph. For each neighbor, the cell type label was extracted, the number of neighboring cells of each type was counted per target spot and aggregated across all targets to calculate the mean and 95% confidence interval (CI) for each cell type. This allowed identification of the most frequently co-localized cell types around a given population. 2) Neighborhood Composition by Hub: In a separate analysis, both the target spot and its neighbors were pooled to represent a local "neighborhood." Cell types within each neighborhood were classified using a curated cell type annotation. For each neutrophil hub, cell type counts were summed and normalized to percentages, excluding spots annotated as "unassigned" to avoid skewing proportion estimates. This enabled comparative analysis of cellular composition across microenvironments.

MACSima Imaging Cyclic Staining (MICS)

Sample preparation and image acquisition

Multiplex immunohistochemistry of lungs from naïve, flu-infected, or tumor-induced mice was performed using a MACSima imaging system (Miltenyi Biotec). In brief, cyclic immunofluorescence imaging consisting of repetitive cycles of immunofluorescent staining, sample washing, multi-field imaging, and signal erasure by photobleaching was performed. Cryosectioned fixated lungs from the three groups were placed on microscopy slides and MACSwell sample carriers were mounted and blocked using a blocking buffer containing 10% BSA and 2% goat serum for 1h at RT before lungs were preincubated with an antibody to IFIT1 (ab236256, Abcam, 1:100) overnight at 4°. Thereafter, nuclei were counterstained with DAPI before samples were placed in the MACSima imaging system.

Neutrophil subsets were identified using directly-conjugated antibodies against Ly6G (1A8, Miltenyi Biotec, PE,1:50), CD11b (M1/70, Miltenyi Biotec, APC, 1:50), PD-L1 (10F.9G2, BioLegend, APC, 1:50), CD14 (Sa14-2, BioLegend, PE, 1:50), Ly6C (REA796, Miltenyi Biotec, PE,1:50), CXCR2 (SA044G4, BioLegend, PE, 1:25), CD45 (REA737, Miltenyi Biotec, FITC,1:50), MHC-II (REA813, Miltenyi Biotec, APC,1:50) and a conjugated anti-rabbit antibody (goat, Sigma-Aldrich, FITC, 1:100) in the first cycle to identify IFIT1. The tissue location was characterized using an anti-Podoplanin antibody (8.1.1, BioLegend, PE, 1:50).

Data analysis and visualization

Images were stitched and pre-processed using MACS iQ View Analysis Software (Miltenyi Biotec) and representative overlay pictures were displayed. For downstream analysis, cells were segmented based on the DAPI signal using the StarDist plugin in ImageJ (NIH) and the donut algorithm in MACS iQ View. The segmented data was then exported for further analysis to FlowJo (BD Biosciences) where neutrophils were identified as Ly6Ghigh cells using a threshold value. In flu-infected lungs, neutrophils were characterized as intravascular or extravasated based on the podoplanin signal in the segmented neutrophils. Neutrophils from all ROIS were concatenated and phenotypically analyzed by dimensional reduction using the UMAP plugin and unsupervised clustering using the FlowSOM plugin. FlowJo and R were used for visualization.

Mathematical modelling for blood neutrophil diagnosis

To model the predictive value of the distribution of blood neutrophils in the NeuMap, we used the density overlap represented by the Bhattacharyya index. We favored density versus spatial overlap to reduce the impact of outliers in our calculations. We also favored using 10 selected regions of the NeuMap over the 7 hubs delineated in Figure 1E to gain spatial resolution of cell distribution over the specific areas of the NeuMap where blood neutrophils from the tested conditions tended to concentrate. Indeed, in separate analyses we found that the spatial overlap not based on densities, and the use of 7 hubs provided significantly less resolution in the overlap barcodes (not shown).

Density state estimation. The UMAP coordinates $\{x_j, y_j\}$ of the neutrophils collected from the tissue hubs and blood samples were pipelined into a computational approach to estimate the probability density functions (PDFs) over the Neumap transcriptomic space associated with these datasets. The kernel density estimators $\hat{f}(x,y)$ were of the from (*95*),

$$\hat{f}(x,y) = \frac{1}{nh_x h_y}\sum_{j=1}^{n} \quad K\left(\frac{x_j - x}{h_x}\right) K\left(\frac{y_j - y}{h_y}\right) ,$$

where K is the Epanechnikov kernel

$$K(u) = \{\frac{3}{4}(1-u^2)\,, \qquad for\ |u| \le 1, \quad 0\,, \qquad otherwise,$$

with n, h_x and h_y denoting the number of points and the bandwidths along two orthogonal directions, respectively. This kernel choice, which is symmetric and normalized along each orthogonal direction, ensures a smooth, bounded, and efficient computation of the density estimates. The determination of each kernel's bandwidths, which influences the smoothness and accuracy of the resulting PDF estimate, was made via the Sheather-Jones method (*76*). This technique employs a data-driven approach that minimizes the mean integrated square error of the estimated density function. By iteratively adjusting the bandwidths h_x and h_y and evaluating their performance, Sheather-Jones effectively balances bias and variance, resulting in accurate density estimates, particularly for *tissue hubs* and *blood samples* that present non-Gaussian distributions or multimodality.

Overlap integration. Upon estimating the PDFs of our datasets, we assessed the degree of overlap between pairs of these functions. For this purpose, we employed the Bhattacharyya index, which yields a measure of the amount of overlap between two PDFs $f(x,y)$ and $g(x,y)$. The Bhattacharyya index was defined by the integral expression

$$BC(f,g) = \iint \sqrt{f(x,y)g(x,y)}\, dx\, dy,$$

where the double integral runs over the entire domain defined by the NeuMap. The Bhattacharyya index gives a scalar value in the interval $[0,1]$, enabling a direct interpretation of the overlap: values near 1 suggest a high degree of similarity, or almost perfect overlap, between the two distributions, indicating that the neutrophil states are nearly indistinguishable within the dimensionally reduced transcriptomic space. Conversely, values near 0 denote little to no overlap, pointing to distinct neutrophil states with minimal similarity in their respective distributions within the dimensionally reduced transcriptomic space.

To calculate the Bhattacharyya index, we used an adaptive Monte Carlo method (*96*) that combines adaptive importance and stratified samplings over multiple iterations, thus optimizing the sample distribution around the peaks of the PDFs and thereby reducing the standard deviation in the estimates. This approach yielded accurate values of the multidimensional integrals and hence offered robust measures of the overlap between the PDFs. While the Bhattacharyya index does not constitute a true probability measure, its bounded nature makes it a valuable score for comparing the similarity of data distributions in a normalized manner. From the computed Bhattacharyya indexes, the resulting barcodes were generated. To perform our calculations, we used the R programming language to analyze all datasets. Specifically, we employed the *MASS*, *graphics*, *stats* and *vegas* R packages.

Estimation of neutrophil lifetimes

To quantify the neutrophil half-lifes and transit times, we employed an age-structured mathematical model as previously proposed (*16*). This model effectively captures the temporal variation in the proportion of labeled neutrophils following the administration of the BrdU pulse. Let $u = u(t,a)$ denote the density of neutrophils, which at time t, have an age a. We assume that their age ranges in the interval $a \in [0, a_{max}]$, where a_{max} is the maximum age (or the maximum lifespan) a neutrophil can achieve in the different examined tissues. In practice, this age can be taken sufficiently large without appreciably altering the numerical results for the entire neutrophil population. To describe the temporal dynamics of the age distribution in neutrophils, we considered the following first-order linear transport partial differential equation

$$\frac{\partial u}{\partial t} + \frac{\partial u}{\partial a} = -\frac{u(t,a)}{\tau(a)} + \phi(t,a). \qquad (1)$$

The left-hand side of (1) represents the temporal change in the number of neutrophils along with their corresponding age. The first term on the right-hand side accounts for neutrophil death. The death time, $\tau(a)$, generally depends on the age of the neutrophil. The introduction of a flux function, $\phi(t,a)$, encapsulates the net recruitment of neutrophils entering or leaving the target tissue. Assuming that at time $t = 0$ no BrdU$^+$-labeled neutrophils of any age have yet arrived at tissue i, the initial condition is $u(0,a) = 0$. Therefore, the exact solution to (1), obtained using the method of characteristics for first-order partial differential equations, is

$$u_i(t,a) = e^{-\int_0^t \frac{d\xi}{\tau_i(a-\xi)}} \int_0^t \phi_i(\xi, a-t+\xi) e^{\int_0^\xi \frac{d\eta}{\tau_i(a-t+\eta)}} d\xi. \quad (2)$$

Equipped with expression (2), we computed the total number of neutrophils at time t and tissue i, irrespective of their age, via the following integral

$$n_i(t) = \int_0^{a_{max}} u_i(t,a)\, da. \qquad (3)$$

To connect (2) with the different scenarios addressed in the experiments, the net flux $\phi_i(t,a)$ corresponded to one synchronous wave of neutrophils after administration of the BrdU labeling. The chosen functional forms for $\tau_i(a)$ and $\phi_i(t,a)$ in our modelling were

$$\tau_i(a) = \tau_i, \qquad \phi_i(t,a) = \alpha_i e^{-\frac{(t-t_i)^2}{2\sigma_i^2}}, \qquad (4)$$

where τ_i, α_i, t_i, and σ_i are constant parameters. Inserting (2) and (4) into (3), we arrive at the following exact formula for the total number of neutrophils at a given tissue i at time t

$$n_i(t) = m_i e^{-\frac{t}{\tau_i}} \left[Erf\left(\frac{\sigma_i^2 + t_i \tau_i}{\sqrt{2}\sigma_i \tau_i} \right) - Erf\left(\frac{\sigma_i^2 + (t_i - t)\tau_i}{\sqrt{2}\sigma_i \tau_i} \right) \right], \quad (5)$$

where

$$m_i = \sqrt{\frac{\pi}{2}}\, \alpha_i \sigma_i a_{max} e^{\frac{\sigma_i^2 + 2t_i\tau_i}{2\tau_i^2}}, \qquad (6)$$

is a normalization parameter for tissue i, and $Erf(x) = \frac{2}{\sqrt{\pi}} \int_0^x e^{-\xi^2} d\xi$ is the error function. The parameters τ_i, m_i, t_i, and σ_i for blood, bone marrow and spleen were computed via a nonlinear regression analysis using the corresponding time series measured from day 1 to day 7 for each tissue compartment. Once these four parameters were found for each tissue i, the mean half-life time $t_{1/2}^{(i)}$ and transit time $t_{tran}^{(i)}$ were estimated from the normalized profile (5). To do that, the transit time was identified as the time at which this unimodal profile achieves its maximum (100% of the BrdU-labeled neutrophils in tissue i). Subsequently, the 50% level was set as a reference for the mean half-life time $t_{1/2}^{(i)}$. The approach for calculating these two lifetimes is illustrated in Extended Data Fig. 5F**.** The bands shown in this figure correspond to a confidence level of 0.75.

To carry out the density state estimation and overlap integration, we used the R programming language to analyze all datasets. Specifically, we employed the *MASS*, *graphics*, *stats,* and *vegas* R packages. The nonlinear regression and statistical analysis were performed with Matlab (R2024a) using the functions *fitnlm* and *coefCI*.

Quantification and Statistical Analysis

Data from experiments are represented as mean values ± SEM. All parameters analyzed followed normal distribution as tested by D'Agostino-Pearson test unless indicated in the figure legend. Unpaired two-tailed t test was used when 2 groups were compared, and comparison of more than two datasets was done using one-way analysis of variance (ANOVA) with Tukey's post-test or two-way ANOVA. Log-rank analysis was used for Kaplan-Meier survival curves. Statistical analysis was performed using GraphPad software. Statistics on the RNA sequencing are indicated in the analysis section. A P value below 0.05 ($*$) was considered statistically significant; P values ≤ 0.01 ($**$) and P ≤ 0.001 ($***$), as well as nonsignificant differences (n.s.) are indicated accordingly.

Data and Code Availability

All the transcriptomics data are available in Gene Expression Omnibus (GEO) Super-series GSE266680; Single-cell transcriptomics and spatial data (GSE266518) (token for reviewers: kvmhgwmstnkldsp), Dogma (GSE266930) (token for reviewers: qfivoasgdhsndst), Bulk (GSE266678) (token for reviewers: mrmxmkwondgvvmz). Visualization and analysis of the NeuMAP is available at the single-cell Data Analysis and VISualization scDAVIS (scDAVIS) web-based tool: https://bioinfo.cnic.es/scdavisr/ (Credentials for reviewers: user: neumap; pass: 0gl4d1h).

Supplementary Figures

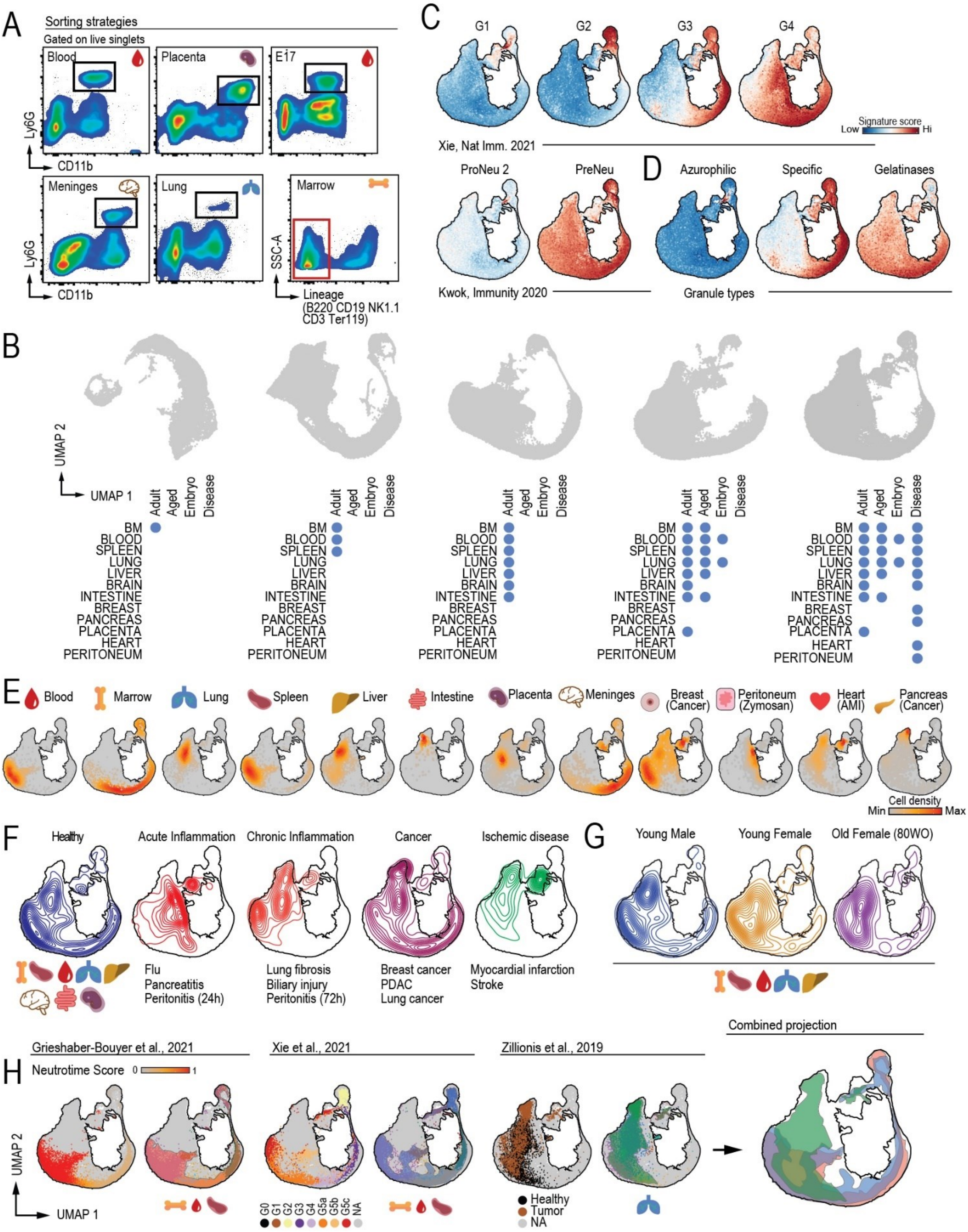

Extended Data Figure 1. NeuMAP, a map of the neutrophil transcriptome. (**A**) Plots showing the sorting strategy to isolate neutrophils from the indicated tissues. Note the different gating for the bone marrow. (**B**) Score expression on the NeuMap of published gene sets associated with neutrophil differentiation and maturation. (**C**) Score values of genes expressed in primary, secondary and specific granules onto the NeuMAP. (**D**) Evolution of the NeuMAP by the cumulative addition of neutrophils from the indicated tissues. (**E**) K-mass score of neutrophils by the indicated tissue of origin in the NeuMAP. (**F**) Contour plots of the combined neutrophils from the indicated tissues in various conditions of disease. (**G**) Contour plots of the combined neutrophils from the indicated tissues of males, females and old (80 week-old) individuals. (**H**) Mapping of neutrophils from the indicated studies, showing their distribution in the NeuMap.

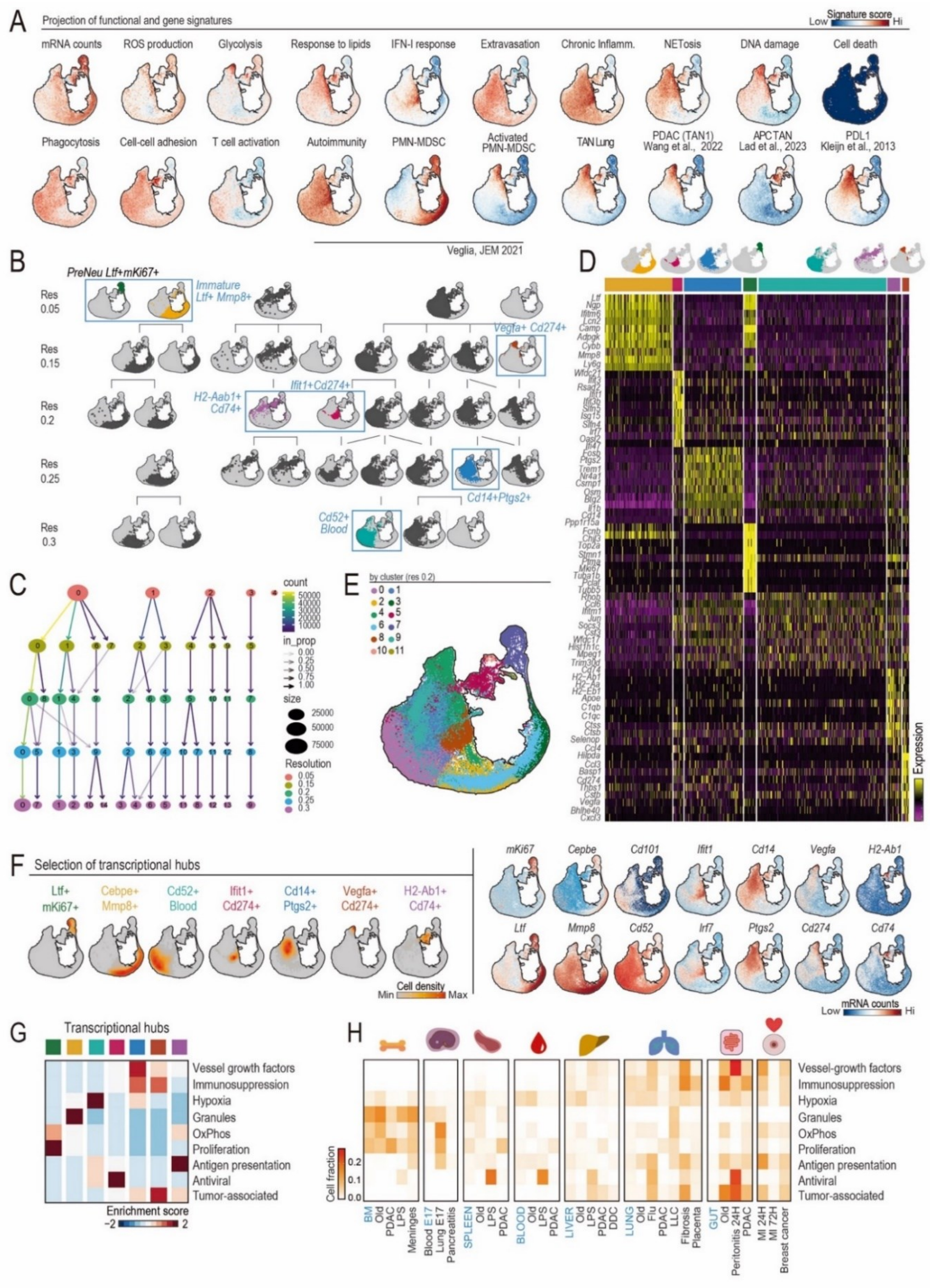

Extended Data Figure 2. Identification of clusters and transcriptional hubs in the NeuMap. (**A**) Score expression of gene sets from specific biological processes. See Table S2 for a complete gene list. (**B**) Clustering of the NeuMap with different levels of resolution. The clusters that best captured the functional areas were selected across the different resolutions to annotate the transcriptional hubs of the NeuMAP (as in Figure 1). (**C**) Clustering tree of 151,960 neutrophils from R0.05 to R0.3, with clusters labeled according to their size. The arrow intensity reflects the proportion of cells and the color of the number of cells assigned to the other clusters. (**D**) Heatmap of the differentially expressed genes for each transcriptional hub. For a complete gene list see Table

S3. (**E**) Clustering of the NeuMap at resolution 0.2. (**F**) Transcriptional hubs from (**B**) and mRNA expression of the indicated genes. (**G**) Heatmap showing the enrichment scores of the functional signatures in the transcriptional hubs **(H)** Heatmap showing the proportion of cells in all the conditions included in the NeuMap that contribute to the top 5% expressing cells for each indicated functional gene signature. The number of cells per tissue was downsampled to 1000 prior to the calculation of the contribution proportion.

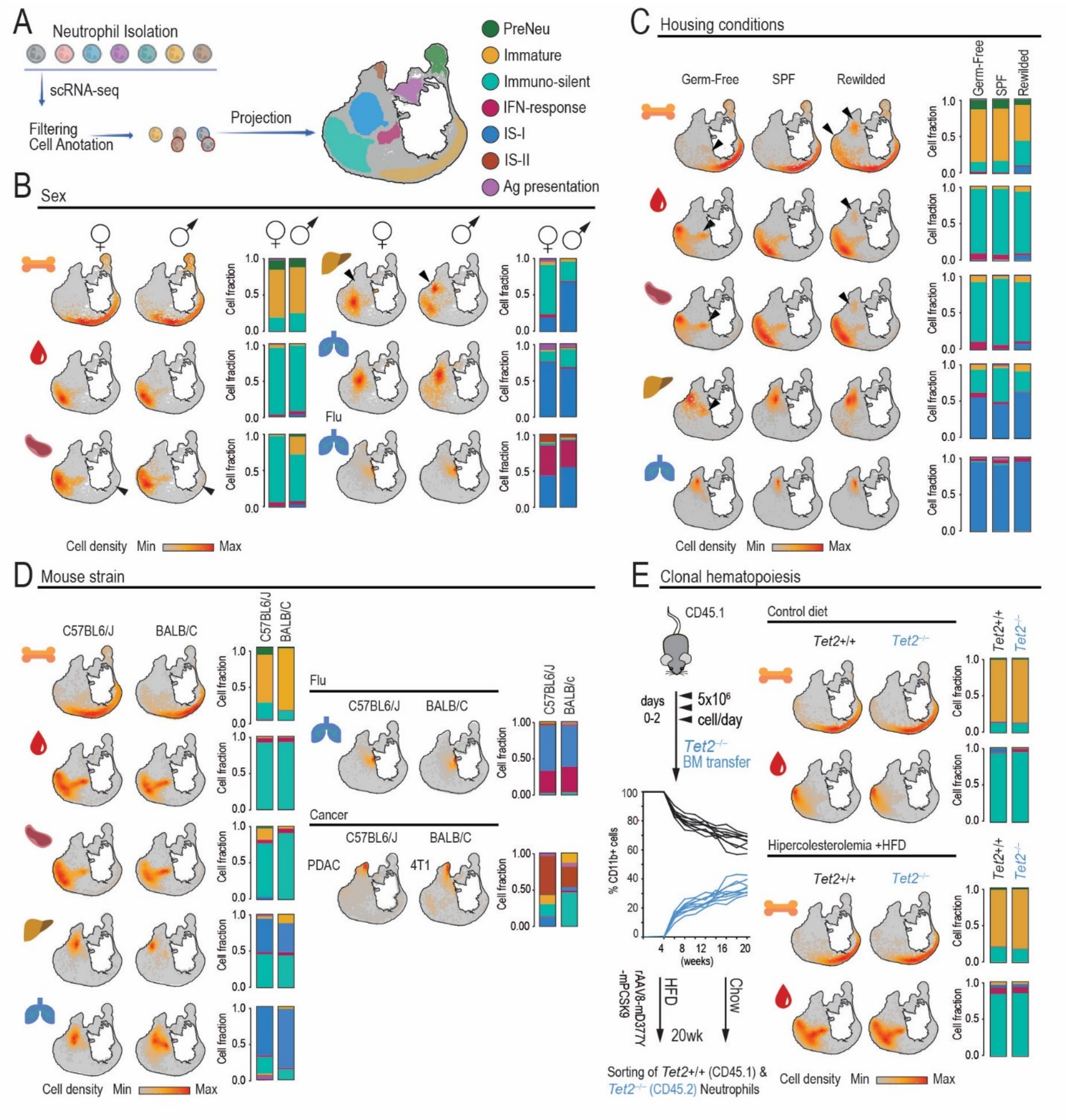

Extended Data Figure 3. Architecture of the NeuMap across sex, environmental conditions, mouse strains, and genetic alterations. (A) Experimental strategy and projection onto the NeuMap to assess neutrophil distribution across transcriptional hubs. (B) K-mass density plots and stacked bar graphs showing hub distribution of neutrophils from healthy tissues and influenza-infected lungs, separated by sex (male and female). (C) K-mass scores and hub distributions of neutrophils isolated from indicated tissues in naïve male mice housed under germ-free (GF), specific pathogen-free (SPF), or rewilded (RW) environmental conditions. (D) K-mass scores and hub distributions of neutrophils from healthy tissues, flu-infected lungs, and tumors in C57BL/6J and BALB/c mice, showing conserved hub structure across mouse strains. (E) K-mass scores and hub distributions of wild-type and Tet2^{-}/$^{-}$ neutrophils isolated from non-irradiated bone marrow chimeras, under control (upper panels) or hypercholesterolemic (lower panels) conditions, illustrating hub preservation across genetic backgrounds.

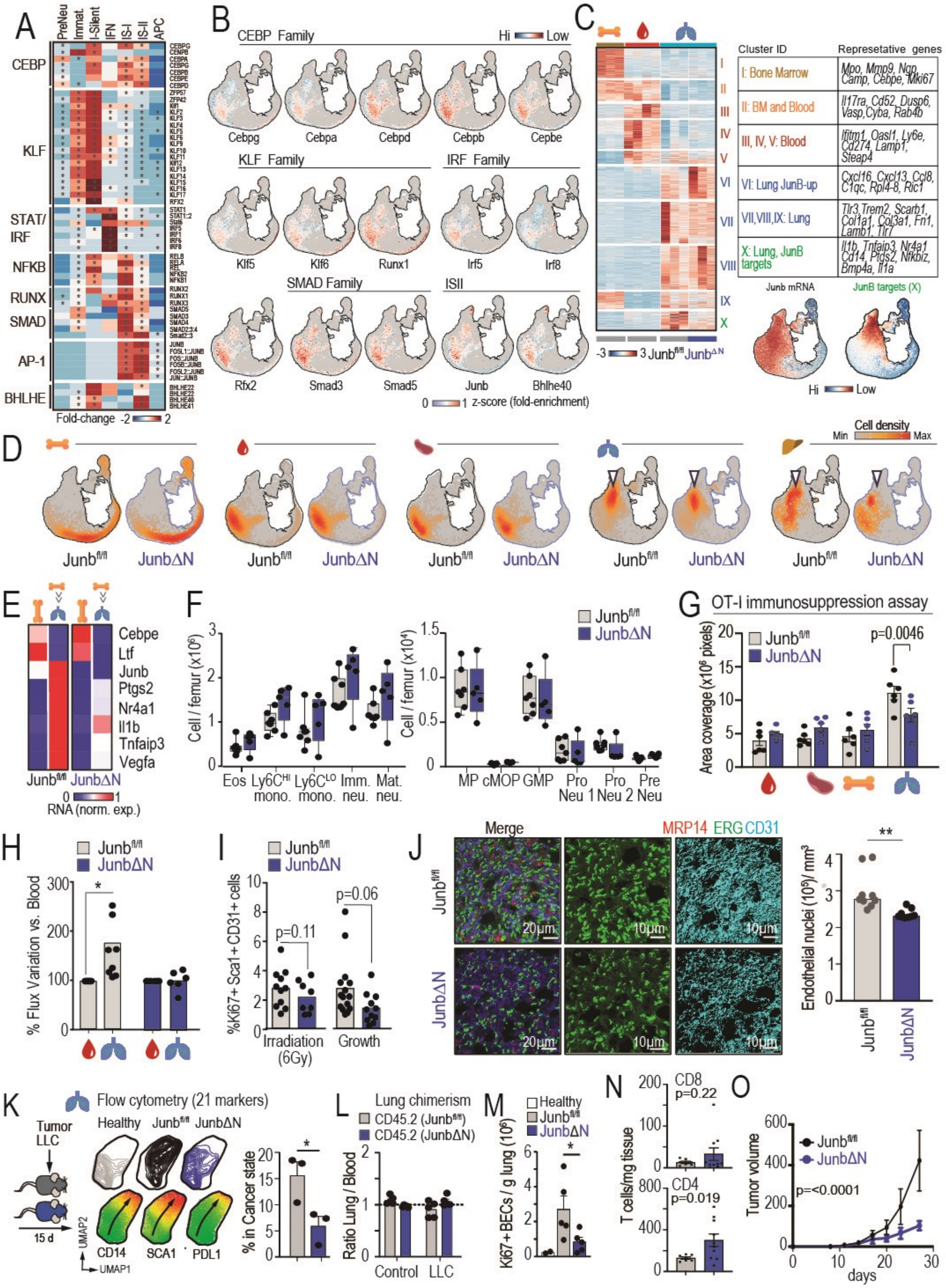

Extended Data Figure 4. Characterization of JunbΔN mice. (**A**) Heatmap showing the fold enrichment in binding sites for the indicated transcriptional factors (TF) associated with each hub. Significant motif enrichment values are marked with * (**B**) chromatin accessibility scores for the indicated TF projected onto the NeuMAP, as determined by scATAC-sequencing combined with scRNA-seq (Dogma-seq). For a complete list of enriched motifs see Table S4. (**C**) Heatmap of differentially expressed genes obtained by bulk RNA-seq of neutrophils from the BM, blood, and lung of wildtype mice, and lung of JunBΔN mice, as indicated in the table at right. Bottom right, JunB mRNA levels and signature of JunB target genes are projected in the NeuMAPs. For a complete list of

DEGs see Table S5. (**D**) K-mass values of neutrophils obtained from BM, blood, lungs, spleen, and livers of control Junb$^{fl/fl}$ and JunBΔN mice. (**E**) Expression of the indicated genes by RT-PCR analysis of Junb$^{fl/fl}$ and JunBΔN BM neutrophils, before and after intratracheal transfer into the lungs of WT mice. (**F**) Quantification of immature and mature myeloid cell progenitors and mature populations in the BM of control Junb$^{fl/fl}$ and JunBΔN mice. Eo, eosinophils, Mono, monocytes, Imm. Neu, immature neutrophils, Mat.neu, mature neutrophils; CMP, common myeloid progenitor; cMoP, common monocyte progenitor; GMP,granulocyte-monocyte progenitor. (**G**) Quantification of OT-1 T cell killing of B16OVA target cells in the presence of neutrophils from the indicated tissues of control Junb$^{fl/fl}$ and JunBΔN mice. (**H**) Quantification of the vascularization of Matrigel plugs coinjected with blood or lung neutrophils from control and JunBΔN mice, as assessed by Doppler analysis. (**I**) Percentage of proliferative endothelial cells (Ki67+ Sca1+ CD31+) in lungs from control and JunBΔN mice after irradiation (left) or during organismal growth (4-week-old mice; right). (**J**) Representative images and quantification of the density of CD31+ ERG+ endothelial cells (MRP14) in control and JunBΔN mice. (**K**) Experimental setup and multiparametric cytometric analysis (21 markers) of lung neutrophils from LLC tumors implanted in Cre^{NEG} control and JunBΔN mice. The UMAP projections show the distribution of neutrophils from each mouse and the expression of CD14, Sca1 and PDL1. Right, percentage of control and JunB-deficient neutrophils that acquire the "Cancer" phenotype. Data is from 3 mice. *, $p < 0.05$ as determined by Student's t-test. (**L**) Ratio of Cre^{NEG} control and JunBΔN neutrophils that infiltrate the lungs relative to the numbers in blood, in naïve and LLC tumor-bearing mice, using transplantation chimeric mice. Data is from 5 mice per group. (**M**) Number of proliferative endothelial cells (BECs) in the lungs of healthy and tumor-bearing mice 3 weeks after tumor implantation. BECs were analyzed by flow cytometry. Data is from 5-6 mice per group. *, $p<0.05$ as determined by one-way ANOVA with multigroup test. (**N**) Absolute number of CD4 or CD8 T cells infiltrating LLC tumors in control and JunBΔN mice; data from 7-10 mice. (**O**) Volume of subcutaneous LLC implanted tumors in control versus JunBΔN mice over time; n=10-12.

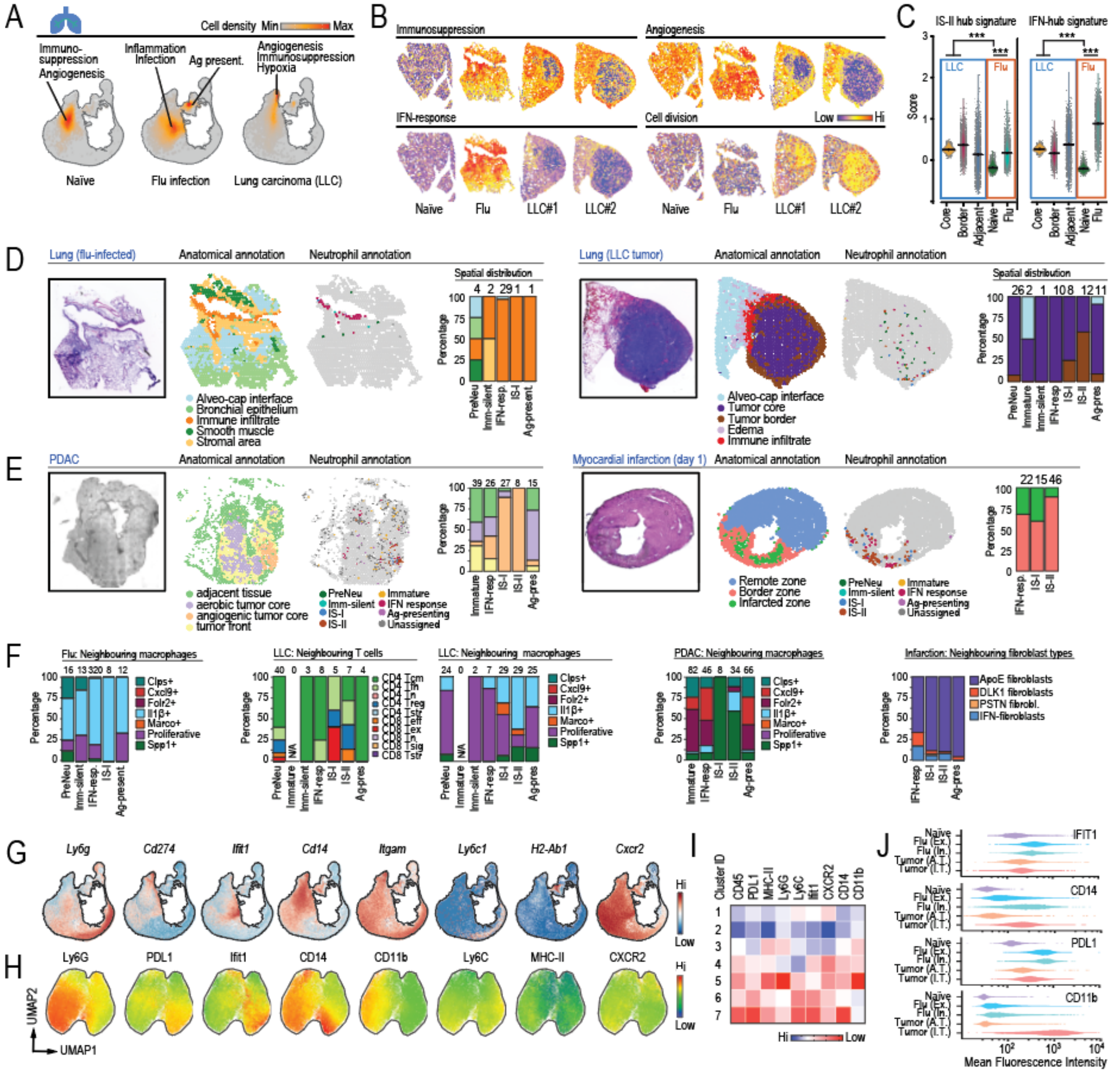

Extended Data Figure 5. Spatial characterization of neutrophils. (**A**) K-mass score of neutrophils from lungs of naïve, tumor-bearing, and flu-infected mice. (**B**) Score of the indicated signatures onto the spatial transcriptomic dataset in the naïve, tumor-bearing, and flu-infected lung sections. (**C**) Enrichment scores of neutrophils for the IS-II and IFN-response signatures. (**D**) H/E staining of lungs from tumor-bearing (LLC), and flu-infected lung sections. Deconvolution using LungMap Project3 allows annotation of cells the tissues used for spatial transcriptomics. Right, bars show the percentage distribution of neutrophils assigned to the indicated hubs in the different annotated regions of the tissue. (**E**) Analyses as in (**D**) performed in a PDAC tumor (from (*4*)) and an infarcted myocardial tissue (one day after ischemia; from (*24*)). (**F**) Percent of closest neighbouring cells (macrophages, T cells or fibroblasts) featuring the indicated profiles to neutrophils from the different hubs. The numbers on top indicate the number of neighbouring cells around neutrophils from each hub, when available. (**G**) Expression of the indicated genes encoding for surface markers in the NeuMAP, and (**H**) expression of the respective proteins represented in the UMAP generated with neutrophils stained using the MACSima platform (see Methods). (**I**) Heatmap showing the expression of the indicated proteins in the neutrophil clusters identified using MACSima. (**J**) Mean fluorescence expression intensity of the indicated proteins in neutrophils in different regions of the tissues analyzed by multiparametric immunofluorescence. Ex, extravascular; In, intravascular; AT, adjacent tissue; IT, intratumoral.

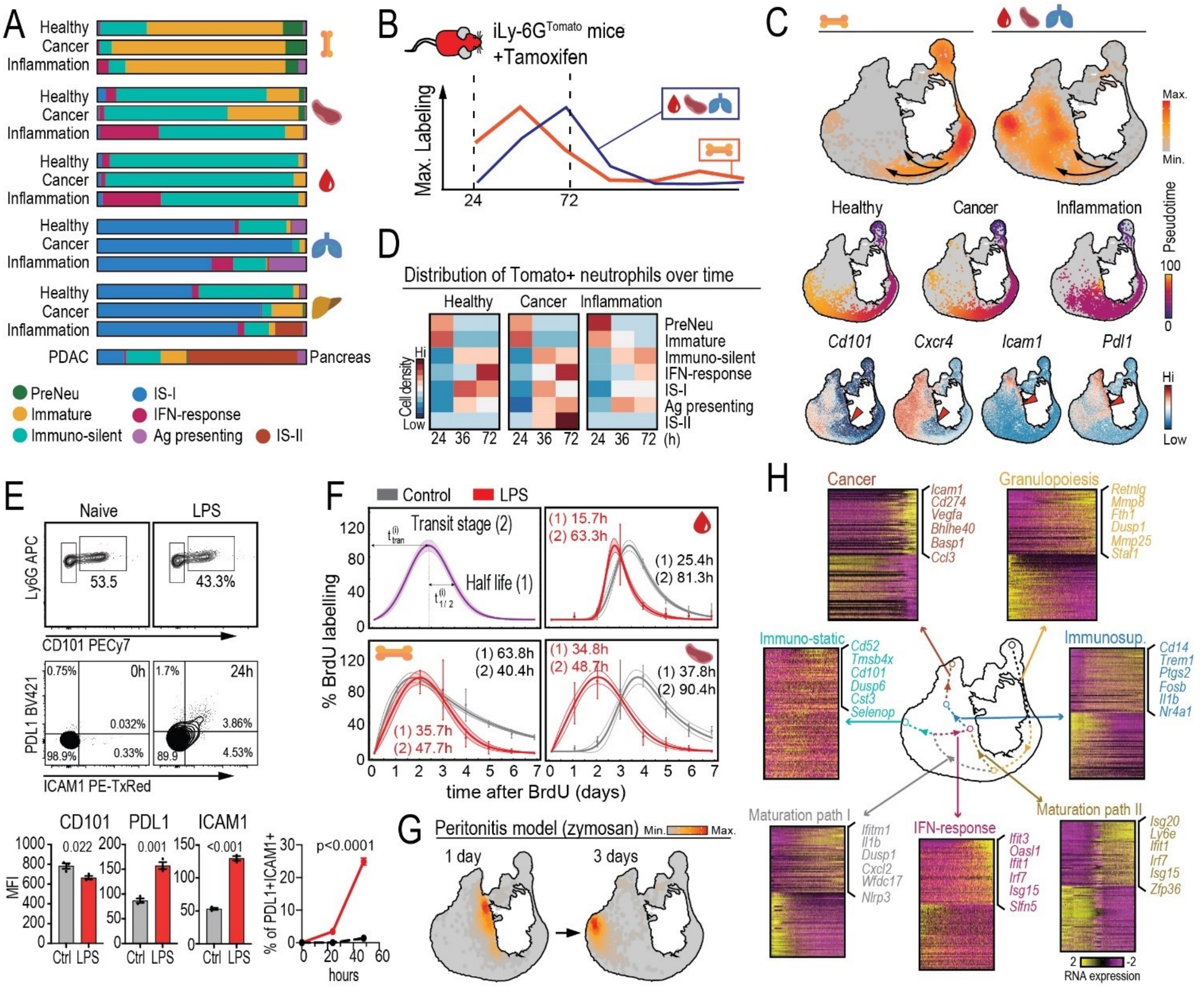

Extended Data Figure 6. Dynamics of neutrophil maturation. (**A**) Fraction of neutrophils in the different transcriptional hubs for the indicated tissues and conditions of naive, tumor-bearing or LPS treated mice (**B**) Experimental setup for the timestamp experiment in iLy6GtdTomato mice, showing the frequency of Tomato+ neutrophils in the indicated tissues at different times after tamoxifen administration. Neutrophils were collected from BM (24h), and tissues (36 and 72h). (**C**) Upper panels, cell density (K-mass) in the NeuMap of pulse-labelled neutrophils from the BM (left) or tissues (right) of naïve, tumor-bearing, and flu-infected mice. Middle panels, pseudotime scores of BM neutrophils from the three conditions. Lower panels, expression of relevant maturation and activation genes projected in the NeuMap. (**D**) Heatmap showing the distribution of Tomato+ neutrophils along the different transcriptional hubs over time, determined from the timestamp experiment. (**E**) Flow cytometric plots and quantification of mature blood neutrophils (CD101+ Ly6G+), and expression of PDL1 and ICAM1 in BM neutrophils in response to LPS treatment, and kinetics of the percentage of PDL1+ ICAM1+ cells over time after LPS treatment. (**F**) *In vivo* kinetics of neutrophils from the indicated organs showing their transition from the BM to blood and to spleen of naïve or LPS-treated mice, determined by BrdU staining. (**G**) Transcriptional distribution in the NeuMAP of peritoneal-infiltrating neutrophils at 1 and 3 days of zymosan injection. (**H**) Representative genes that change along the trajectories defined in Figure 3E. For the complete set see Table S6.

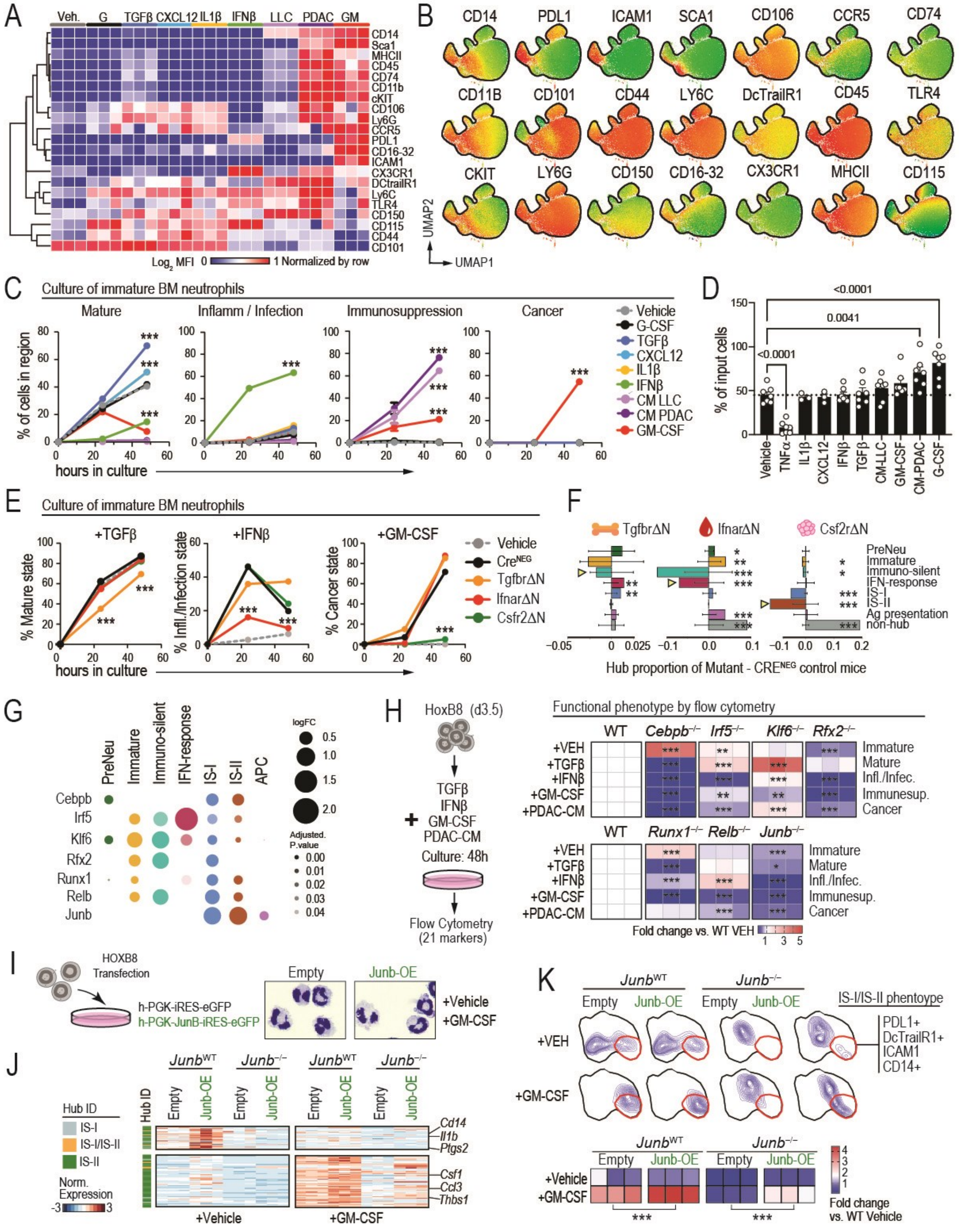

Extended Data Figure 7. Analysis of ex vivo neutrophil cultures. (**A**) Heatmap showing expression of 21 markers in mature neutrophils treated with the indicated cytokines and conditioned media for 24h. G, G-CSF, CM LLC, conditioned medium of LLC cells; CM PDAC, conditioned medium of FC1242 pancreatic cancer cells; GM, GM-CSF. (**B**) Projection of marker expression in the UMAP obtained by multiparametric flow cytometry. (**C**) Percentage of neutrophils classified as "Mature", “Inflammation/infection”, ”Immunosuppression“, and “Cancer” after ex vivo culture for 24 and 48h with the indicated cytokines and conditioned media. Data is from 4 independent experiments. **, $p<0.01$; ***, $p<0.001$ compared with the vehicle group at the respective time point, as determined by Two-way ANOVA. (**D**) Percentage of viable cells after ex vivo culture of neutrophils for 48h with the indicated treatments. (**E**) BM neutrophils from control Cre^{NEG}, TgfbrΔN, IfnarΔN and Csf2rΔN mice were cultured ex vivo for 24 and 48h with TGFβ, IFNβ and GM-CSF. The plots show the percentage of neutrophils with a "Mature" phenotype after treatment with TGFβ, an "Inflammation/infection" phenotype after treatment with IFNβ, and a "Cancer" phenotype after treatment with GM-CSF. Data is from 3 independent experiments and statistics are as in (C). ***, p0.001 as determined by two-Way ANOVA. (**F**) Changes in the distribution of neutrophils from TgfbRΔN, Ifnar1ΔN and Csf2rΔN mice across the transcriptional hubs of the NeuMap, determined by scRNA-sequencing relative to Cre^{NEG} control mice. The arrowheads indicate the more relevant hubs examined for each mutant, as determined from Fig.4H. P values comparing the distribution of control vs. mutant cells were calculated using a bootstrap approach (see Methods). (**G**) Transcription factor (TF) enrichment across NeuMap transcriptional hubs, identified by DOGMA-seq. Dot size indicates odds ratio, and color intensity reflects the adjusted p-value. (H) Functional profiling of HoxB8-derived neutrophils lacking the indicated TFs (Cebpb, Irf5, Klf6, Rfx2, Runx1, Relb, JunB) or wild-type controls, after 48h treatment with the indicated cytokines or PDAC-conditioned medium. Heatmaps show the proportion of cells in each phenotypic cluster (Immature, Mature, Inflammation/Infection, Immunosuppression, Cancer), based on flow cytometry marker expression. Data are from three independent experiments. **p<0.01, ***p<0.001, One-way ANOVA. (**I**) Schematic representation of JunB overexpression in HoxB8 progenitors using lentiviral transduction. Representative cytospin images of control and JunB-overexpressing neutrophils at day 5 post-estrogen withdrawal confirm comparable polymorphonuclear morphology. (**J**) Heatmap showing differentially expressed IS-I/IS-II-associated genes identified by bulk RNA sequencing of HoxB8-derived neutrophils (wild-type; $\textit{Junb}^{\text{WT}}$, JunB knockout; $\textit{Junb}^{-/-}$, or JunB-overexpressing; OE) cultured for 48 hours with vehicle or 10ng/ml GM-CSF. (**K**) UMAP contour plots derived from multiparametric flow cytometry (21 markers) of HoxB8-derived neutrophils from the same experimental groups as in (J), after 48-hour culture with vehicle or GM-CSF. Heatmaps below indicate the proportion of cells within the IS-I/IS-II-associated gate for each condition. Data represent n = 3 independent experiments. ***p < 0.001, one-way ANOVA.

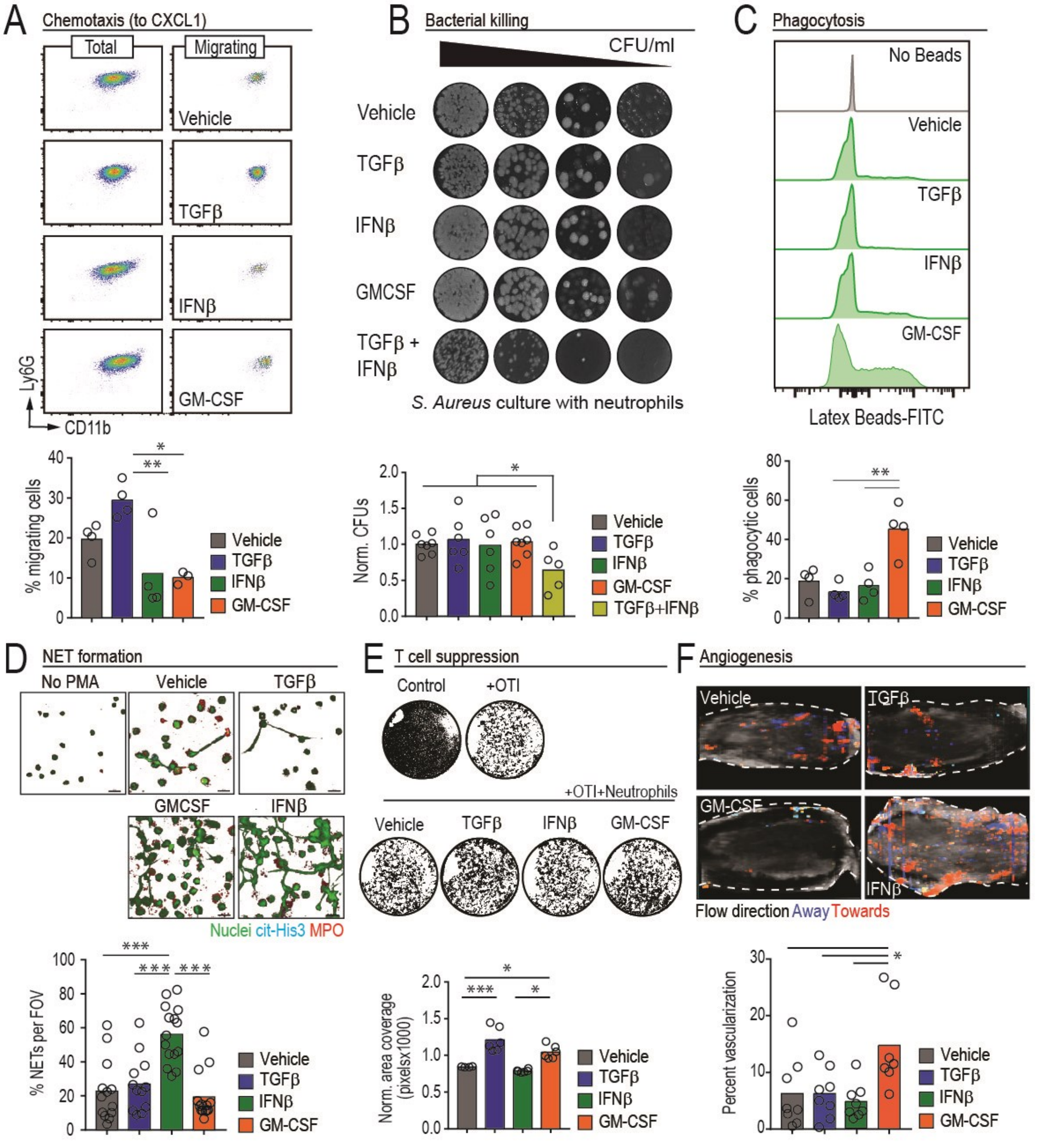

Extended Data Figure 8. Functional properties of cytokine-treated neutrophils. BM-derived neutrophils were treated with vehicle, TGFβ, IFNβ, or GM-CSF for 48h before being subjected to (**A**) migration to CXCL1 in Boyden chambers, and quantified by flow cytometry, illustrated by the dot plots and quantified in the bar graphs. Data is from 3-4 biological replicates per group. (**B**) Bacteria killing assays, for which *S. aureus* was incubated with the cytokine-treated neutrophils. Data is from 6-7 biological replicates per group, and show as fold-increase number of bacteria CFUs over vehicle. (**C**) Phagocytosis of fluorescent latex beads measured by flow cytometry in the representative histograms and shown as the percentage of fluorescent neutrophils. Data is from 4 biological replicates per group. (**D**) NET-forming capability of the cultured neutrophils after treatment with PMA. NETs were identified by staining for MPO and citrullinated histone 3 (cit-H3) and quantified as the percentage of field of view (FOV) occupied by NETs. Data is from 3-4 biological replicates per group and 3-5 technical replicates per sample. (**E**) T-cell immunosuppression assay. The cultured neutrophils were co-incubated with OT-I T cells before performing killing assays on B16F10-OVA cells. Data is from 4-6 biological replicates per group. (**F**) Angiogenesis assays. The cultured neutrophils were co-injected subcutaneously with LLC cancer cells in the back of WT mice, and the vascularization of tumors was measured 15 days after implantation using a Color Doppler Vevo Ultrasound system. Color indicates blood flow. Data is from 7-8 biological replicates per group. All bars show means. ***, p<0.001; **, p<0.01; *, p<0.05 as determined by One Way ANOVA with Tukey's post-test for all assays.

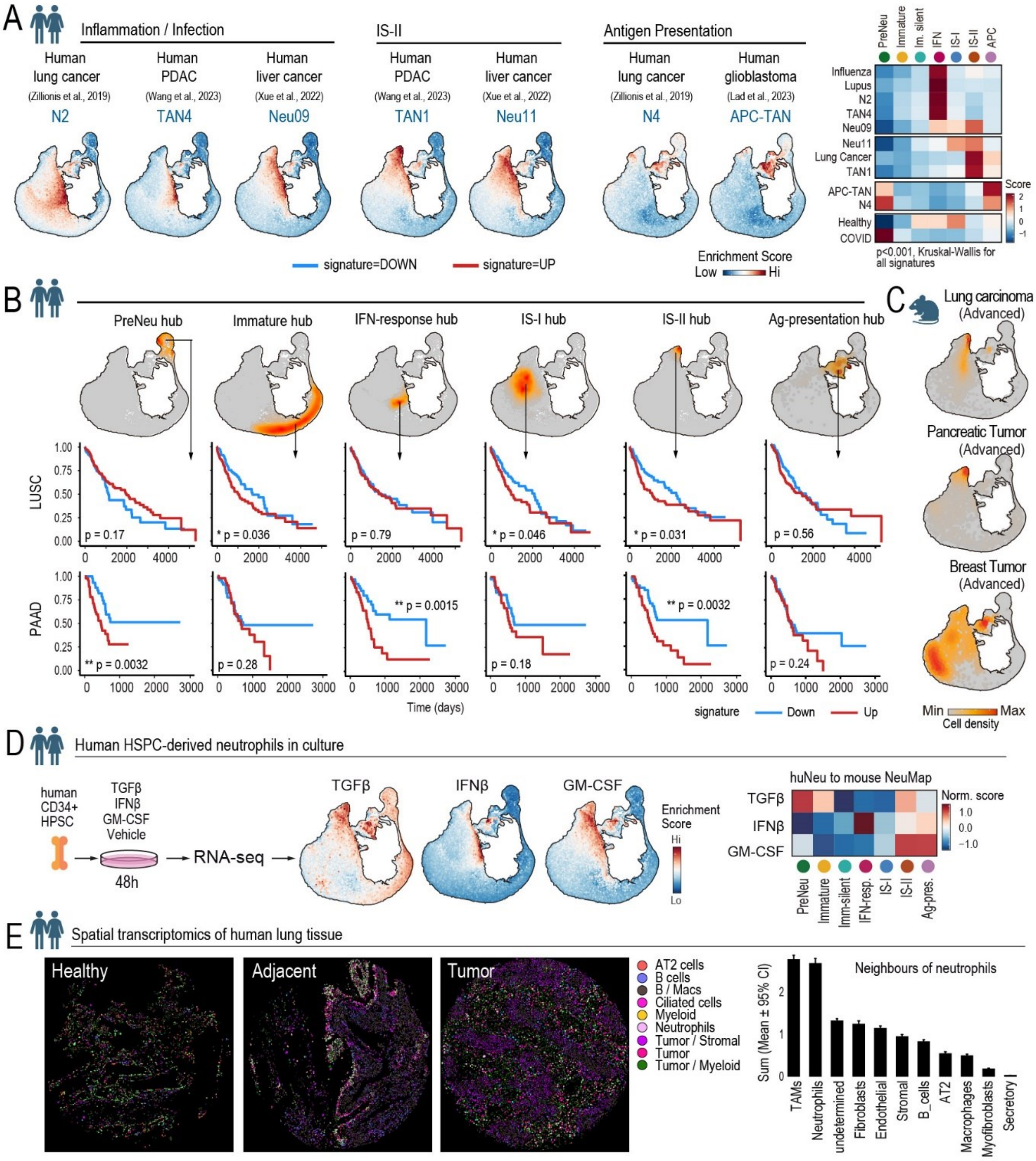

Extended Data Figure 9. Predictive potential of the NeuMAP. (**A**) Enrichment score of signatures obtained from human neutrophils from four types of cancer (lung, liver and pancreas, and glioblastoma, GBM). Shown are the associations of different clusters of neutrophils from these human cancers with hubs of inflammation/Infection (left), Angiogenesis/Immunosuppression (middle), and Antigen presentation (right). Shown are the cluster names from the indicated studies. See also Figure 5A for similar projections in infectious, autoimmune disease and lung cancer. Right, heatmap of average enrichment scores for each hub signature, scaled by signature. (**B**) Kaplan–Meier plots of LUSC and PAAD patient survival, based on high or low expression of hub signature. Statistical significance was determined by a two-sided log-rank test. (**C**) K-mass visualization on the NeuMap of neutrophils from lung cancer 21 days after intravascular injection of LLC cells (top), humane endpoint of orthotopically implanted pancreatic cancer (FC1242 cells) and breast cancer (E0771 cells) mouse models. (**D**) Human neutrophils derived from bone marrow CD34+ HSPC were cultured with the indicated cytokines and their RNA sequenced. Enrichment scores were computed for each cytokine-induced signature and mapped onto NeuMAP. Right, heatmap showing mean signature scores across hubs. (**E**) Spatial transcriptomic maps of lung tissue from patients with lung adenocarcinoma, comparing healthy, adjacent, and tumor regions. Cell types were annotated by deconvolution and overlaid as spatial coordinates. Right, neighbourhood composition using a curated cell annotation

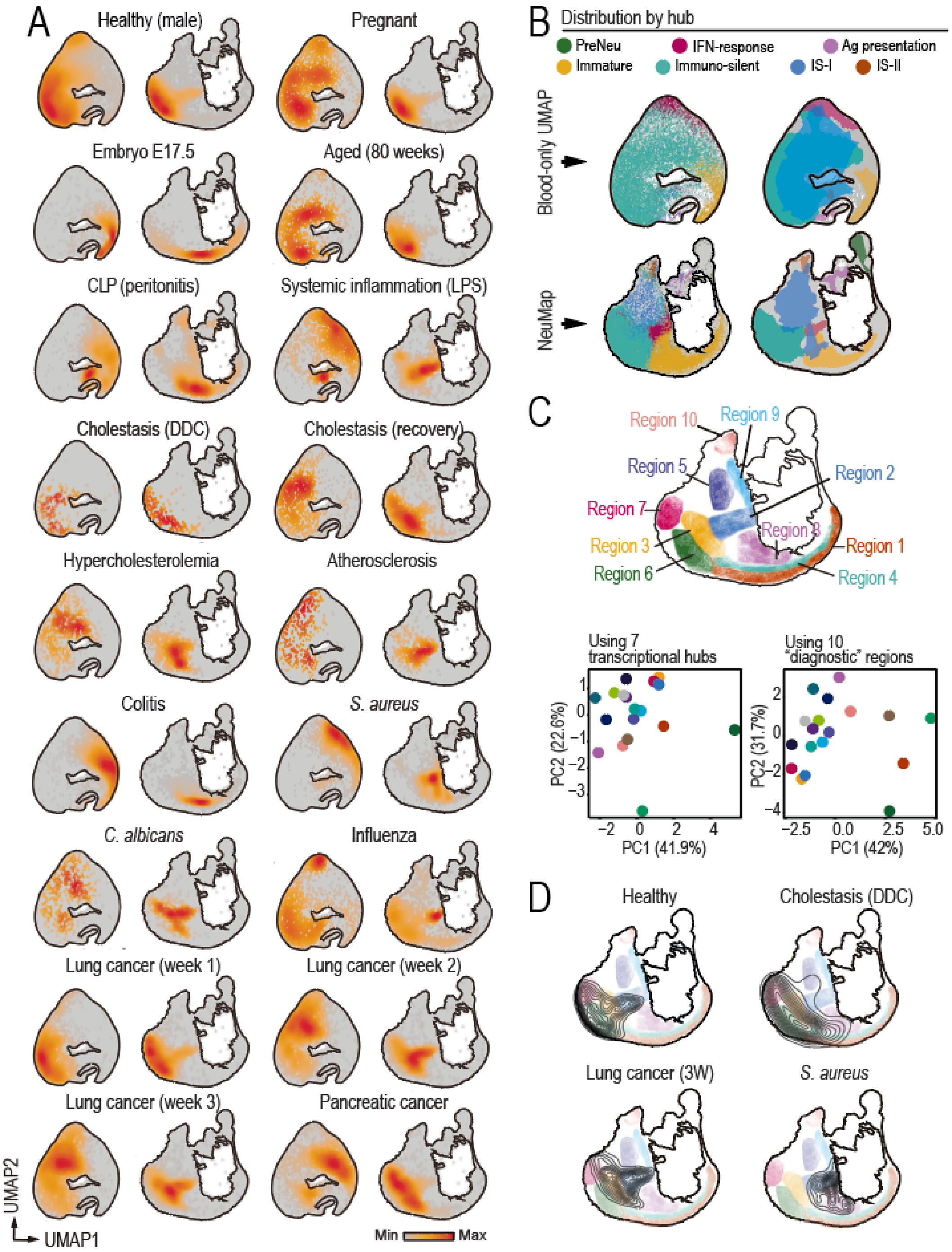

Extended Data Figure 10. Diagnostic potential of blood neutrophils projected in the NeuMap. (**A**) Blood neutrophils from 18 conditions were projected onto the blood-only UMAP or the NeuMap based on their transcriptional profile and are shown as densities or K-mass. (**B**) Distribution of cells with their assigned transcriptional hub (by color) in the blood-only UMAP and in the NeuMAP (left), showing the overlapping areas of the different hubs. (**C**) PCA analysis of blood sample distribution based on the Bhattacharyya index obtained using the 7 transcriptional hubs or the 10 expanded diagnosis regions. (**D**) Representative examples of the distribution of the blood neutrophils from four conditions onto the expanded diagnostic regions that we used to calculate the Bhattacharyya indexes.

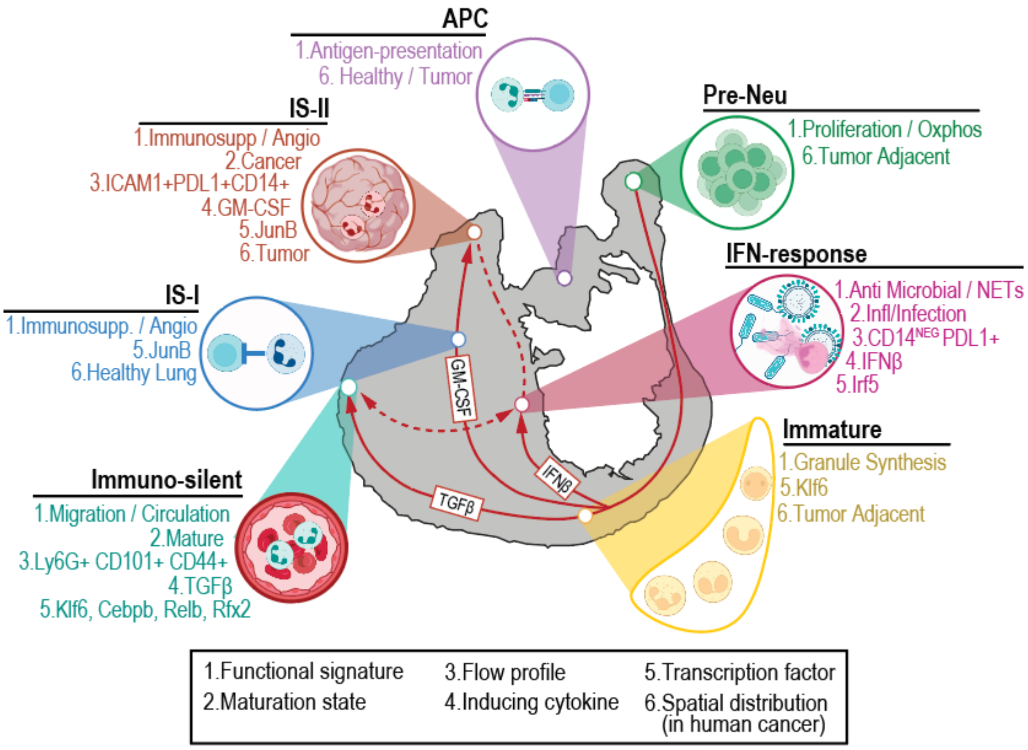

Extended Data Figure 11. Integrated transcriptional and functional map of the neutrophil compartment in mice. The scheme highlights the general structure and dynamics of the NeuMap, including cytokines driving the main trajectories, associated functions, maturation stages, cytometric profiles, transcription factors, and the spatial distribution (in human lung cancer) of neutrophils associated with each hub.

References

Supplementary Tables

Table S1. Identification of samples (65 individual samples) and biological conditions (47 different conditions) used to build the NeuMap. All samples are single cell transcriptomes from purified neutrophils generated in this study.

Table S2. Gene signatures used to identify functional hubs in the NeuMap.

Table S3. Differentially expressed genes in neutrophils from the 7 functional hubs identified in Figure1 and Extended Data Fig.2.

Table S4. Analysis of Enriched Motifs found in tissue neutrophils and clusters of the DOGMA-seq analysis.

Table S5. LRT analysis of neutrophils from BM, blood and lungs of control mice, and JunBΔN lungs from the bulk RNA-sequencing dataset, shown in and Figure 2E and Extended Data Fig.3C.

Table S6. Pseudotime trajectory analysis, from the proposed developmental trajectories in Figure 3E and Extended Data Fig.5H.